# Magnetoelectric Laminates with Novel Properties for Sensor, Transmitter, and Gyrator Applications

**Junran Xu**

Dissertation submitted to the faculty of the Virginia Polytechnic Institute and State University in partial fulfillment of the requirements for the degree of

Doctor of Philosophy

In

Material Science and Engineering

Dwight D. Viehland, Chair

Jiefang Li

Gary R. Pickrell

Guo-Quan Lu

April 27th, 2020
Blacksburg, VA

Keywords: magnetoelectric, magnetostrictive, piezoelectric, gradiometer, transmission, gyration, power efficiency, and resonance frequency.

© Copyright 2020, Junran Xu

# Magnetoelectric Laminates with Novel Properties for Sensor, Transmitter, and Gyrator Applications

**Junran Xu**

## ABSTRACT

The magnetoelectric (ME) effect is a property that results in power/energy conversion between magnetic and electric forms. Two-phase composites consisting of magnetostrictive and piezoelectric materials have been developed that show remarkable ME voltage/charge coefficients. This extrinsic ME effect is achieved by using mechanical coupling as a medium between the magnetostrictive and piezoelectric phases. As described in this thesis, I investigated the optimization of the material properties of sensors/gradiometers, transmitters, and gyrator applications using ME heterostructures with a multi-push-pull structure.

In applications, ME sensors will need to work in an open environment where there will be a mix of magnetic signals and microphonic noises. Prior research has determined that both passive and active mode ME sensors are affected by vibrational noise in the open environment. Therefore, as described herein, an ME gradiometer consisting of a pair of ME sensors working under H-field modulation (active mode) was developed to address the issue of microphonic noise. The common mode rejection ratio of my ME gradiometer was determined to be 74. Gradiometer curves were also measured, which presented the gradiometer outputs as a function of the normalized distance between the magnetic source and the ME gradiometer. Based on resulting data, the proposed ME gradiometer was confirmed to be capable of significant vibration noise rejection. However, this method is not appropriate for rejecting longitudinal vibrations due to the propagation direction

being the same as the magnetic field. To resolve this dilemma, a new ME laminate structure was designed that could better reject vibrational noise. Additionally, two different configurations were developed to measure the gradiometer curve.

Second, in order to understand how much energy can be wirelessly transmitted by ME laminates within a local area, a portable (area ~ 16 $cm^2$), a very low-frequency transmitter was developed using ME laminate with Metglas/PZT structure. The proposed strain-driven ME laminate transmitter functions as follows: (a) a piezoelectric layer is first driven by alternating current electric voltage at its electromechanical resonance (EMR) frequency; (b) subsequently, this EMR excites the magnetostrictive layers, giving rise to a magnetization change; (c) in turn, the magnetization oscillations result in oscillating magnetic fluxes, which can be detected through the use of a search coil as a receiver. The prototype measurements revealed an induction transmission capabilities in the near field. Furthermore, the developed prototype evidenced a $10^4$ times higher efficiency in the near field over a small-circular loop of the same area, exhibiting its superiority over the class of traditional small antennas.

Next, recent efforts in our group resulted in the development of an ME gyrator based on ME heterostructures. Such gyrators facilitate current-to-voltage conversion with high power efficiency. ME gyrators working at their resonance frequency are capable of converting power with an efficiency of > 90 %, which show potential for use in power convertors. Here, we found that the resonance frequency could be tuned through the use of a frequency-modulation technique. Accordingly, this method can be utilized to match the frequency difference between the power supply and the piezoelectric transducer in actual applications, which will increase the power efficiency. Another problematic issue is that the electromechanical coupling factor of piezoelectric transducers is limited by bandwidth. Typically, transducers cannot be impedance matched to a

power supply, which significantly reduces power efficiency. Our initial studies have shown that an improved impedance match can be realized by using an ME gyrator to geometrically tune a transducer, which will substantially enhance power efficiency.

The last chapter will mainly focus on ME gyrator applications. Designing linear power amplifiers that operate reliably at high frequency is quite challenging, which is mainly due to the fact that the parasitic impedances of their electronic components tend to dominate at higher frequencies, thereby leading to significant power-efficiency loss. Therefore, ME gyrator may play an important role between the power amplifier and the acoustic transducer to reduce the power loss. In this chapter, we achieved the impedance matching between a piezoelectric transducer and a power supply by implementing geometric changes to the gyrator. Both the power efficiency of an individual ME gyrator and a piezoelectric transducer are > 90%. Therefore, the total power efficiency of the ME gyrator and the piezoelectric transducer also approach > 80% when they got connected together. The second aspect of this chapter pertains to resonance-frequency tuning using three method. Since an ME gyrator will be used to achieve impedance matching, the resonance frequency of the ME gyrator and a piezoelectric transducer may not exactly match. This limitation will be overcome through capacitance tuning of the piezoelectric transducer in order to achieve frequency matching. Finally, an equivalent circuit will be developed that connects a piezoelectric transducer with a gyrator, thereby enabling the impedance of the output port of the transducer and the shifted EMR frequency of the transducer to be modified.

# Magnetoelectric Laminates with Novel Properties for Sensor, Transmitter, and Gyrator Applications

**Junran Xu**

## GENERAL AUDIENCE ABSTRACT

In my dissertation, I focus on the magnetoelectric (ME) effect, which is a property that results in power/energy conversion between magnetic and electric forms. Two-phase composites consisting of magnetostrictive and piezoelectric materials have been developed that show remarkable ME voltage/charge coefficients. As described in this dissertation, I investigated the optimization of the material properties of sensors/gradiometers, transmitters, and gyrator applications using ME heterostructures with a multi-push-pull structure.

An ME gradiometer consisting of a pair of ME sensors working under H-field modulation (active mode) was developed to address the issue of microphonic noise. The common mode rejection ratio of my ME gradiometer was determined to be 74. Gradiometer curves were also measured, which presented the gradiometer outputs as a function of the normalized distance between the magnetic source and the ME gradiometer. Besides that, a new ME laminate structure was designed that could better reject vibrational noise.

Second, in order to understand how much energy can be wirelessly transmitted by ME laminates within a local area, a portable, a very low-frequency transmitter was developed using ME laminate with Metglas/PZT structure. The prototype measurements revealed an induction transmission capability in the near field. Furthermore, the developed prototype evidenced a 10^4 times higher efficiency in the near field over a small-circular loop of the same area, exhibiting its superiority over the class of traditional small antennas

In the last chapter, we achieved the impedance matching between a piezoelectric transducer and a power supply by implementing geometric changes to the gyrator. The total power efficiency of the ME gyrator and the piezoelectric transducer approach > 80% when they got connected together. The second aspect of this chapter pertains to resonance-frequency tuning using three methods. Finally, an equivalent circuit will be developed that connects a piezoelectric transducer with a gyrator, thereby enabling the impedance of the output port of the transducer and the shifted EMR frequency of the transducer to be modified.

*To my family and friends*

# Acknowledgements

I would like to express my sincere gratitude to my advisor, Professor Dwight Viehland, for his tremendous help and support of my Ph.D studies and research. I have been always encouraged and energized by his patience, motivation, enthusiasm, and immense knowledge. I will always remember Prof. Viehland's course, *Structure and Properties of Materials.* In addition to expertly conveying his incredible knowledge of materials science, Prof. Viehland's use of humor made every class a pleasure to attend. His guidance is routinely essential and clear, which helped me throughout the long process of learning, studying, and conducting research. I benefited so much from his patience on correcting my papers, and his valuable instruction on my presentations. His example of high-efficiency and hard-work will continue to influence me in my future career.

Equally important, I would like to express my deepest appreciation to Professor Jiefang Li, who also gave fantastic suggestions and instruction during my Ph.D studies and research. I still can remember the first time she called me in to her office, where she kindly introduced me to lab expectations and what kind of research I would be working on. Without exception, every time I experienced any problems or struggled in my studies, she always took the time to help me overcome the hurdles I faced—no matter if it was a theoretical calculation or an experimental setup. Without her committed guidance and help, this dissertation would not have been possible.

I also would like to thank my committee members, Prof. Gary Pickrell and Prof. Guo-Quan Lu. I will always be grateful for their insightful comments, encouragement, and constructive feedback. From them, I learned the value of asking questions, which incentivized me to widen my research across various perspectives.

I would like to thank Dr. Chung Ming Leung and Dr. Xin Zhuang. In addition to providing moral support and encouragement, Dr. Leung helped me so much with circuit building,

experimental setup design, and equipment repair, which made my project proceed much more rapidly and efficiently. Dr. Zhuang always answered my questions patiently, and his insightful perspectives on ME sensors working under passive mode and active mode helped me enormously. I appreciate him for his theoretical explanations in terms of all kinds of ME devices we researched in our lab.

I would like to thank my fellow PhD students, Dr. Xiao Tang and Dr. Min Gao, who have become close friends since we first met in July 2015 when we started our PhD studies. They were always there to help me better understand the fundamentals of materials science—not to mention sharing much-needed downtime outside the lab.

Lastly, but most importantly, I would like to express my deepest gratitude to my parents, Dajun Xu and Chenghua Gu, and my best friend, Dr. Chenlin Zhao. My parents have always been there for me, no matter where I am, with their unconditional support and love. My best friend, Dr. Chenlin Zhao, will also be a great example in my life. We have known each other for 22 years. Every time I faced problems in my life or studies, he was always there with insightful suggestions and steadfast support. He is my brother forever.

# TABLE OF CONTENTS

# LIST OF FIGURES

# LIST OF TABLE

# CHAPTER 1: INTRODUCTION

## 1.1. Magnetoelectric effect.

As a simple definition, the term *magnetoelectricity* refers to electricity produced by the action of magnetic fiends. As a property, the *magnetoelectric effect* (ME) can be defined as a power/energy conversion between magnetic and electric forms, which is characterized by an induced electric polarization change under an applied magnetic field, or by an induced magnetization change under an applied electric field.[1-3] Therefore, the direct ME effect can be expressed as the ME voltage coefficient $\alpha_{ME}$, which is a parameter defined by the induced electric field by an applied magnetic field:

$$\alpha_{ME} = \delta E / \delta H = \delta V / t\delta H \quad (1.1)$$

where δE is the induced electric field, δH is the applied magnetic field, δV is the induced voltage response to the applied magnetic field, and t is the thickness. Similarly, the converse ME effect can be defined as the induced magnetic field by an applied electric field.[4]

In the 1960s, the ME effect was first found in chromic oxide ($Cr_2O_3$) single crystals,[5,6] which represents a milestone for ME materials research. Due to the direct coupling between dipole and spin moments at the atomic level, the ME effect in single crystals is linear. However, the electronic configurations that favor magnetization are opposed to the ones that favor polarization; accordingly, the direct coupling between dipole and spin is tiny, leading to very small ME effects in single crystals at low temperature. As an example, the ME voltage coefficient in $Cr_2O_3$ is only 14 $mVcm^{-1}Oe^{-1}$, thus reducing its ability to be used in industrial applications.[7]

Accordingly, the need to develop a composite that could achieve a significantly larger ME effect was becoming increasingly apparent. In the 1970s, van Suchtelen reported the development of two-phase composites consisting of both magnetostrictive and piezoelectric phases.[8] The most

important property of two-phase composites for use in industrial application is that one can achieve an extremely high ME coefficient—up to three orders higher than for single phase system. Unlike the intrinsic ME effect[9] of single phases, the huge ME effect associated with two-phase composites can be realized by using mechanical coupling as a medium between the magnetostrictive and piezoelectric phases. Figure 1.1 shows how the ME effect is achieved via mechanical coupling in two-phase composites. The underlying principle of the direct ME effect is that a magnetic field induces a magnetization change in the magnetostrictive layer, which results in an induced shape change; this shape change is then transmitted to the piezoelectric layer, which in turn converts the strain to a voltage/charge output with the help of the piezoelectric effect.[10] Similarly, for a converse ME effect, an electric field creates a polarization change in the piezoelectric layer, which generates an induced shape change; this strain also induces mechanical stress in the magnetostrictive phase, resulting in an induced magnetic field. The following expressions illustrate both the direct and converse ME effects:[11]

$$\begin{cases} \text{Direct ME effect} = \dfrac{\text{Electric Output}}{\text{Mechanical Input}} \times \dfrac{\text{Mechanical Output}}{\text{Magnetic Input}} \\ \text{Converse ME effect} = \dfrac{\text{Magnetic Output}}{\text{Mechanical Input}} \times \dfrac{\text{Mechanical Output}}{\text{Electric Input}} \end{cases} \tag{1.2}$$

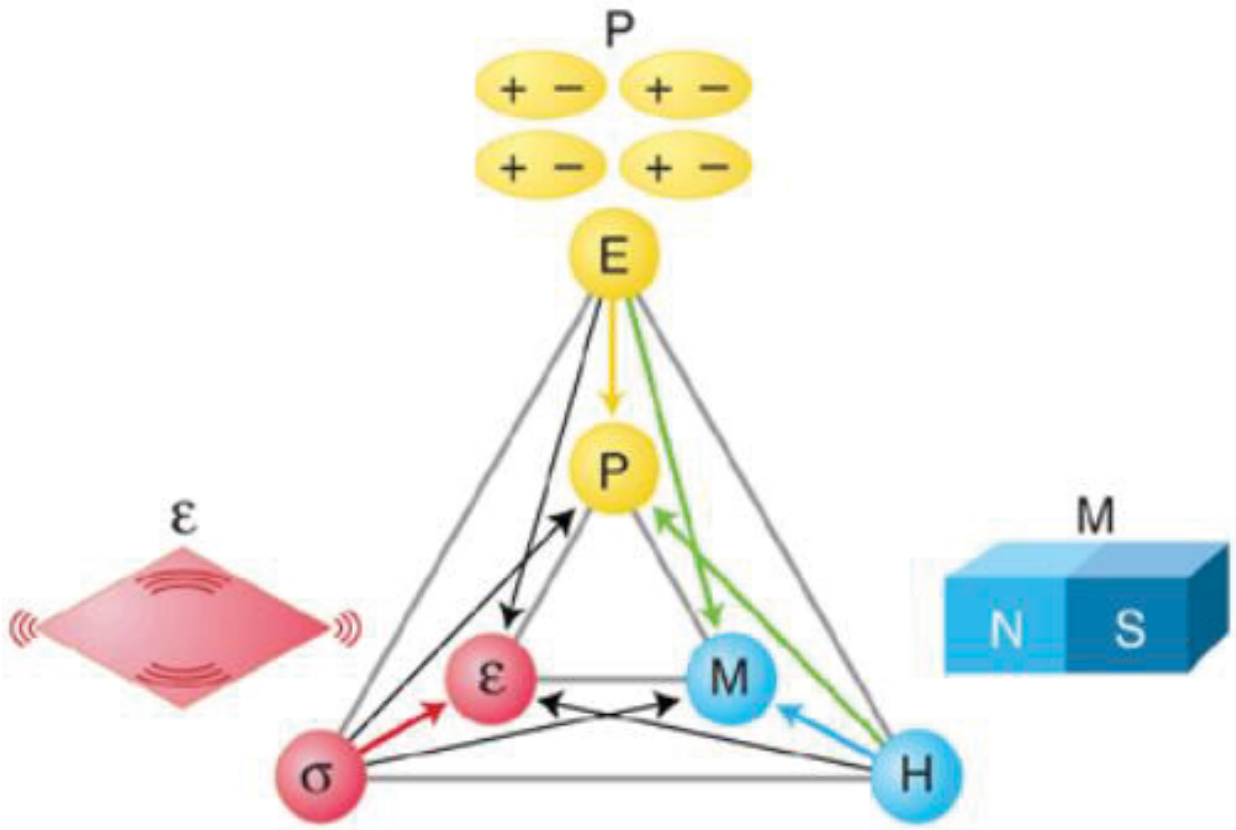


*Figure 1.1. Phase control in ferroics and multiferroics. N. A. Spaldin, M. Fiebig: The Renaissance of Magnetoelectric Multiferroics, Science 309, 391 (2005), with fair use.*

Based on this concept, in 1974 a ceramic composite consisting of $BaTiO_3$-$CoFe_2O_4$ was fabricated via the unidirectional solidification technique.[12] The ME effect of this composite was determined as 0.13 $Vcm^{-1}Oe^{-1}$, which was about seven times higher in comparison to $Cr_2O_3$ single crystals. Also notable is that this is the first ME composite based on using mechanical coupling as a medium between the magnetostrictive and piezoelectric phases. This development of more than 40 years ago spurred the generation and study of new families of bulk two-phase ME composites, leading to four widely accepted problems that limit even higher ME effects: (1) the difficulty in controlling the interconnectivity of the constituent phases; (2) the chemical reactions that occur between phases during the sintering process; (3) the breakdown of the piezoelectric phase due to

the low resistance of the magnetostrictive phase during the polarization process of the piezoelectric phase; (4) insufficient mechanical coupling between phases due to surface defects such as pores and cracks.

In order to overcome these problems, ME-laminated composites consisting of magnetostrictive and piezoelectric layers were developed.[13-15] The laminate was configured as a sandwich structure, which combined a Pb(Zr, Ti)$O_3$ (PZT) piezoelectric ceramic disk between two Terfenol-D magnetostrictive alloys disks that were bonded by epoxy. The PZT disk was polarized in the thickness direction, and the Terfenol-D disks were magnetized radially. The ME coefficient of the laminate was determined to be 4.68 $Vcm^{-1}Oe^{-1}$ at 1 kHz. Later on, Dong et al. proposed an ME laminate in rectangular form that also featured a sandwich structure, and demonstrated that its in-plane direction should be along the incident direction to achieve an optimized ME coefficient.[16,17] More recently, Wang et al. fabricated an ME laminate consisting of Metglas and $Pb(Mg_{1/3}\ Nb_{2/3})O_3$–$PbTiO_3$ (PMN-PT) single crystals; the ME coefficient was significantly increased to a value of 52 $Vcm^{-1}Oe^{-1}$ (at 1 kHz)[18] with a multi-push-pull structure, which is three orders higher than $Cr_2O_3$ single crystals.

## 1.2. Magnetostrictive and piezoelectric materials.

### 1.2.1. Magnetostriction and magnetostrictive materials.

First identified by James Joule in 1842, magnetostriction is a property of ferromagnetic materials whereby a material will change its shape under an applied magnetic field, or will change its magnetization under an applied mechanical stress.[19] While almost all the ferromagnetic materials possess magnetostriction, only a small fraction of them demonstrate giant magnetostriction.

The magnetostriction of a material is easy to understand at a macroscopic level. Figure 1.2 shows the B-H behavior curve for a ferromagnetic or ferrimagnetic material that is initially unmagnetized. As shown therein, the magnetic field B is not proportional to the magnetic field strength H for ferromagnets and ferrimagnets. For an unmagnetized specimen, the sum of magnetizations for all domains is zero. Initially, the moments of the domains are randomly oriented such that there is no net B field. When an H field is applied, the domains that are oriented in directions favorable to the applied field grow, and the domains change shape and size according to the movement of domain boundaries. As the magnetic field strength increases, the process continues until the macroscopic specimen becomes a single domain. Finally, saturation is achieved when this single domain orients along the direction of the H field. During the entire process, the domain walls move, resulting in a shape or strain change induced by the H field. In order to present the most intense shape change, magnetostrictive materials are always working under an optimized DC magnetic bias.

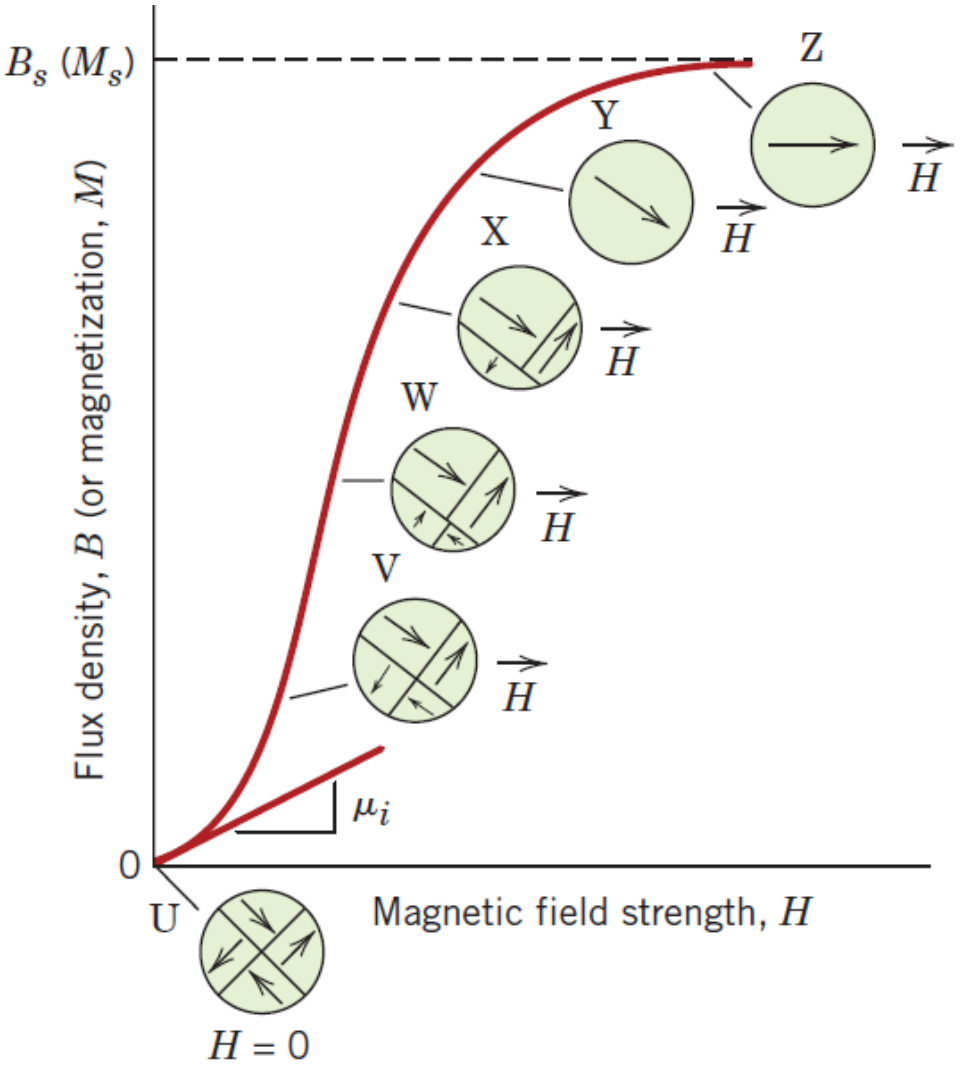


*Figure 1.2. The B-versus-H behavior for a ferromagnetic or ferrimagnetic material. Callister, William D., and David G. Rethwisch. Materials Science and Engineering: An introduction. Vol. 7. New York: John Wiley & Sons, 2007, with fair use.*

Terfenol-D,[19] Galfenol,[20] and Metglas[21] are the most widely used magnetostrictive materials in sensing and actuator applications. Terfenol-D possesses the highest magnetostriction (>1600) and the lowest permittivity, while Galfenol exhibits lower magnetostriction and higher permeability comparing with Terfenol-D. Metglas has the lowest magnetostriction and highest permeability (>40000), as well as demonstrates the smallest saturation magnetic field.

This investigation was designed to better understand AC magnetic field detection, as then utilize a material with a high magnetostrictive coefficient and small DC magnetic bias for incorporation in ME laminates. As indicated in Figure 1.3, we can observe that the magnetostrictive coefficient of Metglas surpasses the others, while also requiring the smallest DC magnetic bias. Therefore, we choose Metglas 2605 for the ME laminate, which shows excellent magnetic properties in the Metglas family.

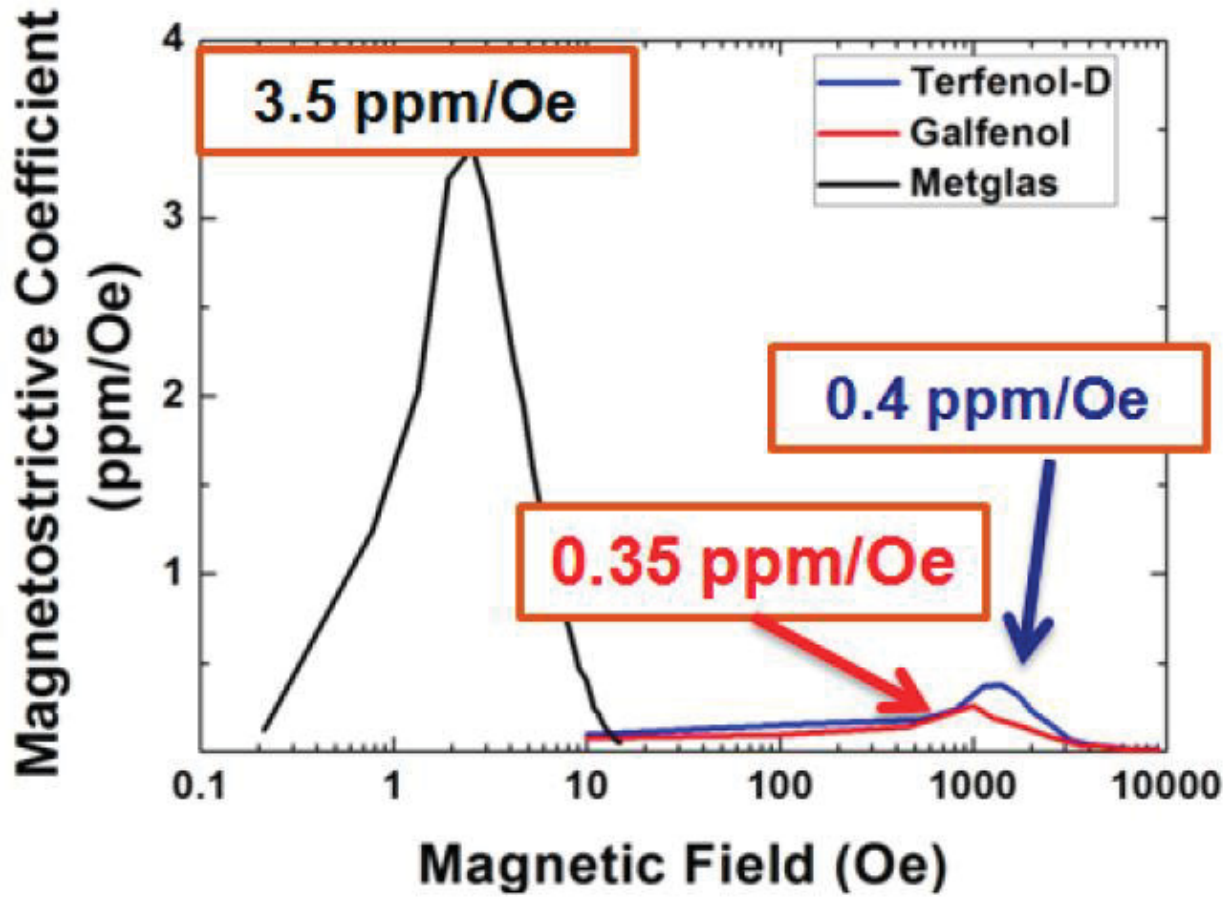


*Figure 1.3. Magnetostrictive coefficient as a function of magnetic field for Terfenol-D (red), Galfenol (blue) and Metglas (black). Li, Feng, et al. "Magnetoelectric flexural gate transistor with nanotesla sensitivity." Journal of Microelectromechanical Systems 22.1 (2012): 71-79, with fair use.*

1.2.2. Piezoelectricity and piezoelectric materials.

Piezoelectricity refers to a linear coupling between applied mechanical stress and induced electric polarization (the direct piezoelectric effect), or between applied electric field and induced mechanical strain (the converse piezoelectric effect)[22]. The following fundamental equations show the coupling between electric and mechanical parameters in piezoelectric materials,

$$\begin{cases} \sigma = \mathrm{Cs} - d^{T}\mathrm{E} \\ \mathrm{D} = \mathrm{ds} + \varepsilon\mathrm{E} \end{cases} \tag{1.3}$$

where σ is stress, s is strain, d is piezoelectric charge constant, E is electric field, D is electric displacement, and ε is dielectric constant.

Figure 1.4 illustrates the poling process of a piezoelectric ceramic. Before poling, the direction of polarization among the adjacent domains is random, which indicates the absence of overall polarization in the ceramic element. After applying a strong DC electric field, however, the domains in the ceramic element become aligned; at the same time the element lengthens in the direction of the electric field. When the electric field is removed, most of the electric dipoles are essentially locked along the direction of the applied electric field. Accordingly, the ceramic element displays permanent polarization, and is permanently elongated.

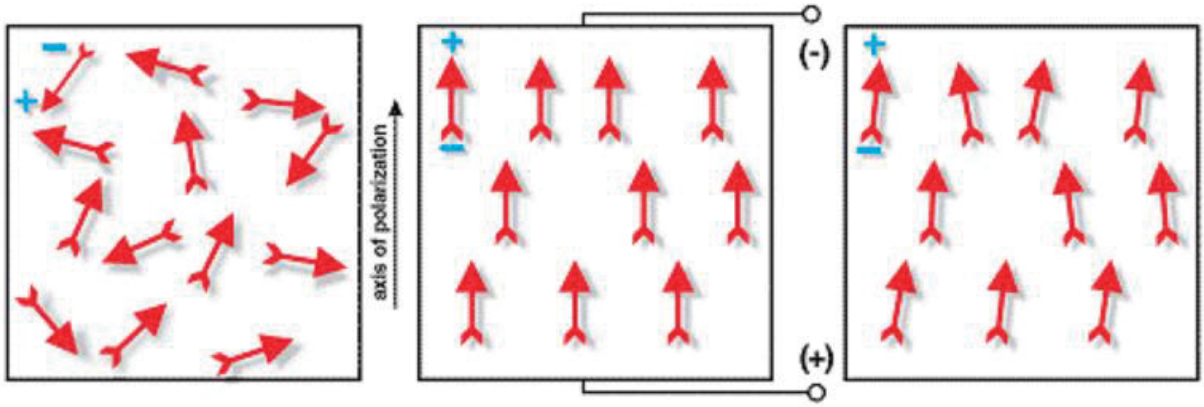


*Figure 1.4. The poling process of a piezoelectric material. APC International, Ltd. Piezoelectric Ceramics: Principles and Applications. APC International, 2002, with fair use.*

As described in this thesis, we will investigate and compare PZT[23] and PMN-PT single crystals[24] in terms of their performance in ME heterostructures. PZT (lead zirconate titanate), one the most widely used piezoelectric ceramic materials, is essentially a mass of perovskite ceramic crystals. When the temperature is above Curie point, there is no dipole moment in each perovskite crystal, which exhibits a simple cubic symmetry (shown in Figure 1.5). Below the Curie temperature, however, on observes a dipole moment in each crystal with rhombohedral and tetragonal symmetry. Because compositions tend to pole best near the morphotropic phase boundary[25,26] (MPB) between the rhombohedral and tetragonal mixtures of a perovskite structure, compositions of PZT ceramic are purposefully determined near the phase transition to enhance piezoelectric properties. Therefore, near the MPB, domain wall movements and phase changes between the rhombohedral and tetragonal phases occur intensively during the poling process.

Based on the success of PZT, further investigations targeting lead-based relaxor materials have focused on PMN-PT single crystals due to their much higher piezoelectric and electrostrictive properties in comparison to PZT ceramics. Compared with the structure of PZT, PMN-PT single

crystals present analogous phase diagrams with MPBs between the rhombohedral and tetragonal phases. However, PMN-PT single crystals display a much better dielectric constant and piezoelectric coefficient, which can largely be attributed to two factors: (1) the uniformity of PMN-PT single crystal growth, and (2) the enhancement of the piezoelectric response contributed by Nb atoms.

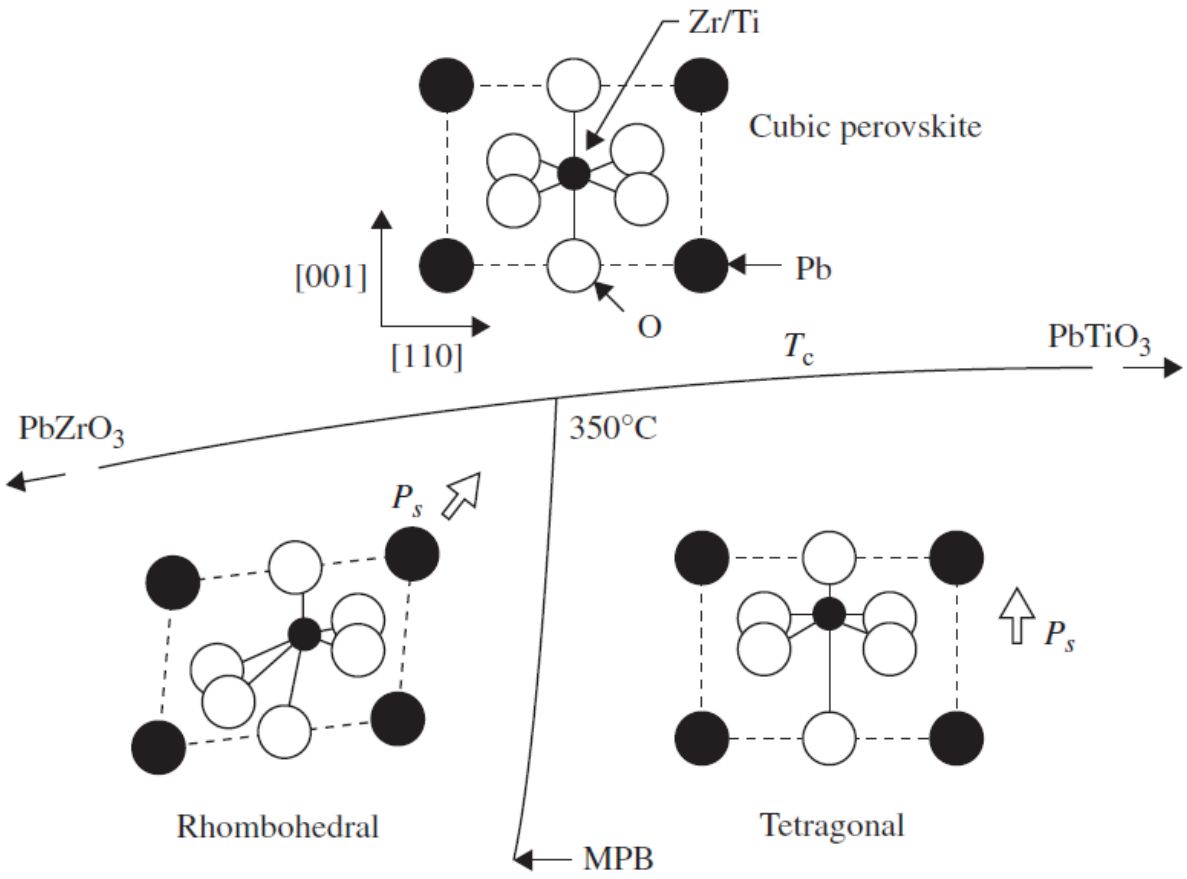


*Figure 1.5. A portion of the PZT phase diagram showing the structure change at the Curie temperature ($T_c$) and the morphotropic phase boundary. Newnham, Robert E. Properties of Materials: Anisotropy, Symmetry, Structure. Oxford University Press on Demand, 2005, with fair use.*

## 1.3. Magnetoelectric laminated composites.

### 1.3.1. Structure of ME laminated composites.

Due to the fact that magnetostriction happens in the magnetostrictive phase, and insufficient DC magnetic bias leads to a loss of magnetic remanence, ME laminate composites require an optimized DC magnetic bias in order to display their best ME effects.[27-31] Furthermore, the optimized DC magnetic bias has to occur at the maximum point of the slope on the magnetostriction-DC magnetic bias curve (M-H curve), where the magnetostrictive phase possesses the highest piezomagnetic coefficient. By reason of the fact that a piezomagnetic coefficient for ME laminate composites is strongly dependent on their structure, a thorough structural analysis of these materials is critical.

There are four basic ME configurations wherein both the directions of magnetization and polarization can be along either the transverse (T) or longitudinal (L) directions of ME laminates.[32,33] The four basic modes with different ME configurations are shown as sandwich structures in Fig. 1.6. For example, as shown in the T-T mode (a), both the directions of magnetization and polarization are along the transverse direction of the ME laminate. Based on prior investigations in our group,[34] the L modes (L-T, L-L) require a smaller optimized DC magnetic bias in comparison to the T modes (T-T, T-L), while L modes exhibit significantly higher ME coefficient than the T modes. Accordingly, we selected L modes for our study.

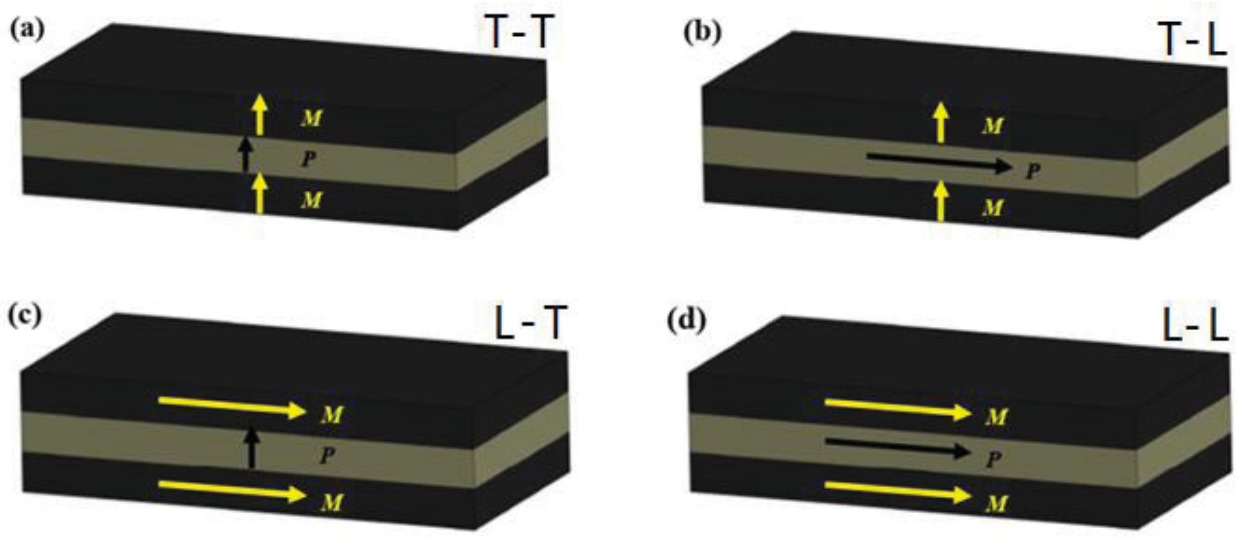


*Figure 1.6. Basic modes for ME laminates.*

Compared with the L-T mode, the L-L mode should be expected to exhibit a higher ME voltage coefficient due to the fact that $d_{33}$ in the longitudinal direction is stronger than $d_{31}$ in the transverse direction. However, there are two limitations associated with the L-L mode. The first is high poling voltage. Owing to the fact that the longitudinal direction of the ME laminate exhibits the longest length, it requires much higher voltage for its poling process compared with the transverse direction of the ME laminate. The second limitation is low capacitance; specifically, the L-L mode inherently presents low capacitance, which can be easily influenced by the stray capacitance of the measurement system with low charge output. In order to overcome these limitations, researchers developed a L-L push-pull mode,[31] whose structure is depicted in Figure 1.7, and which is reported to exhibit four times higher capacitance than L-L mode with piezoelectric layers of exactly the same length.

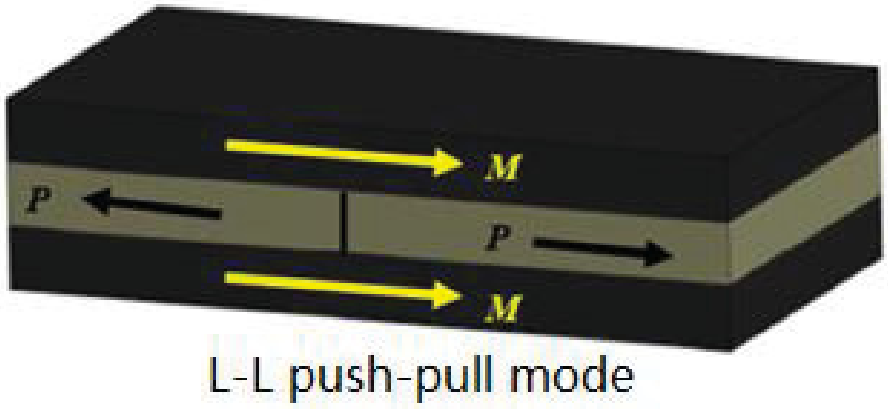


*Figure 1.7. Structure of L-L push-pull mode.*

To increase the capacitance of the piezoelectric layer, Dong et al. developed a multi-push-pull structure, which is shown in Fig. 1.8[35]. For this study we chose to utilize L-L multi-push-pull mode ME laminates. Specifically, a PZT/PMN-PT single crystal piezoelectric layer made up of five 40mm long macro-fibers in parallel was bonded between two 80mm long Metglas layers using epoxy, where each layer consisted of three Metglas 2605 foils that were stacked and joined with epoxy. The PZT/PMN-PT fibers were poled in the longitudinal direction through the use of interdigital electrodes applied on both the top and bottom of these fibers. This configuration can be broken down into many single pull-push modes, which is shown in the inset of Fig. 1.8. By incorporating this particular structure, the capacitance of ME laminates can be significantly enhanced.

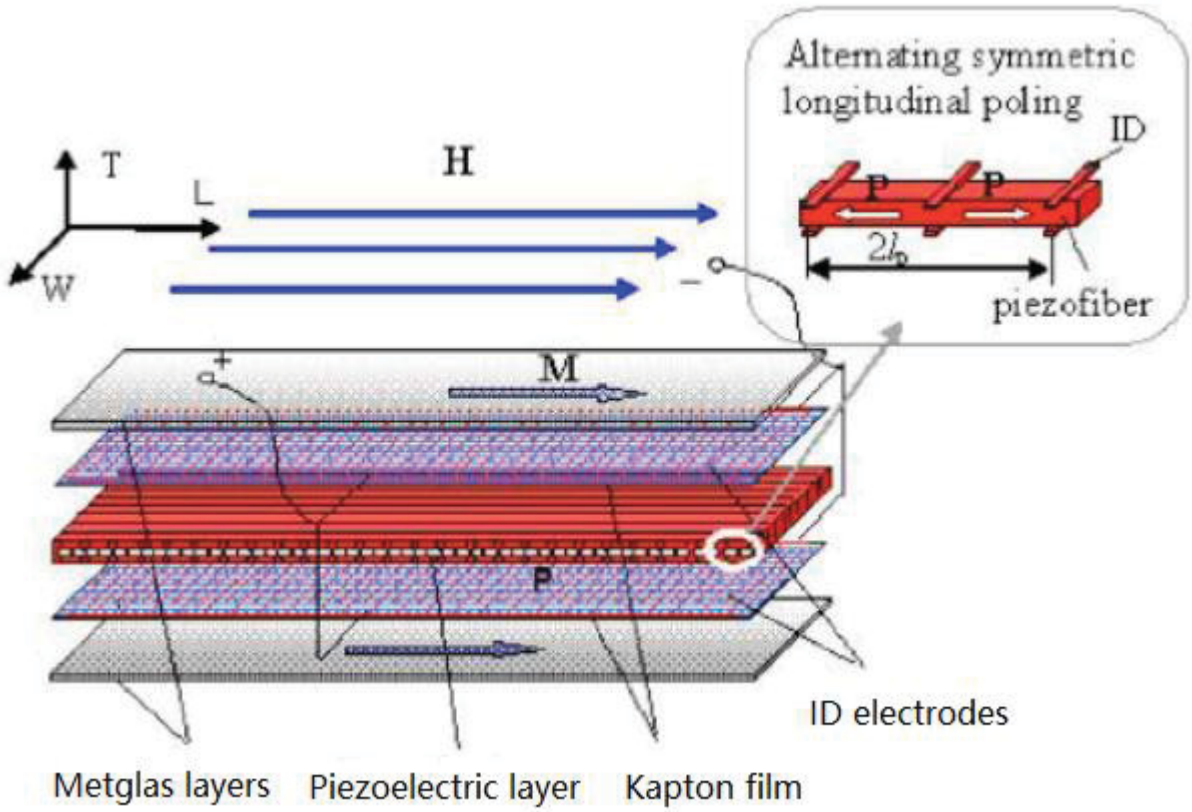


*Figure 1.8. Schematic structure of L-L multi-push pull mode. Gao, Junqi. Magnetoelectric (ME) composites and functional devices based on ME effect. Diss. Virginia Tech, 2013, with fair use.*

1.3.2. Working principles of ME laminated composites.

Figure 1.9 provides a cross-section view of an ME laminate in the L-L multi-push-pull mode. The yellow region in the middle represents the PZT/PMN-PT layer, which was polarized in the longitudinal direction using interdigitated electrodes, and the red and blue points are the positive and negative electrodes. The purple layers at the top and bottom are the Metglas layers, which were bonded to the electrodes using epoxy. In terms of how an ME laminate works, a magnetic signal is applied to the ME sensor, thereby inducing a magnetization change in the magnetostrictive layer, which results in a shape change on magnetostrictive layer. This shape change is then transmitted to the piezoelectric layer, which in turn converts the strain to a voltage/charge output with the help of the piezoelectric effect.

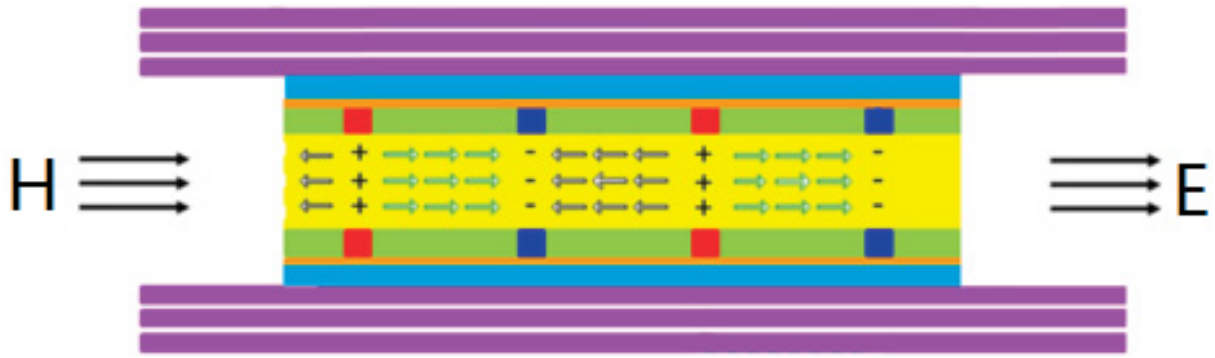


*Figure 1.9. Schematic cross-section of ME laminate with L-L multi-push-pull configuration. Li, M., et al. "Theoretical modelling of magnetoelectric effects in multi-push–pull mode Metglas/piezo-fibre laminates." Journal of Physics D: Applied Physics 45.35 (2012): 355002, with fair use.*

1.3.3. Characterization of ME effect.

Figure 1.10 provides our experimental setup for measuring the ME voltage coefficient. A determined frequency AC magnetic field was provided by a pair of Helmholtz coils via a constant-current supply amplifier. A DC magnetic bias field was generated by a water-cooled, C-shaped electromagnet under the energization of a DC current supply. The ME laminate was placed in the center of the Helmholtz coil. When the sample is an L-L mode ME laminate, the longitudinal direction of the laminate should be parallel to the direction of the AC magnetic field. The voltage and charge of the ME laminate were measured with a data acquisition unit or a charge meter.

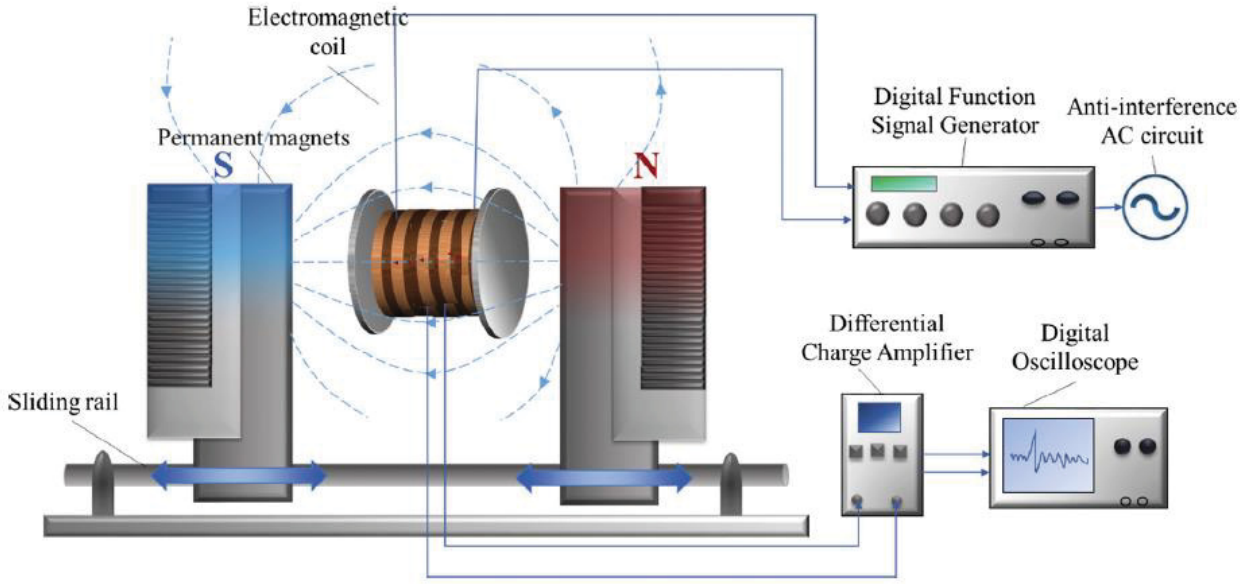


*Figure 1.10. Schematic of ME voltage coefficient measurement. Pei, Huafu, et al. "Magnetostrictive strain monitoring of cement-based magnetoelectric composites in a variable magnetic field by fiber Bragg grating." Construction and Building Materials 149 (2017): 904-910, with fair use.*

1.3.4. Thickness ratio of ME laminated composites.

As verified by both theoretical and experimental findings, the ME effect strongly depends on the thickness ratio of ME laminates, with the structure of one piezoelectric layer bonded between two magnetostrictive layers. The expression of thickness radio n is shown in Equation 1.4,

$$n = \frac{2t_m}{2t_m + t_p} \tag{1.4}$$

where $t_m$ and $t_p$ are the thickness of the magnetostrictive layer and the piezoelectric layer, respectively. Many researchers have discussed how the thickness ratio impacts the ME effect. For example, Srinivasan et al. reported that the ME effect will decrease when both the magnetostrictive and piezoelectric layers increase—even in instances when the thickness ratio is maintained;[36] the researchers attributed the weakened ME effect to growth-induced strain and interfacial impurities between two phases. Based on theoretical findings, Dong et al. reported that the $\alpha_{ME}$ would exhibit a linear increase with an increase in thickness ratio.[37] Lin et al. reported that when the thickness ratio n was increased, the $\alpha_{ME}$ initially increased, achieving its highest value at n = 0.714, but then decreased. The final degradation can be attributed to a decrease in the effectiveness of the piezoelectric phase.[38] Similarly, Sim et al. documented how a thickness increase in the piezoelectric phase weakened magnetostrictive behavior.[39]

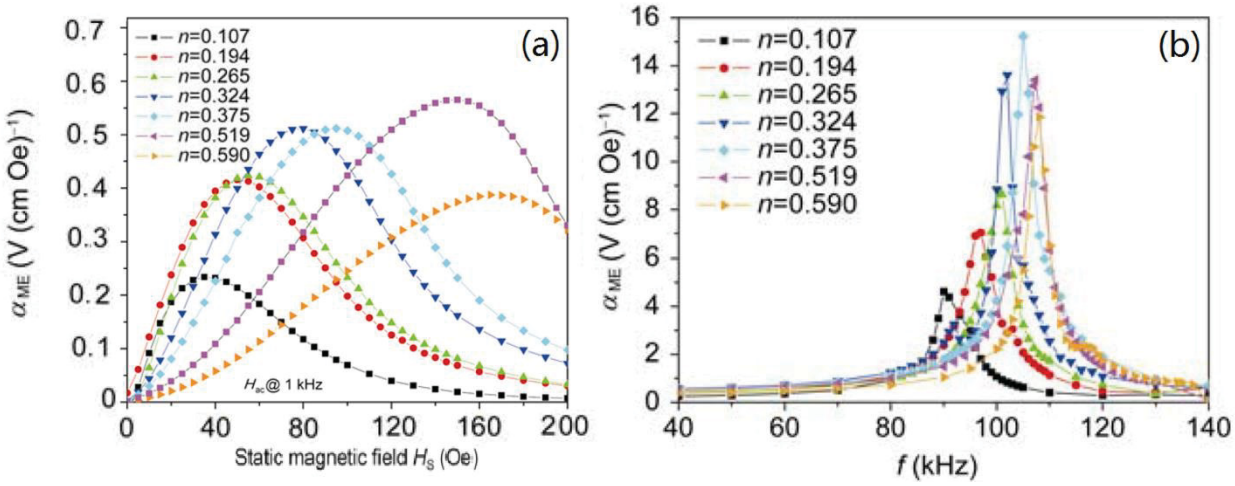


*Figure 1.11. (a) ME voltage coefficient as a function of DC magnetic bias at non-resonance frequency, (b) ME voltage coefficient as a function of frequency with optimized DC magnetic bias. Fang, Fei, ChangPeng Zhao, and Wei Yang. "Thickness effects on magnetoelectric coupling for Metglas/PZT/Metglas laminates." Science China Physics, Mechanics and Astronomy 54.4 (2011): 581-585, with fair use.*

Based on prior studies, Fang et al. obtained comparative measurements of ME voltage coefficients between the non-resonance and resonance of the ME laminate.[40] The structure of the ME laminate was as same as the L-T mode configuration shown in Fig. 1.6. The measured results are provided in Fig 1.11. Specifically, Figure 1.11(a) shows the $\alpha_{ME}$ as a function of DC magnetic bias with increasing thickness ratio n at non-resonance frequency. When the DC magnetic bias is increased, the $\alpha_{ME}$ first increases and then achieves its maximum with a fixed thickness ratio; it then decreases rapidly with further increases in DC magnetic bias. When the thickness ratio is increased, the peak value of $\alpha_{ME}$ first increases and then achieves its maximum, after which it decreases with increasing thickness ratio. Figure 1.11(b) shows the $\alpha_{ME}$ as a function of frequency measured under optimized DC magnetic bias with increasing thickness ratio. As we can

obverse, the resonance frequency moves from low frequency to high frequency with increasing thickness ratio. With increases in the thickness ratio, the peak value of $\alpha_{ME}$ first increases and then achieves the maximum; it then decreases with an increase in thickness ratio. Reports have confirmed that $\alpha_{ME}$ reaches its maximum at a certain resonance frequency with a fixed thickness ratio, which is due to the electromechanical resonance of the piezoelectric phase in ME laminates.[28,41] We also observed that the optimized thickness ratio measured under non-resonance frequency and resonance frequency are different, which can be explained using expressions of $\alpha_{ME}$ under non-resonance frequency and resonance frequency. These equations are shown below:

$$\begin{cases} \left|\frac{dV}{dH}\right| = \frac{ng_{31,p}d_{33,m}t_p}{ns_{11,p}^{D}+(1-n)s_{33,m}^{H}} \\ \left|\frac{dV}{dH}\right|\text{res} = \frac{8Q_m ng_{31,p}d_{33,m}t_p}{\pi^2 ns_{11,p}^{D}+(1-n)s_{33,m}^{H}} \end{cases} \quad (1.5)[42]$$

where $g_{31,p}$ is the piezoelectric constant, $d_{33,m}$ is the piezomagnetic constant, $s_{11,p}^{D}$ is the elastic compliance coefficient of the piezoelectric layer under constant electric displacement, $s_{33,m}^{H}$ is the elastic compliance coefficient of the magnetostrictive layer under constant magnetic field, and $Q_m$ is the mechanical quality factor. Apparently, the difference between $\alpha_{ME}$ at non-resonance frequency and resonance frequency is $Q_m$, and the thickness ratio with the highest $Q_m$ at resonance frequency is different from the thickness ratio with the highest $\alpha_{ME}$ at non-resonance frequency.

## 1.4. Prior state-of-art of ME sensors.

### 1.4.1. Passive mode ME sensors.

For this thesis work on ME sensors, we utilized ME laminates in the L-L multi-push-pull configuration. When research was first conducted on ME sensors, investigators tended to focus on how to achieve higher sensitivity in ME sensors, referring to ME coefficient, which has been thoroughly investigated.[15,35,36,43-45] Note that the ME laminates consisting of Metglas alloys and

PZT or PMN-PT single crystal fibers exhibit a very high ME voltage coefficient of 20 $Vcm^{-1}Oe^{-1}$.[46] Importantly, however, a good ME sensor requires both high ME coefficient as well as a low noise floor for detection applications. The first extremely low noise floor ME sensor was fabricated using Metglas/PMN-PT/Metglas laminates.[18]

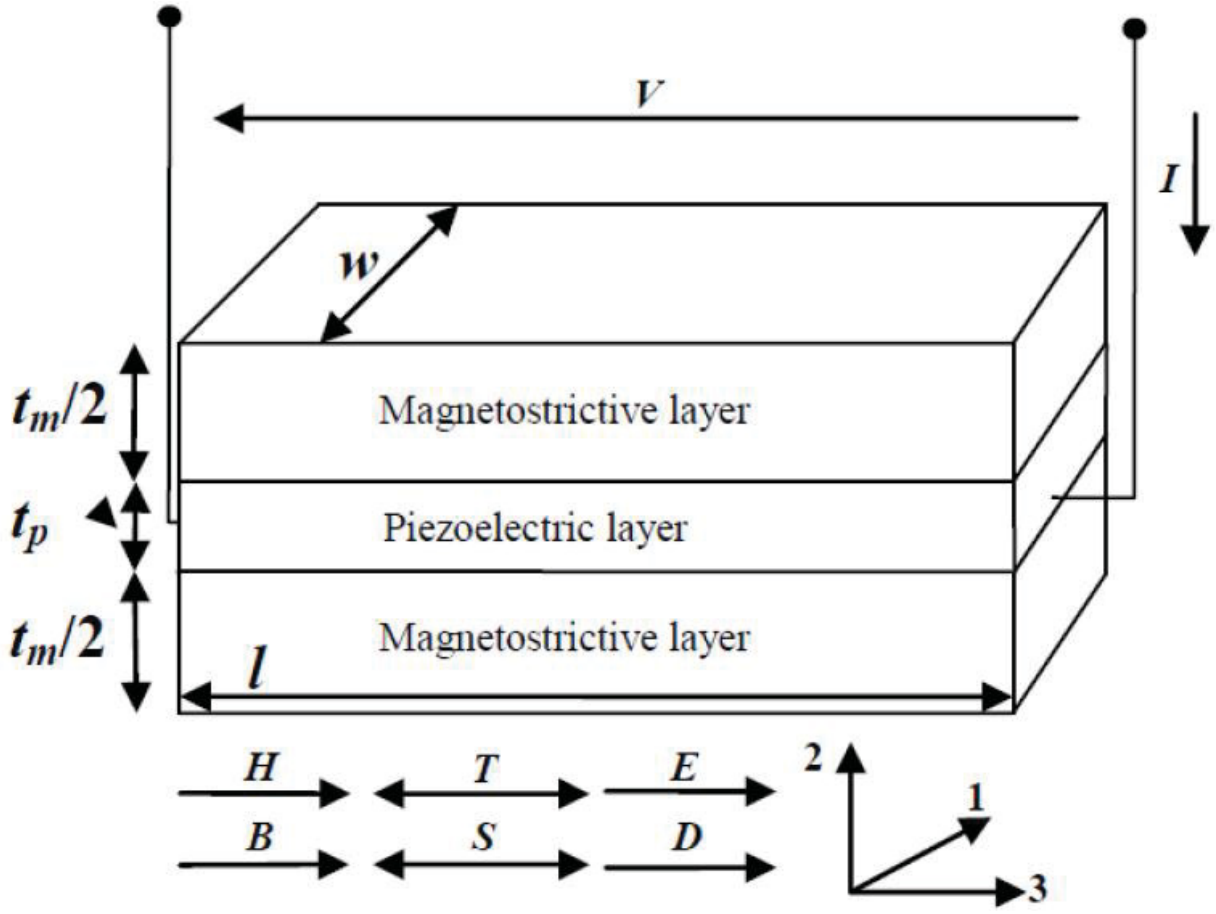


*Figure 1.12. Sketch view of the ME sensor in L-L mode. Zhuang, Xin, et al. "Theoretical intrinsic equivalent magnetic noise evaluation for magneto (elasto) electric sensors using modulation techniques." IEEE Sensors Journal 14.1 (2013): 150-158, with fair use.*

Prior research has documented the importance of analyzing and understanding the working principles of an ME sensor using Mason's model.[34,37] For the present study, given that the mechanical motion is only along the longitudinal direction of our ME sensors, the magnetostrictive and piezoelectric layers will be considered as free bodies in the perpendicular direction. As discussed earlier, there are four basic modes (Fig. 1.6). Here, we use L-L mode consisting of two magnetostrictive layers and one piezoelectric layer as an example. Figure 1.12 shows the ME sensor mode in the L-L configuration; note that the electric field (*E*), electric displacement (*D*), magnetic field (*H*), and magnetic flux density (*B*) are all along the "3" direction, which is also the longitudinal direction of the ME laminate. The dimensions of the magnetostrictive and piezoelectric layer are $l \times w \times t_m$ and $l \times w \times t_p$, respectively. Considering the both ends of the ME laminate are free, the forces on both ends of the ME laminate should be $F_1 = F_2 = 0$, which can be expressed as:

$$\begin{cases} F_1 = F_{1,m} + F_{1,p} \\ F_2 = F_{2,m} + F_{2,p} \end{cases}. \tag{1.6}$$

By applying the basic magnetostrictive and piezoelectric equations,

$$\begin{cases} B_3 = \mu_{33}^{\sigma} H_3 + d_{33,m}\sigma_3 \\ S_3 = s_{33,m}^{H}\sigma_3 + d_{33,m}D_3 \end{cases} and \begin{cases} E_3 = \beta_{33}^{\sigma} D_3 - g_{33,p}\sigma_3 \\ S_3 = s_{33,p}^{D}\sigma_3 + g_{33,p}D_3 \end{cases}, \tag{1.7}$$

we generate the following equations,[47]

$$\begin{cases} F_1 = (\zeta_m + \zeta_p)\left(j\tan\frac{kl}{2}\, v_1 + \frac{v_1+v_2}{j\sin kl}\right) - \frac{g_{31,p}}{j\omega s_{33}^{D}} I + \frac{d_{33,m}A_m}{s_{33,m}^{H}} H_3 \\ F_2 = (\zeta_m + \zeta_p)\left(j\tan\frac{kl}{2}\, v_2 + \frac{v_1+v_2}{j\sin kl}\right) - \frac{g_{31,p}}{j\omega s_{33}^{D}} I + \frac{d_{33,m}A_m}{s_{33,m}^{H}} H_3 \end{cases}. \tag{1.8}$$

where $\zeta_m = \frac{k_m A_m}{\omega s_{33,m}^{H}}$ and $\zeta_p = \frac{k_p A_p}{\omega s_{33,p}^{D}}$ are the characteristic impedance of the magnetostrictive and piezoelectric layers, respectively, *j* is the imaginary number, *k* is the wave number, *l* is the length of the ME laminate, $v_1$ and $v_2$ are the vibration speeds at both end of the ME laminate,

$g_{33,p}$ is the piezoelectric constant, $d_{33,m}$ is the piezomagnetic constant, $s_{33,m}^{H}$ is the elastic compliance of magnetostrictive phase under constant magnetic field, $A_m$ is the side surface area ($w \times t_m$) of the magnetostrictive phase, $I$ is the induced electric current, and $H_3$ is the applied magnetic field. When the electric potential is coupled with (1.8), we have,

$$\begin{cases} F_1 = (\zeta_m + \zeta_p)\left(j\tan\frac{kl}{2}\, v_1 + \frac{v_1+v_2}{j\sin kl}\right) - \frac{g_{31,p}}{j\omega s_{33}^{D}} I + \frac{d_{33,m}A_m}{s_{33,m}^{H}} H_3 \\ F_2 = (\zeta_m + \zeta_p)\left(j\tan\frac{kl}{2}\, v_2 + \frac{v_1+v_2}{j\sin kl}\right) - \frac{g_{31,p}}{j\omega s_{33}^{D}} I + \frac{d_{33,m}A_m}{s_{33,m}^{H}} H_3 \\ V = \frac{g_{33,p}}{j\omega s_{33}^{D}} \frac{t_p}{l} (v_1 + v_2) - \frac{I}{j\omega} \frac{\beta_{33}^{S} t_p}{lw} \end{cases}, \tag{1.9}$$

where $V$ is induced voltage. Therefore, the equivalent circuit can be obtained from (1.9), which is shown in Fig. 1.13. Then, we can observe that the magnetic field $H$, the induced voltage $V$, and the induced electric current $I$ are all related to the vibration speed $v$. Therefore, we can define these parameters as follows:

$$\begin{cases} \varphi_m = wt_m \frac{d_{33,m}}{s_{33,m}^{H}} \text{ and } \varphi_p = \frac{wt_p}{l} \frac{d_{33,p}}{s_{33,p}^{E}} \\ Z_{1,mech} = j(\zeta_m + \zeta_p)\tan\frac{kl}{2} \text{ and } Z_{2,mech} = j(\zeta_m + \zeta_p)\frac{1}{jsinkl} \\ C = \frac{wt_p}{l}\varepsilon_{33}^{S} \end{cases}, \tag{1.10}$$

where $\varphi_m$ and $\varphi_p$ are the coupling coefficients of the magnetostrictive and piezoelectric layers, $Z_{1,mech}$ and $Z_{2,mech}$ are the equivalent mechanical impedances in Fig. 1.13, and $C$ is the capacitance of the piezoelectric layer.

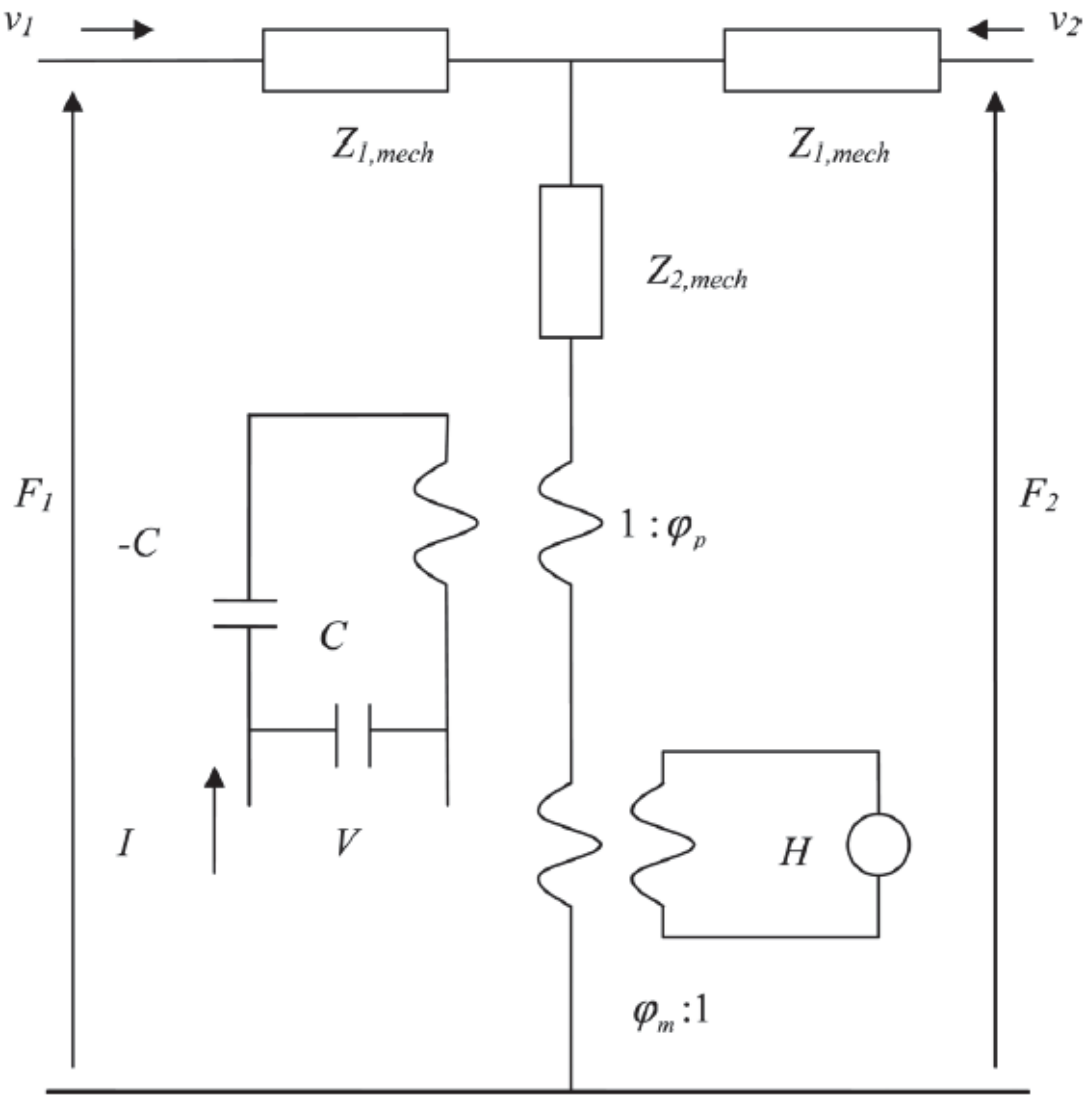


*Figure 1.13. Sketch view of the equivalent circuit of the ME sensor in L-L mode. Zhuang, Xin, et al. "Theoretical analysis of the intrinsic magnetic noise spectral density of magnetostrictive-piezoelectric laminated composites." Journal of Applied Physics 109.12 (2011): 124512, with fair use.*

At the resonance frequency, the equivalent circuit can be converted to the simplified one shown in Fig. 1.14. At low frequency, the electric charge and voltage outputs from the ME laminate are basically constant with frequency.[48] Therefore, the mechanical impedance can be expressed in the quasi-static condition $\omega \ll 2\pi f_r$ ($f_r$ is resonance frequency) as

$$Z^D_{mech} = Z_{1,mech} \,//\, Z_{1,mech} + Z_{2,mech} = -j\left(\frac{A_m}{s^H_{33,m}} + \frac{A_p}{s^D_{33,p}}\right)\frac{1}{vkl} . \quad (1.11)$$

If n is the thickness ratio (1.4), (1.11) can be modified as

$$Z^D_{mech} = -j\left(\frac{n}{s^H_{33,m}} + \frac{1-n}{s^D_{33,p}}\right)\frac{A}{\omega l} , \quad (1.12)$$

where $A$ is the total side surface area of the ME sensor. Similarly, we can use basic magnetostrictive and piezoelectric equations to obtain the equivalent circuit under constant electric field (close circuit).[47] As such, we can have both $Z^D_{mech}$ and $Z^E_{mech}$,

$$\begin{cases} Z^D_{mech} = -j\left(\frac{n}{s^H_{33,m}} + \frac{1-n}{s^D_{33,p}}\right)\frac{A}{\omega l} \\ Z^E_{mech} = -j\left(\frac{n}{s^H_{33,m}} + \frac{1-n}{s^E_{33,p}}\right)\frac{A}{\omega l} \\ j\omega C Z^D_{mech} = j\omega C Z^E_{mech} + \varphi_p^2 \end{cases} . \quad (1.13)$$

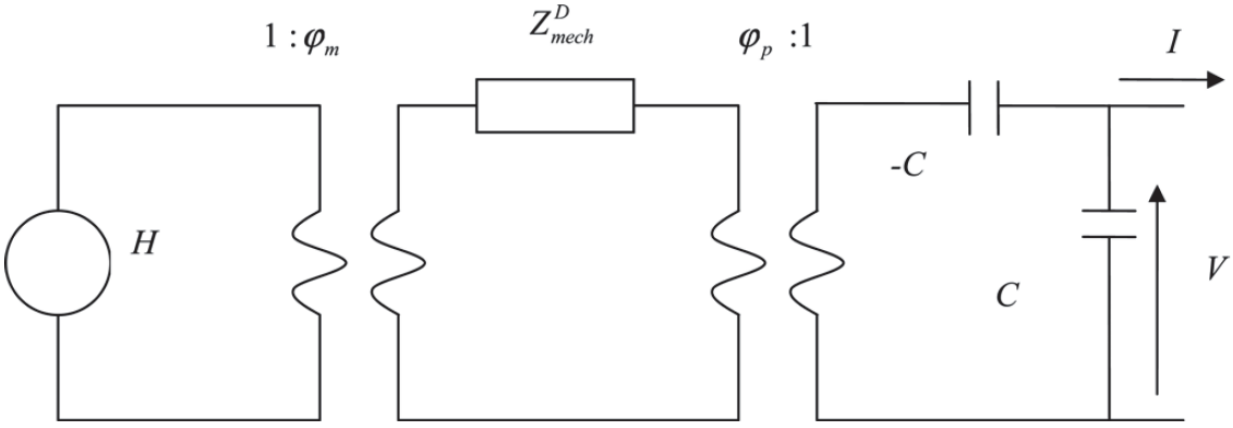


*Figure 1.14. Sketch view of the simplified equivalent circuit of the ME sensor in L-L mode under constant electric displacement (open circuit). Zhuang, Xin, et al. "Theoretical analysis of the intrinsic magnetic noise spectral density of magnetostrictive-piezoelectric laminated composites." Journal of Applied Physics 109.12 (2011): 124512, with fair use.*

Finally, we can have the expressions of ME voltage coefficient and ME charge coefficient with L-L mode configuration, which are shown below:

$$\begin{cases} \left|\frac{dV}{dH}\right| = \left|\frac{\varphi_m\varphi_p}{\varphi_p^2 + j\omega C Z^E_{mech}}\right| = \left|\frac{\varphi_m\varphi_p}{j\omega C Z^D_{mech}}\right| \\ \left|\frac{dQ}{dH}\right| = \left|\frac{1}{j\omega}\frac{dI}{dH}\right| = \left|\frac{\varphi_m\varphi_p}{j\omega Z^E_{mech}}\right| = \left|\frac{\varphi_m\varphi_p C}{j\omega C Z^E_{mech} - \varphi_p^2}\right| \end{cases} . \tag{1.14}$$

If we substitute $C$ $(= \frac{wt_p}{l}\varepsilon^S_{33})$ in (1.14), the ME voltage coefficient and ME charge coefficient in L-L mode configuration can be expressed as

$$\begin{cases} \left|\frac{dV}{dH}\right| = \frac{ng_{33,p}d_{33,m}l}{ns^D_{33,p} + (1-n)s^H_{33,m}} \\ \left|\frac{dQ}{dH}\right| = \frac{nd_{33,p}d_{33,m}wt_p}{ns^E_{33,p} + (1-n)s^H_{33,m}} \end{cases} . \tag{1.15}$$

Principally, there are two inherent sources of noise in ME laminates: dielectric loss noise ($N_{DE}$) and DC leakage resistance noise ($N_R$). Some other noise sources (e.g., thermal-magnetic noise and electric circuit noise) will not be addressed herein because of the even lower charge

noise density compared with $N_{DE}$ and $N_R$. The dielectric loss noise is related to the electric dissipation from ferroelectric domain wall motion.[49] The DC leakage resistance noise, also known as Johnson noise, is caused by the free electric charge random motion.[50] Both of these represent thermo-electric dissipations, which are the intrinsic source of loss. The two noise sources are expressed as:

$$N_{DE} = \sqrt{\frac{4kTC_p tan\delta}{2\pi f}} \tag{1.16}$$

$$N_R = \frac{1}{2\pi f}\sqrt{\frac{4kT}{R}} \tag{1.17}$$

The total intrinsic noise floor of ME laminate is

$$N_t = \sqrt{N_{DE}^2 + N_R^2} = \sqrt{\frac{4kTC_p tan\delta}{2\pi f} + \frac{1}{(2\pi f)^2}\frac{4kT}{R}} \tag{1.18}$$

where $k$ is the Boltzmann constant, $T$ is the temperature, $Cp$ is the internal electric capacitance of the ME sensor, $tan\delta$ is the dielectric loss, $f$ is the frequency, and $R$ is the DC resistance of the ME sensor. The measured samples we utilized were Metglas/PMN-PT/Metglas ME laminates in L-L multi-push-pull mode, which is exactly the same structure as shown in Fig. 1.8.

Prior experimental results are shown in Fig. 1.15.[18] As indicated in Fig. 1.15(a), the ME effect of the Metglas/piezoelectric layer exhibits DC magnetic bias-dependent behavior due to the fact that the ME coefficient is proportional to the piezomagnetic coefficient. These results show that the ME voltage coefficient increases initially with the DC magnetic bias increase, reaching a maximum value of 52 $Vcm^{-1}Oe^{-1}$. We list five reasons why the ME voltage coefficient is so high in this instance: (1) the optimized magneto-mechanical-electric coupling in multi-push-pull mode; (2) the high permeability and piezomagnetic constant of Metglas layers; (3) the high piezoelectric charge constant of the PMN-PT single crystal fibers compared with PZT ceramic fibers; (4) the optimized thickness ratio of the ME laminate; (5) the optimized interdigitated electrodes printing

on Kapton films. We then measured the equivalent magnetic noise (EMN) of the ME laminate using the conversion of the charge noise density divided by the ME charge coefficient, and those results are provided in Fig. 1.15(b). At 1 Hz, a significantly low EMN of 5.1 pT/√Hz was determined, which is very close to the predicted value of 4.2 pT/√Hz. With an extremely low charge noise density and an enhanced ME charge coefficient, a low EMN was achieved through the use of an ME laminate with a Metglas/PMN-PT sandwich structure.

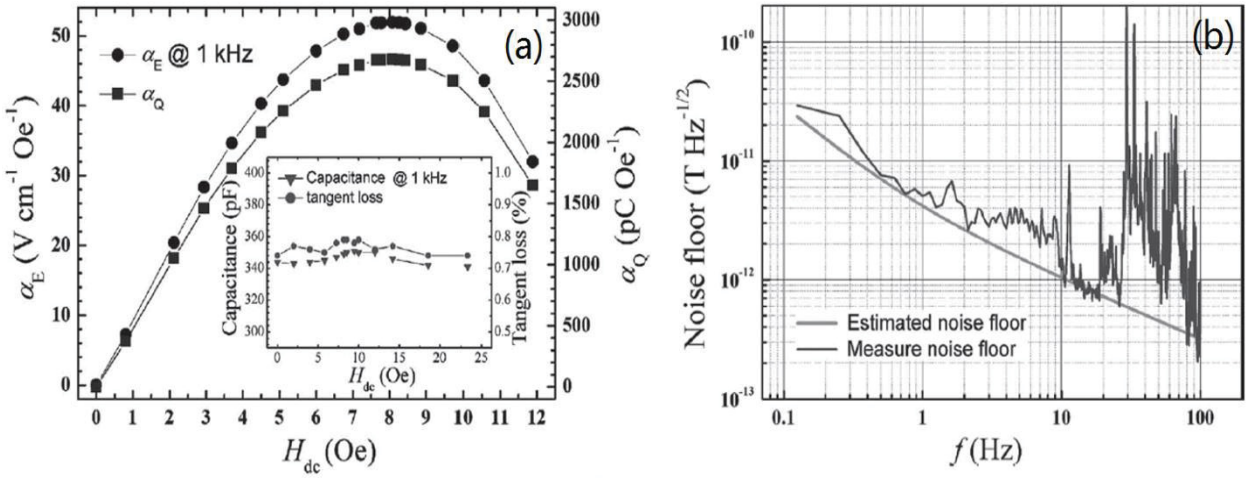


*Figure 1.15. (a) ME coefficients as a function of DC magnetic bias at non-resonance frequency, (b) Equivalent magnetic noise of Metglas/PMN-PT ME sensor. Wang, Yaojin, et al. "An extremely low equivalent magnetic noise magnetoelectric sensor." Advanced Materials 23.35 (2011): 4111-4114, with fair use.*

1.4.2. Active mode (H-field modulation) ME sensors.

While we know that dielectric loss noise and DC leakage resistance noise are both sources of thermo-electric noise based on fluctuation-dissipation theory, it is difficult to further decrease the noise floor due to existing fabrication methods for piezoelectric fibers. In order to overcome this limitation, some researchers have focused on using modulation techniques to enhance the performance of ME sensors with respect to lowering the noise floor.[51-53] The underlying principle at work here is that both dielectric loss noise and DC leakage resistance noise decrease as a function of frequency. By applying the modulation technique, the low-frequency reference signal can modulate a high-frequency excitation carrier signal around the first mechanical resonance frequency of the ME sensor. Then, the low-frequency reference signal can be separated from the carrier signal via the classic demodulation technique. Therefore, the only expected noise source should be near the frequency of the excitation carrier signal, with the noise caused by low-frequency thermo-electric dissipations able to be discounted. It must be noted that prior studies have indicated that there is still considerable noise around the excitation carrier signal after the demodulation process, which has yet to be fully explained.[53-56] Compared with the passive mode, another advantage of H-field modulation is that it can partially reject vibration noise due to the fact that the low-frequency signal shifts to high frequency.

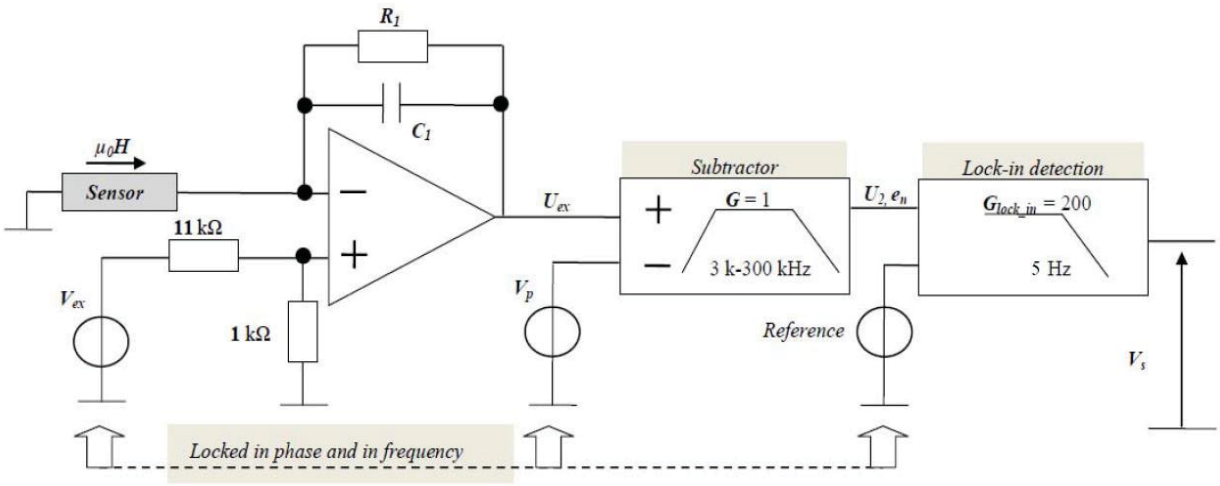


*Figure 1.16. Experimental sketch of H-field modulation and demodulation process. Zhuang, Xin, et al. "Sensitivity and noise evaluation of a bonded magneto (elasto) electric laminated sensor based on in-plane magnetocapacitance effect for quasi-static magnetic field sensing." IEEE Transactions on Magnetics 51.1 (2015): 1-4, with fair use.*

When the ME sensor is working in passive mode, the ME effect depends on the first order nonlinearity of the magnetostrictive phase. However, under H-field modulation, the ME effect will depend on the second order nonlinearity of the magnetostrictive phase. Figure 1.16 shows the modulation and demodulation process. The ME sensor is located within a coil, which provides a known high-frequency excitation signal. Simultaneously, an unknown low-frequency magnetic signal is applied to the ME sensor to generate a modulated signal. After this modulated signal is amplified, it is applied to a subtracting amplifier with a 3-300 kHz bandwidth to eliminate the low-frequency noise. Finally, the applied low-frequency magnetic signal is recovered through the demodulation process using the lock-in amplifier.[57]

Since H-field modulation uses the second order nonlinearity of the magnetic properties, the charge noise floor and the ME charge coefficient after the demodulation process can be expressed as,[42]

$$\begin{cases} q_{n\_demod}(f) = \frac{\kappa \varphi_m \varphi_p H_0}{2\pi f\, Z_{mech}} \sqrt{\frac{4kT\, tan(\delta_{mech})}{2\pi f C_{mech}} + 4kTR_{mech}} \\ \left|\frac{dQ}{dH}\right|_{demod} = \frac{\tau \varphi_m \varphi_p H_0}{2\pi f\, Z_{mech}} \end{cases}, \tag{1.19}$$

where $\kappa$ (= $s_{33}^{NL} / s_{33}$) and $\tau$ (= $d_{33}^{NL} / d_{33}$) are the mechanical nonlinearity and magnetic nonlinearity, respectively, $\tau/\kappa \approx 2\varphi_m$,[42] $H_0$ is the amplitude of the low-frequency magnetic signal, $R_{mech}$ (= $2\pi f_0\, m\, /\, Q_{mech}$) is the mechanical resistance, $C_{mech}$ (= $s_{33}l/\, wt_{lam}$) is the mechanical capacitance, $Z_{mech}$ (=$1\, /\, j2\pi f\, C_{mech}$) is the mechanical impedance, and $tan(\delta_{mech})$ (= $Re(Z_{mech})\, 2\pi f\, C_{mech}$) is the mechanical loss factor. Therefore, the EMN of an ME sensor working under H-field modulation can be expressed as,[42]

$$b_{n\_demod}(f) = \frac{\mu_0 \kappa}{\tau} \sqrt{\frac{4kT\, tan(\delta_{mech})}{2\pi f C_{mech}} + 4kTR_{mech}}\ . \tag{1.20}$$

Figure 1.17 provides comparison results of EMN using Metglas/PZT and Metglas/PMN-PT single crystals. For the PZT sample, the calculated (red) and measured (black) EMN were 58 pT/√Hz and 65 pT/√Hz, respectively. For the PMN-PT single crystal sample, the calculated (red) and measured (black) EMN were 30 pT/√Hz and 32 pT/√Hz, respectively. Theoretically, the EMN of the PMN-PT signal crystal sample could be even lower if the uniformity of the ME laminate and the growth process of the single crystal were enhanced.

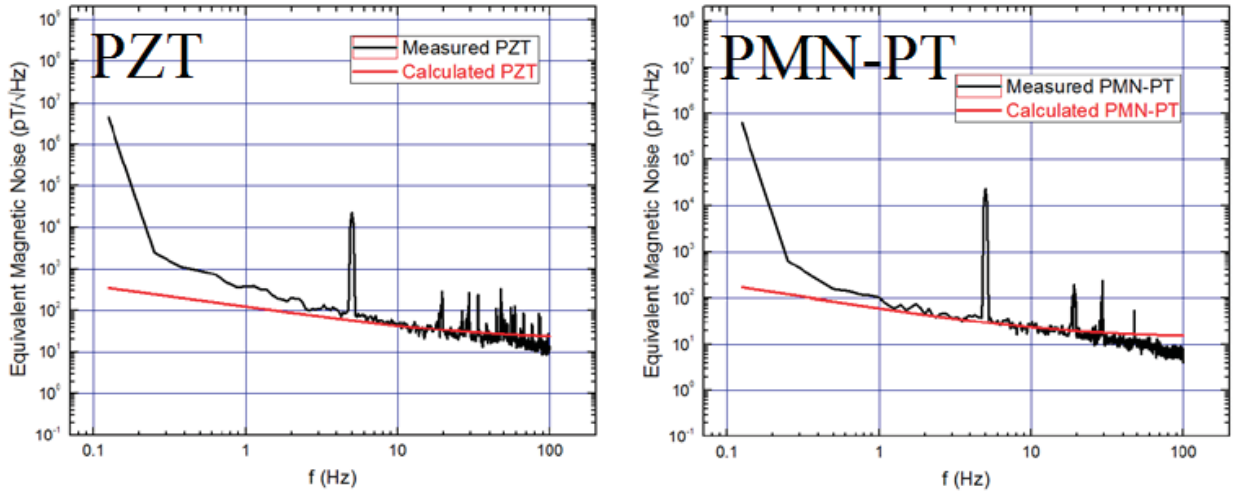


*Figure 1.17. Comparison results of EMN using Metglas/PZT and Metglas/PMN-PT.*

1.4.3. Advantages and disadvantages.

In this section, I summarize the advantages and disadvantages of both passive mode and active mode (H-field modulation) ME sensors. First, passive mode ME sensors that feature a Metglas/PMN-PT single crystal trilayer structure possess an extremely low noise floor of 5.1 pT/√Hz. The lowest consuming power level for the passive mode is only around a few μW using a simple circuit design. However, passive mode ME sensors are inherently affected by microphonic noise and electromagnetic interference, creating substantial noise at low frequency levels. This limitation restricts the application of passive mode ME sensors. Conversely, for active mode (H-field modulation) ME sensors, although the noise floor is higher, such sensors are able to overcome electromagnetic interference due the frequency shift modulation technique. Moreover, active mode ME sensors can partially reject some vibrational noise, especially transverse vibrational noise at low frequency, but they will still be affected by vibrational noise in the longitudinal direction. In actual applications, both passive and active mode ME sensors can detect the magnetic strength of the detected magnetic sources, but they cannot determine the distance

between magnetic source and ME sensors. Based on the various limitations of passive mode and active mode ME sensors, it is important to implement new approaches for addressing these problems, with the goal of enhancing their use in a range of applications.

## 1.5. Summary of this section

Over the past two decades, ME laminated composites have been modified using different materials, structures, and working modes to enhance the ME coefficient and reduce the noise floor. Currently, the ME sensors working under passive mode demonstrate extremely low noise floor and tremendously high ME coefficient in an absolutely quiet environment. However, in order to overcome the limitations for ME sensors that need to function well in an open environment, an H-field modulation ME sensor was developed that shows much lower sensitivity to a range of mechanical stimuli. As described in the next section of my dissertation, the vibration rejection of an ME sensor/gradiometer working under H-field modulation was achieved; a transmitter based on the ME laminate structure was developed, whose efficiency was shown to be several orders magnitude higher than an equivalent current loop; an ME gyrator application was also developed, which achieved impedance matching and resonance frequency tuning.

# CHAPTER 2: PURPOSE OF DISSERTATION

In the prior section of this thesis, I summarize the advantages and disadvantages of both passive and active mode (H-field modulation) ME sensors. Accordingly, the goal of this thesis investigation was to optimize the properties of ME heterostructures for improved usage in three types of applications: sensing in open environment with rejection of microphonics, the wireless transmission of power, and gyration.

**(1) Detection properties of ME sensors.**

In order to reject vibrational noise, we developed two ME sensors with closely matched transfer functions and noise floors; we then formed an ME gradiometer by placing these two sensors across a baseline. This ME gradiometer worked well under H-field modulation. Previous studies have indicated that a passive mode ME gradiometer can be used for low-frequency sensing applications, but is notably impacted by ambient microphonic noise that can significantly reduce the distance at which a magnetic source can be detected. Accordingly, this active mode ME gradiometer working under H-field modulation represents an important development for achieving enhanced vibration-rejection efficiency. Moreover, this ME gradiometer can inherently reject the common mode sources in parallel mode with high efficiency. When the ME gradiometer is in line mode configuration, the output difference between two ME sensors can then be used to determine the distance between the gradiometer and a magnetic source.

**(2) Low frequency laminate properties of ME heterostructures.**

The developed ME laminate was used as a transmitter and a search coil served as a receiver. Using the converse ME effect, a voltage was applied to the piezoelectric layer of the ME heterostructure, which then induced a polarization change in the piezoelectric layer. Subsequently, a shape change was generated in the piezoelectric layer, which was then transmitted to the

magnetostrictive layer, ultimately resulting in a magnetic flux output that could be detected through the use of a search coil as a receiver. The frequency transmitter and receiver were that of the resonance frequency of the ME heterostructure, at which point the ME effect was enhanced and the power output was the highest. I then compared the performance of my ME laminate transmitter with a small-circuit loop with the same surface area, confirming that it demonstrated $10^4$ times higher efficiency.

**(3) Gyration properties of ME heterostructures.**

Our group has recently developed an ME gyrator that features an ME heterostructure located in the center of a search coil. This device can convert a magnetic input to an electric output, and vice-versa. Near the mechanical resonance frequency, the ME heterostructure exhibits a giant ME effect. By optimizing the materials and dimensions of the ME gyrator, a 90% power efficiency level has been achieved. In real applications, a transducer will typically have an impedance mismatch problem with the power supply, which will create a significant reduction in the entire transducer device system. Accordingly, this investigation was also designed to determine how an ME gyrator can help address the impedance mismatch between a piezoelectric transducer and a power supply.

# CHAPTER 3: ME GRADIOMETER WITH ENHANCED VIBRATION REJECTION

## 3.1. Introduction.

Gradiometers have been widely used in applications requiring magnetic field/flux detection.[58-61] Based on the above-mentioned advantages of ME sensors, magnetometers have been developed that consist of a pair of ME sensors. Previously, gradiometers based on two passive ME sensors were studied for use in low-frequency sensing applications.[59] As noted, passive mode ME sensors are capable of detecting low-frequency signals. Coupling between piezoelectric and magnetostrictive layers can be achieved through the application of mediating mechanical stress/strain. Since the piezoelectric layers are inherently sensitive to mechanical stimuli, the ME composite also partially picks up microphonic noise. Unfortunately, this noise can be substantial at lower frequencies, which represents a major limitation of passive ME sensors. Thus, it is important that gradiometers be capable of rejecting microphonics.

Previously, Xing et al. showed that microphonics could in part be rejected by built-in structures that included an acoustic gradiometer, which was effectively incorporated into a magnetic sensor.[62] The differential output was shown to double the ME gain coefficient while providing some rejection of microphonics. In terms of the noted "built-in" approach, the gradiometer could be operated simply by adding/subtracting signals in an analog manner. Higher rejection efficiencies would require more precise matching of the sensor sizes and signal outputs, or computational analysis.

To overcome these limitations, Zhuang et al. developed an active mode ME sensor driven under H-field modulation that used a frequency shift modulation technique.[52] The ME composites were excited by an external sinusoidal signal; and when this signal is a harmonic of the magnetic field signal, it is designated as an H-field modulation.[63] An applied low-frequency magnetic signal

then modulates the excitation signal via the nonlinearity of the magnetostrictive layer of the laminate, producing two side-band signal peaks around the excitation signal frequency in the spectrum similar to a classic amplitude modulation (AM) method.[56,64] It is known that there are two principal noise sources that contribute profoundly to the total equivalent magnetic noise spectral density level.[47] The first noise source is in the piezoelectric layer, which is a Johnson noise that results from free electric charge random motion; the second is the dielectric loss noise related to the electric dissipation from ferroelectric domain wall motion. These two noise sources belong to the category of thermo-electric dissipations, and both represent intrinsic sources of loss.[65] It is difficult, therefore, to lower the equivalent magnetic noise spectral density level by only considering the piezoelectric layer construction and passive detection. Accordingly, modulation techniques have been developed to overcome these limitations.

Using H-field modulation, a low frequency magnetic field to be sensed modulates an excitation carrier signal that is applied on the ME laminate at a higher frequency.[52] The low-frequency output signals can then be separated from the carrier by means of classic demodulation techniques.[66] Accordingly, the only expected noise is the one near the frequency of the excitation carriers, and thus the noise contribution from the low-frequency thermo-electric dissipations are removed. Furthermore, this process enables the H-field modulation to also partially reject low-frequency vibration noises. The EMN is converted from the output electric noise spectral density by dividing the transfer function of the ME sensor. On the other hand, there are three notable limitations associated with H-field modulation: (a) its power consumption is significantly higher in comparison to the passive mode, (b) it requires continuous drive, and (c) its associated detection circuity is much more complicated when compared to passive mode.

To date, a gradiometric pair of ME sensors operated under H-field modulation has yet to be reported. However, such an approach represents a potentially important way by which the rejection efficiency of microphonics may be increased. Accordingly, we constructed and tested a gradiometer consisting of a pair of ME sensors operating in the active mode by H-field modulation. Our investigation focused on the common mode rejection ratio (CMRR) of this ME gradiometer, with results indicating that this pair of H-field modulation sensors enhanced vibration rejection efficiency compared to a single ME sensor in both passive or modulation working modes.

## 3.2. Common mode rejection ratio and spatial transfer function.

In this section, several benchmarks of gradiometers will be introduced, such as differential and common mode gains, common mode rejection ratio, and the spatial transfer function. In addition, a basic theoretical analysis on these benchmarks will be provided via demonstrations of the essential parameters of the proposed gradiometer. The primary working mode of a gradiometer is based on its ability to detect the gradient output $\Delta V/V_1$ as a function of the normalized distance $D/d$, as shown in Fig. 3.1. Note that $\Delta V$ is the difference between the voltage output of ME sensor 1 ($V_1$) and the voltage output of ME sensor 2 ($V_2$), $D$ is the distance between magnetic moment and gradiometer, and $d$ is the baseline of the gradiometer. For a given value of the baseline $d$, the working regime is between a start point $D_{start}$ and an end point $D_{end}$ and limited by the value of 1/CMRR.

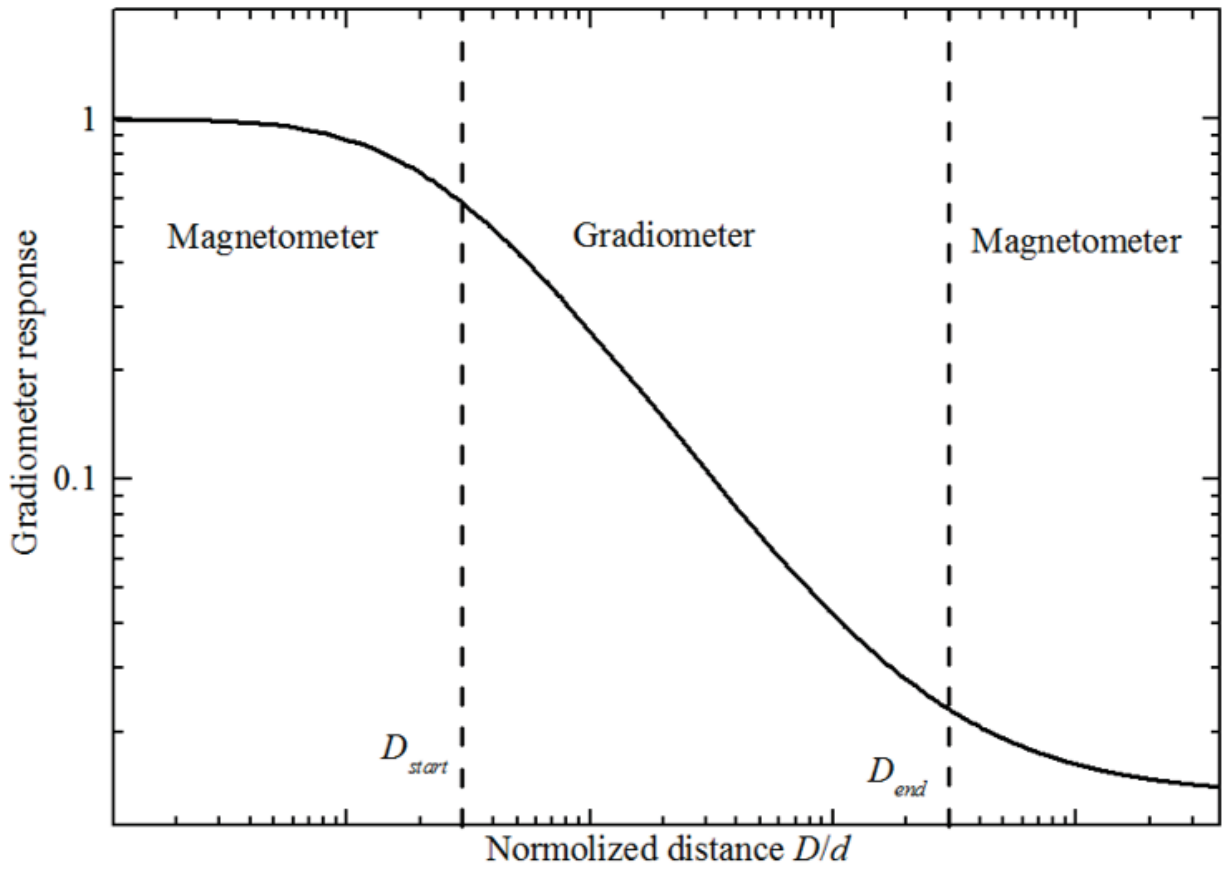


*Figure 3.1. Ideal gradiometer response curve. Xu, Junran, et al. "Magnetoelectric gradiometer with enhanced vibration rejection efficiency under H-field modulation." Journal of Applied Physics 123.10 (2018): 104501, with fair use.*

A. Common mode rejection ratio

The common mode rejection ratio of a magnetic gradiometer is defined as the ratio of the amplitudes of differential mode outputs over a common mode output in a homogenous field; more succinctly, it can be expressed as the ratio between the differential mode and the common mode gains. By applying a magnetic field $H$ on the gradiometer, the detected magnetic flux density can be expressed as $B=\mu_0 H$. This magnetic signal is amplified by the first and second magnetometers,

producing the two output voltage signals *V1(=Tr1×B1)* and V2(=Tr2×B2), as shown in Fig. 3.2. The output voltage of the gradiometer can then be given as:

$$\begin{aligned} V_{out} &= \vec{T}_{r1} \times B_1 + \vec{T}_{r2} \times B_2 \\ &= \vec{T}_{r\_d} \left( B_1 - B_2 \right) + \vec{T}_{r\_cm} \left( \frac{B_1 + B_2}{2} \right) \end{aligned} \tag{3.1}$$

where we used a common formula that expresses the output voltage as a differential mode gain $\vec{T}_{r\_d} = \frac{\vec{T}_{r1} - \vec{T}_{r2}}{2}$ and a common mode gain $\vec{T}_{r\_cm} = \vec{T}_{r1} + \vec{T}_{r2}$ . The arrows indicate that the symbols have both amplitude and phase contributions. We introduced a phase shift of 180° in the following equations. In practice, there are differences between the first and second magnetometers with respect to their phases and gains, as expressed in Equation 3.2:

$$\begin{cases} \Delta T_r = \left| T_{r1} - T_{r2} \right| \\ \varphi = \varphi_{r1} - \varphi_{r2} \end{cases} \tag{3.2}$$

Thus, the differential mode and common mode gains can be given as:

$$\begin{cases} T_{r\_d} = \dfrac{\sqrt{\left(T_{r1}\right)^2 + \left(T_{r2}\right)^2 - 2T_{r1}T_{r2}\cos\left(\pi - \varphi\right)}}{2} \\ T_{r\_cm} = \sqrt{\left(T_{r1}\right)^2 + \left(T_{r2}\right)^2 + 2T_{r1}T_{r2}\cos\left(\pi - \varphi\right)} \end{cases} \tag{3.3}$$

While the CMRR can be calculated by:

$$CMRR = \frac{T_{r\_d}}{T_{r\_cm}} = \frac{\sqrt{\left(T_{r1}\right)^2 + \left(T_{r2}\right)^2 + 2T_{r1}T_{r2}\cos\left(\varphi\right)}}{2\sqrt{\left(T_{r1}\right)^2 + \left(T_{r2}\right)^2 - 2T_{r1}T_{r2}\cos\left(\varphi\right)}} \tag{3.4}$$

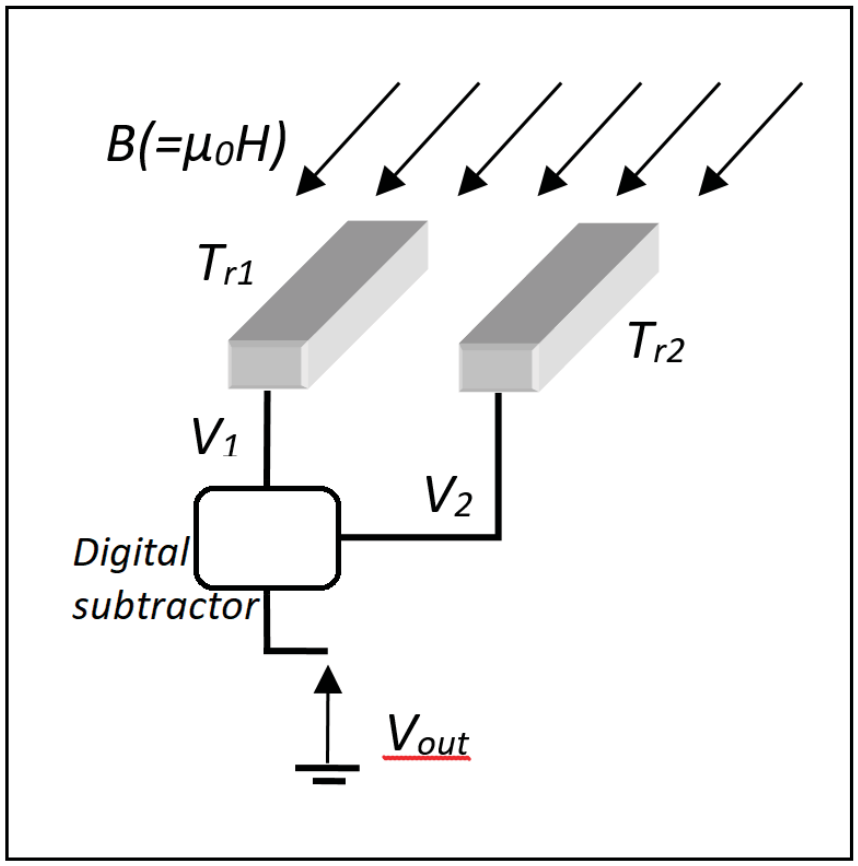


*Figure 3.2. Scheme of two ME sensors with a subtractor. Xu, Junran, et al. "Magnetoelectric gradiometer with enhanced vibration rejection efficiency under H-field modulation." Journal of Applied Physics 123.10 (2018): 104501, with fair use.*

Experimental data have indicated that the phase shift between the two active mode ME sensors was nearly zero. There is a component of our LabView program that can generate the phase difference between channel 1 and channel 2. The phase difference values for every second obtained over a period of 5 sequential seconds was measured, with the following results: -1.43, -1.02, 358.31, -0.81 and -0.83 degrees. As can be seen, all of them could be found near 0° or 360°. Thus, the CMRR can be simplified to the following equation:

$$CMRR = \frac{T_{r\_d}}{T_{r\_cm}} = \frac{T_{r1} + T_{r2}}{2\left(T_{r1} - T_{r2}\right)} \approx \frac{T_{r1}}{\Delta T_r} = \frac{T_{r1}}{\Delta T_r} \tag{3.5}$$

By placing the pair of sensors in a common magnetic field, the CMRR can also be measured according to the following expression:

$$CMRR = \frac{T_{r1} B_1}{\Delta T_r B_1} = \frac{V_1}{V_1 - V_2} = \frac{V_1}{\Delta V} \tag{3.6}$$

B. Spatial transfer function

The spatial transfer function defines the gradient response of a magnetic gradiometer as a function of the distance between the gradiometer and a magnetic target. An axial gradiometer consists of two sensors aligned with a baseline *d*, as shown in Fig. 3.3. In the following section we will show the theoretical formula of a gradient response for an axial gradiometer, and then compare simulated data using this formula with experimentally obtained data. The absolute value of the magnetic flux density generated by a magnetic moment with a distance *D* along the perpendicular direction can be written as:

$$B = \frac{\mu_0}{2\pi} \frac{m}{D^3} \text{ [T] } ; \tag{3.7}$$

where m is the absolute value of a magnetic moment, *D* is the distance between the magnetic moment and the gradiometer.

The output voltage values of the first and second sensors, and the difference between the two sensors, can be given as:

$$\begin{cases} V_1 = B_1 \cdot T_{r1} = \dfrac{\mu}{2\pi}\dfrac{m}{D_1^3} \cdot T_{r1} = \dfrac{\mu}{2\pi}\dfrac{m}{D_1^3} \cdot \left( T_{r2} + \Delta T_r \right) \\ V_2 = B_2 \cdot T_{r2} = \dfrac{\mu}{2\pi}\dfrac{m}{D_2^3} \cdot T_{r2} \\ V_3 = V_2 - V_1 = \dfrac{\mu m}{2\pi}\left[ \left( \dfrac{1}{D_1^3} - \dfrac{1}{\left(D_1 + d\right)^3} \right) T_{r2} + \dfrac{\Delta T_r}{D_1^3} \right] \end{cases} \tag{3.8}$$

where $D_1$ is the distance between magnetic source and first ME sensor, $D_2$ is the distance between magnetic source and second ME sensor, and $\Delta Tr$ $(= Tr_2 - Tr_1)$ is the difference of the transfer function between the two sensors. Thus, the spatial transfer function of the gradiometer can be derived as:

$$\begin{aligned} STF &= \left| \frac{V_3}{V_1} \right| = \left| \frac{\dfrac{\mu m}{2\pi}\left[ \left( \dfrac{1}{D_1^3} - \dfrac{1}{\left(D_1 + d\right)^3} \right) T_{r2} + \dfrac{\Delta T_r}{D_1^3} \right]}{\dfrac{\mu m}{2\pi}\dfrac{T_{r1}}{D_1^3}} \right| \\ &= \left| \frac{\left( 1 - \dfrac{D_1^3}{\left(D_1 + d\right)^3} \right) + \dfrac{\Delta T_r}{T_{r2}}}{1 + \dfrac{\Delta T_r}{T_{r2}}} \right| \end{aligned} \tag{3.9}$$

When the magnetic moment is close to the gradiometer, the STF is unified; however, when the magnetic moment is far enough from the magnetic gradiometer, ($D_1 >> d$), the STF becomes:

$$STF = \left| \frac{\Delta T_r}{T_{r1}} \right| = \left| \frac{\Delta T_r}{T_{r2}} \right| = \frac{1}{CMRR} \tag{3.10}$$

In practice, another factor that limits detection performance is associated with non-common noise, such as the intrinsic noise of the sensors. Using a gradiometer with a sufficiently enhanced CMRR value, a sensor's intrinsic noise level determines the ultimate performance of the gradiometer for measuring the gradient in an unknown magnetic environment.

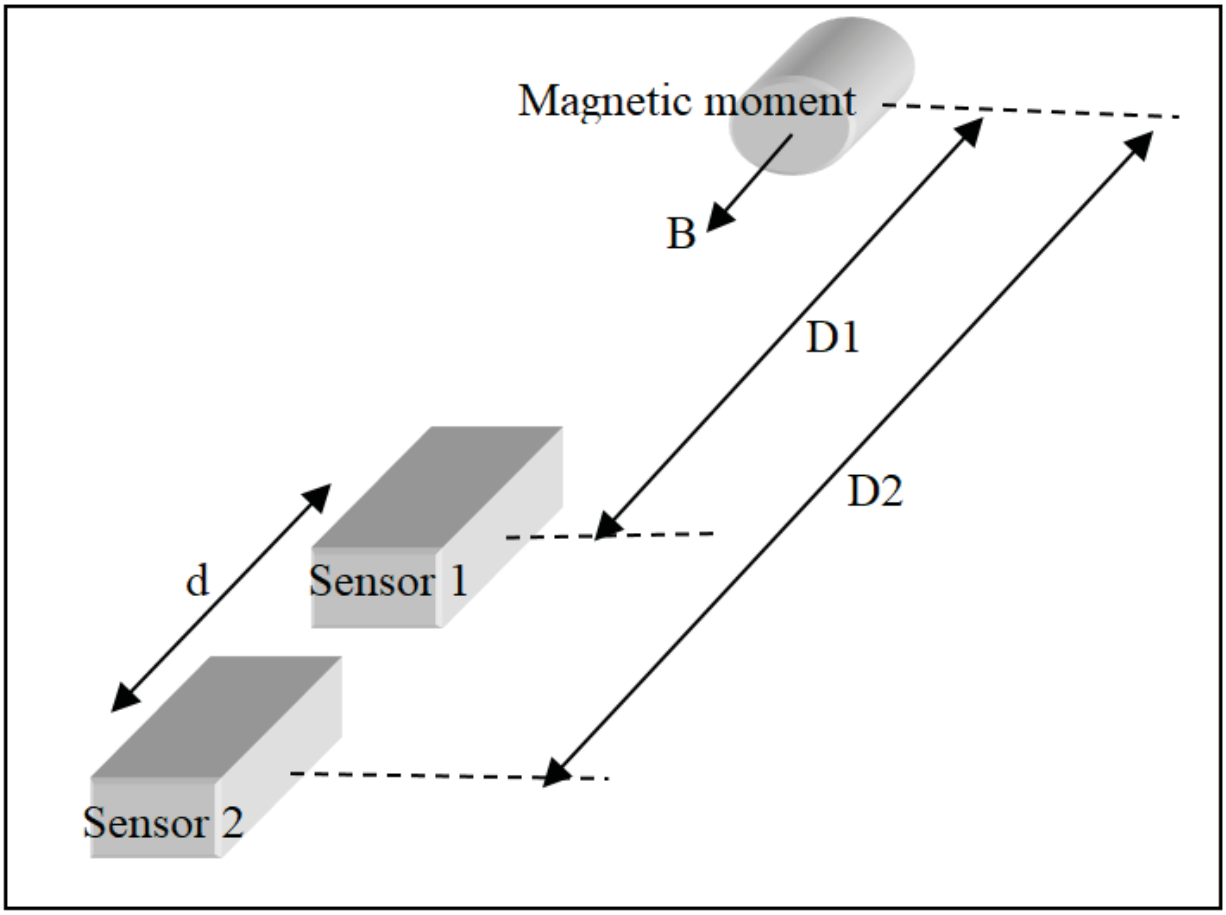


*Figure 3.3. Scheme of an ME gradiometer and a magnetic moment. Xu, Junran, et al. "Magnetoelectric gradiometer with enhanced vibration rejection efficiency under H-field modulation." Journal of Applied Physics 123.10 (2018): 104501, with fair use.*

## 3.3. Structure and working principle.

The proposed ME gradiometer is composed of two ME laminate sensors that are similar in size, weight, structure, and equivalent magnetic noise level. A PZT piezoelectric layer made of five 40mm-long macro-fibers in parallel was bonded between two 80 mm long Metglas layers using epoxy, where each layer consisted of three Metglas foils that were stacked and joined using epoxy. The PZT/PMN-PT fibers were poled in the longitudinal direction through the use of interdigital electrodes applied on both the top and bottom of these fibers. The intrinsic equivalent magnetic noise (EMN) levels of the two ME sensors were 60 pT/√Hz and 65 pT/√Hz at 5 Hz, respectively, when using two independent drive coils with sections measuring 730mm$^2$. The center-to-center distance between the two ME sensors was defined as the baseline of the gradiometer. By varying the values of the baseline, we were able to investigate the CMRR of the proposed gradiometer, which refers to its capacity to reject common mode signals/noise. As shown in Fig. 3.1, the baseline of the ME gradiometer determined the starting point $D_{start}$, which was the position at which the ME gradiometer is able to detect the gradient signals. The smaller the baseline, the closer the position at which the gradiometer can start to work. The closest baseline can be determined by taking into account sensor geometry and the interference between the two sensors. For this study, the baseline was chosen to have values of 15 cm, 20 cm, and 25 cm. For all these values, negligible crosstalk effects were found. As a general definition, the ending point $D_{end}$ of the gradiometer curve represents the farthest distance that the ME gradiometer can detect away from a magnetic target that causes a magnetic field disturbance in the environment before the signal falls below the noise floor. Theoretically, the farthest detection distance is determined by both the CMRR of the gradiometer and the EMNs of the ME sensors in the gradiometer.

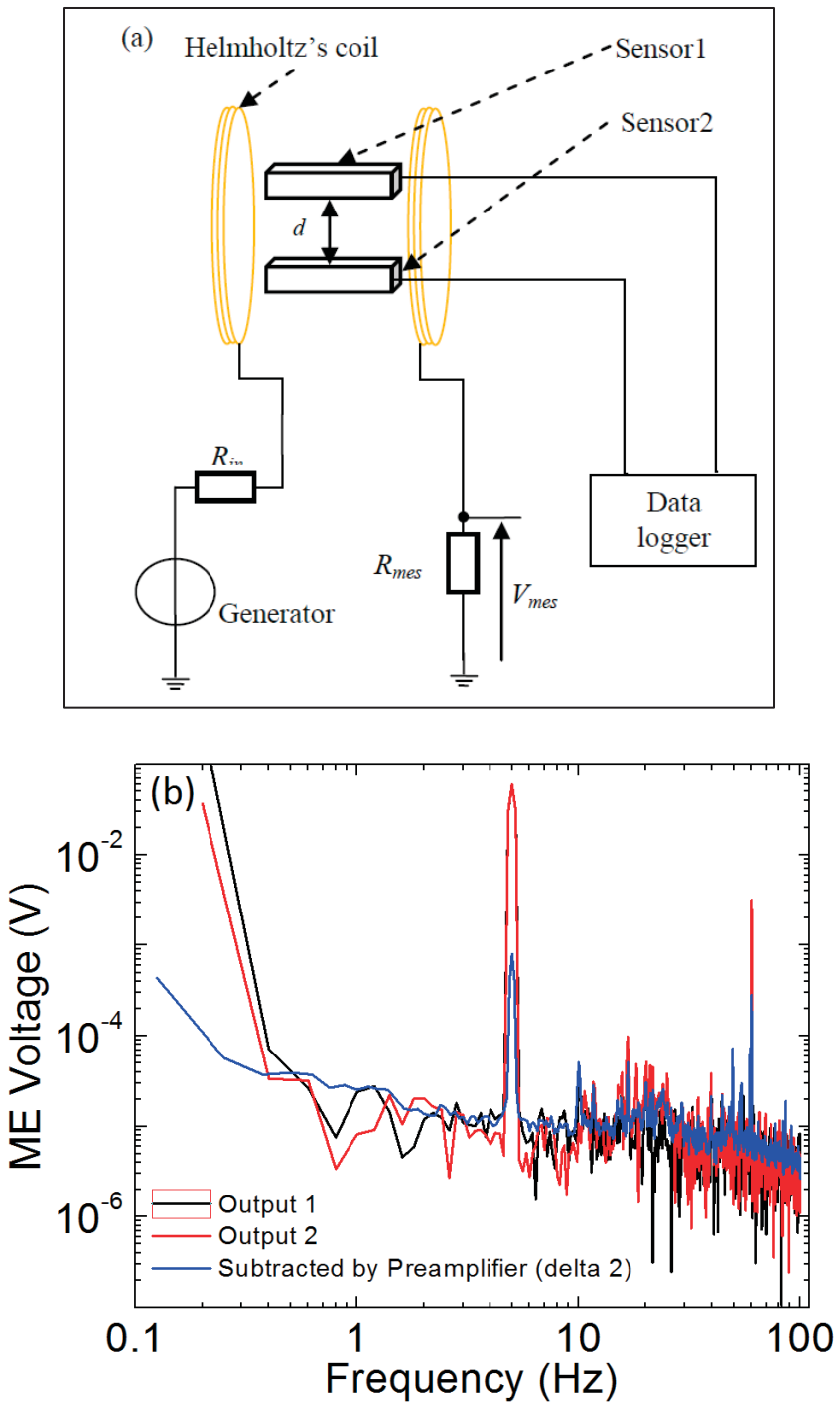


*Figure 3.4. (a) Experimental setup for CMRR measurement, (b) outputs from two ME sensors and their difference. Xu, Junran, et al. "Magnetoelectric gradiometer with enhanced vibration rejection efficiency under H-field modulation." Journal of Applied Physics 123.10 (2018): 104501, with fair use.*

The CMRR was measured by applying a homogenous magnetic field simultaneously to both active ME sensors. The two ME sensors were located in parallel within a Helmholtz coil that provided an AC magnetic signal of 110nT at 5 Hz, as shown in Fig. 3.4(a). Based on Equation (3.6), the CMRR can be calculated as the amplitude of the output signal over the difference between the two sensors, yielding,

$$CMRR = \frac{V_1}{V_1 - V_2} = \frac{V_1}{\Delta V} \quad . \tag{3.11}$$

Correspondingly, the predicted maximum CMRR for our sensor pair was measured to be 74, which was calculated from the data in Fig. 3.4(b). The farthest distance by which the ME gradiometer can detect a signal is dependent on the minimum difference between the two sensors in amplitude and in phase, presented as the value of 1/CMRR. Furthermore, a higher intrinsic noise floor for the two individual ME sensors may limit their detection performance—especially in the case of small amplitude magnetic fields. Therefore, there are different external noise levels in different environments. In order to efficiently reject the common mode external noise, a minimum CMRR is required.

By dividing the noise floor results for the ME sensors measured outside of a shielding chamber by the analogous data within the chamber (intrinsic EMN of the ME sensors), one can then estimate the minimum required value of the CMRR for the proposed ME gradiometer working in this environment, which afford the following relationship:

$$CMRR_{required} = \frac{\text{External noise level}}{\text{Sensors' intrinsic noise level}} \quad .$$

The noise floors of our two ME sensors measured in a shielding chamber were determined to be 60 pT/√Hz and 65 pT/√Hz at 5 Hz. The analogous noise floor data obtained out of the chamber

were 189 pT/√Hz and 314 pT/√Hz at 5 Hz. Accordingly, the required minimum CMRR of our ME gradiometer was determined to be a ratio of 4.8 in this noise environment. The gradient sensitivity is defined as a ratio of the output of a gradiometer over the gradient of the magnetic signals detected by the gradiometer. Taking into account that the transfer function of the two sensors was similar, (i.e., $Tr_2 \approx Tr_1$), the formula of the gradient sensitivity can be given as:

$$\begin{aligned} T_{r\_Gradient} &= \frac{V_2 - V_1}{(B_2 - B_1)/d} \\ &= \frac{T_{r1}(B_2 - B_1)}{(B_2 - B_1)/d} = T_{r1} d \ [\mathrm{V}/(\mathrm{T}/\mathrm{m})] \end{aligned} . \tag{3.12}$$

Thus, the detection performance can be predicted to have a value around 260-433 pT/m/√Hz using the baselines in our proposed active ME gradiometer; these values were derived from the equation of (The intrinsic noise floor of gradiometer) / (The baseline of gradiometer). Fig. 3.5(a) shows the experimental configuration that we utilized to measure the gradiometer's spatial response curve, where *d* was the baseline and *D* was the distance between the gradiometer and the magnetic moment. A small coil with a size of ~16 mm in diameter and a thickness of ~11 mm served as the magnetic moment. The intensity of the magnetic source used in the measurements was assessed to be about 50 μT. The expected curves based on (3.9) are given as dashed lines by using different values of the baseline.

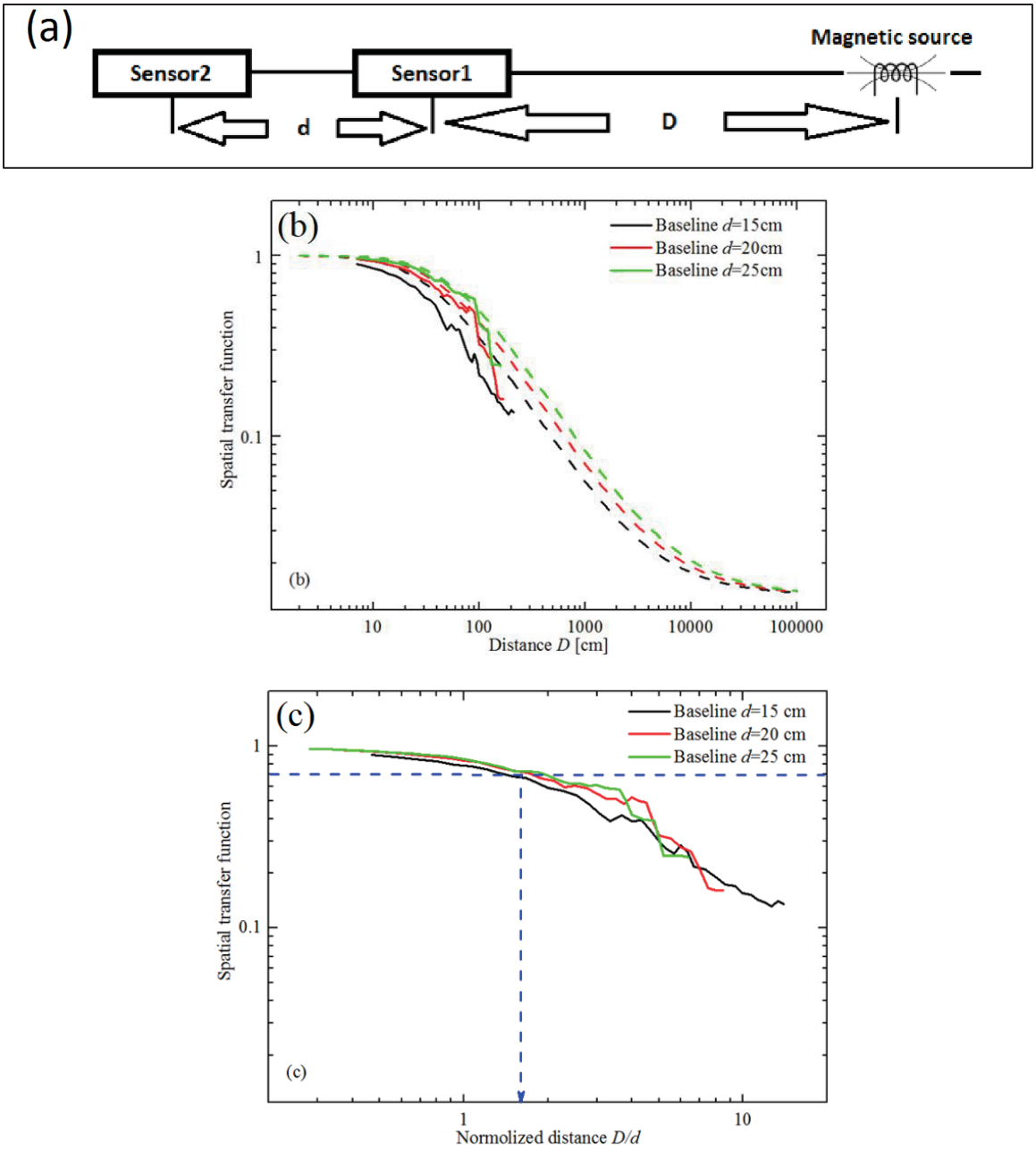


*Figure 3.5. (a) Experimental setup for gradiometer response curve measurement, (b) Gradiometer response curve as a function of distance between ME gradiometer and magnetic source, and (c) Gradiometer response curve as a function of distance between ME gradiometer and magnetic source normalized to baseline. Xu, Junran, et al. "Magnetoelectric gradiometer with enhanced vibration rejection efficiency under H-field modulation." Journal of Applied Physics 123.10 (2018): 104501, with fair use.*

During the process of measuring the gradiometric response curve, the magnetic source was gradually moved further away from the ME gradiometer. The voltage outputs from the two sensors were then simultaneously recorded by a data logger (National Instrument), which was controlled using a LabView program. Figs. 3.5(b) and 3.5(c) show the gradiometeric response curves with baselines of 15 cm, 20 cm, and 30 cm, where the difference between the outputs of the two sensors is along the vertical axis. The horizontal axis in (b) is the distance over which the gradiometer signal detection was measured; whereas in (c), the horizontal axis is the ratio of the distance *D* normalized over the baseline of the gradiometer. As indicated in Fig. 3.5(b), the longer the baseline, the further the distance that the gradiometer can detect a magnetic signal. Conversely, the shorter the baseline, the closer the begining point is at which the gradiometer can begin to work in its gradient regime, as shown in Fig. 3.5(c). When normalized to *D/d*, these three curves nearly overlapped, where the blue line is the -3dB point when it crosses the gradiometer response curves. Note that the intersection on the horizontal axis occurred near *D/d*=1, which is consistent with predictions that our ME gradiometer behaves similarly to a first-order gradiometer.[67] The limiting factor for the gradiometer performance is linked to when the response curves crosses the EMN floor in that sensors with a lower EMN will allow for a longer detection distance. In contrast, the farthest distance is set by the CMRR and the intrinsic noise of this gradiometer.

## 3.4. Experimental setup and vibration rejection efficiency.

Magnetoelectric gradiometer measurements using passive mode ME sensors were previously reported by Shen et al.[59] It should be noted that their ME gradiometer was stationary during magnetic source detection, thus reducing the introduction of low-frequency mechanical vibrations. For this investigation we compared an ME gradiometer working under H-field modulation with

another working in passive mode. We found that the vibration rejection of an ME gradiometer working under H-field modulation was significantly higher than its passive-mode counterpart. Two experiments were performed, whose results are presented in the following paragraphs. The first experiment measured the vibration rejection ratio of the ME gradiometer working under H-field modulation. The second test was designed to determine how an ME sensor working under H-field modulation compares to an ME sensor working in passive mode, which enabled the measurement and comparison of their CMRR values.

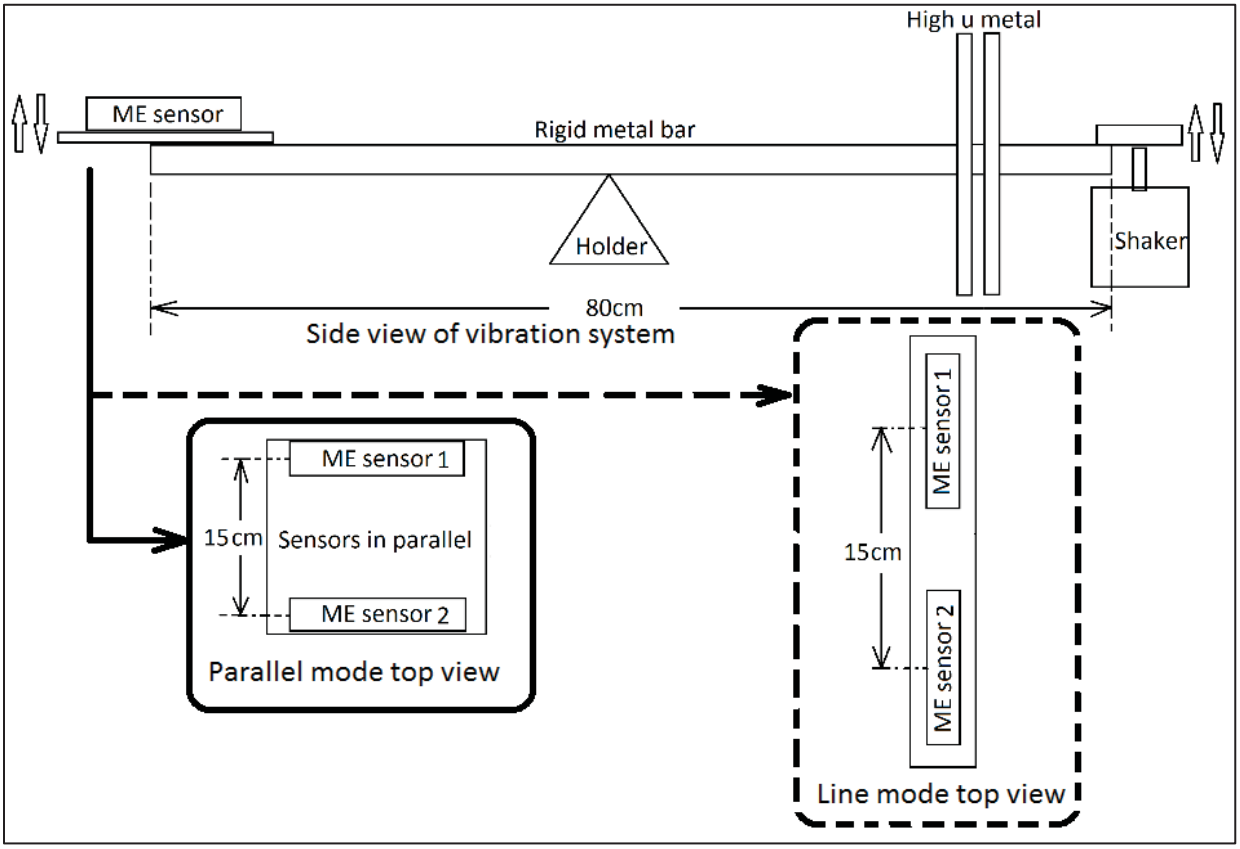


*Figure 3.6. Experimental setup for vibration rejection ratio measurement of ME gradiometer in parallel mode and line mode. Xu, Junran, et al. "Magnetoelectric gradiometer with enhanced vibration rejection efficiency under H-field modulation." Journal of Applied Physics 123.10 (2018): 104501, with fair use.*

Figure 3.6 shows the experimental setup for obtaining vibration-rejection measurements, which we designate as E1. The gradiometer was located on a stiff plastic board for both parallel (solid line) and serial (dash line) sensor configurations. In both cases, the baselines were 15 cm, which is the same as shown in Fig. 3.5(a). The plastic board with the ME gradiometer was fixed to one end of a rigid aluminum bar, while the other end was connected to a shaker. The shaker was then excited by a common mode 5 Hz vibration through the bar. Additionally, two pieces of high μ metal were placed next to the shaker to avoid the effect of DC magnetic fields generated from the shaker. Using the experimental setup of E1, vibrations of three different amplitudes were applied constantly on the gradiometer from the shaker. This approach was conducted for both the parallel and serial configurations of the sensors. Using a fluxgate magnetometer, we were able to characterize these vibrations as an equivalent magnetic flux density (EMFD). This approach allowed all output voltages from the ME gradiometers, which were generated by the vibration sources applied to the gradiometer, to be converted to an EMFD value. Accordingly, the EMFD was calculated in this way:

$$EMFD = \frac{\text{Fluxgate output voltage}}{\text{Fluxgate's transfer function}}\ [\text{T}]. \tag{3.13}$$

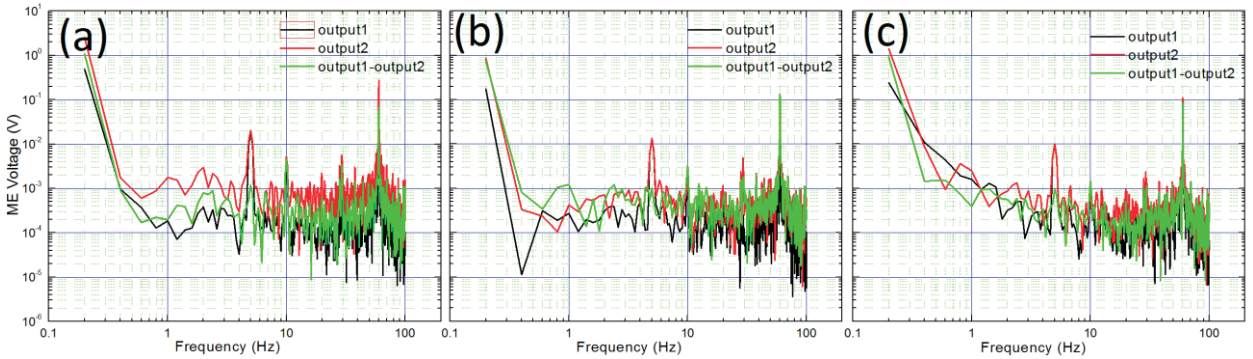


*Figure 3.7. Outputs of the two ME sensors and their corresponding subtractions under different vibrations for parallel mode. (a) Vibration amplitude equivalent to 15 nT magnetic flux density. (b) Vibration amplitude equivalent to 10 nT magnetic flux density. (c) Vibration amplitude equivalent to 7.8 nT magnetic flux density. Xu, Junran, et al. "Magnetoelectric gradiometer with enhanced vibration rejection efficiency under H-field modulation." Journal of Applied Physics 123.10 (2018): 104501, with fair use.*

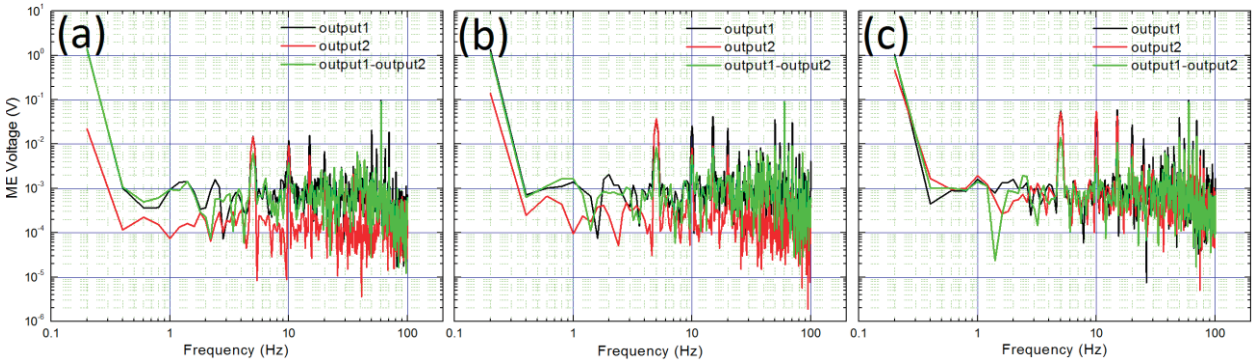


*Figure 3.8. Outputs of two ME sensors and their corresponding subtractions under different vibrations for line mode. (a) Vibration amplitude equivalent to 25 nT magnetic flux density. (b) Vibration amplitude equivalent to 19 nT magnetic flux density. (c) Vibration amplitude equivalent to 15 nT magnetic flux density. Xu, Junran, et al. "Magnetoelectric gradiometer with enhanced vibration rejection efficiency under H-field modulation." Journal of Applied Physics 123.10 (2018): 104501, with fair use.*

The vibration rejection ratio (VRR) was determined by using (3.11), and resulting data are shown in Fig. 3.7 and Fig. 3.8. As indicated in Fig. 3.7, the three distinct vibration amplitudes that were applied to the gradiometer resulted in EMFD values of 15nT, 10nT and 7.8nT for a gradiometer with a parallel sensor configuration. The corresponding vibration rejection ratios for these three vibration amplitudes were 17.4, 13.4, and 10.7, respectively. Fig. 3.8 provides the vibration rejection ratios obtained by means of an ME gradiometer with sensors in a serial configuration. As in the case of the parallel sensors, similar vibrations were applied, resulting in EMFD values of 25nT, 19nT and 15nT. The corresponding vibration rejection ratios were determined to be 10.9, 12.3 and 9.3, respectively. Overall, the vibration rejection ratio for an ME gradiometer working under H-field modulation was around 12, which represents the mean value for all assessed vibration rejection ratios. The rigid plastic board for the serial configuration of sensors was notably longer than the one used for the parallel one (see Fig. 3.6). Thus, the serial mode also experienced bending vibrations under a 5 Hz mechanical drive, which explains why even when larger amplitude vibrations were applied to the serial configuration, lower vibration rejection ratios were measured.

A two-part experiment (E2) was conducted to compare the vibration rejection ratios of two identical ME sensors working under H-field modulation (Part 1) and in passive mode (Part 2). To confirm that the ME sensors were working under the same vibration strength during both measurements, a fluxgate magnetometer was used as a reference to determine EMFD. The ME sensor working under modulation and the fluxgate magnetometer were located in a parallel configuration using the same experimental setup shown in Fig. 3.6. The value of EMFD determined by the fluxgate magnetometer was 19.6 nT, while the output from the ME sensor was 65.4 mV. Using the transfer function ($2.5\times10^6$ V/T) of the ME sensor working under H-field

modulation, the value of EMFD for the ME gradiometer operating under modulation was determined to be 26nT. In order to ensure that the applied vibration in Part 2 of the experiment was the same as in Part 1, the output from the fluxgate magnetometer was adjusted manually to match that from Part 1. For Part 2, the EMFD measured by the fluxgate magnetometer was found to be 19.5nT, which was close to that for Part 1. The output of 196 mV from the ME sensor in the E2 measurement was divided by the transfer function (2.5×106 V/T) of the sensor working under a passive mode, and the EMFD of the passive mode was then calculated to be 78nT. All the data measured in E1 and E2 are listed in Table 3.1.

Based on the obtained data shown above, the value of EMFD measured by the ME sensor working under H-field modulation was 30% larger than that measured by the fluxgate magnetometer. Considering that the vibration rejection of the fluxgate magnetometer is typically quite high,[68] our results confirm that the vibration rejection of the ME sensor working under H-field modulation was also quite high. Even though fluxgate magnetometers are poor at detecting vibration noises,[68] there nonetheless remains small noise outputs due to environmental magnetic induction (EMI). The outputs from the ME sensors working under both modulation techniques and in passive mode had contributions from EMI and vibrations generated by the shaker. The EMFD value measured for the ME sensor working in a passive mode was three times higher than that measured by an identical ME sensor working under modulation techniques. Clearly, we were able to confirm that the vibration rejection of ME sensors working under modulation techniques was considerably higher compared to analogous findings in passive mode. Since the intrinsic noise floor of ME sensors represents a bottleneck for enhancing the performance of an ME gradiometer, efforts going forward need to focus on noise reduction by improving both the excitation coils and the ME composites.

Table 3.1: The data measured in E1 and E2.

| E1 | Parallel mode | EMFD (nT) | 15 | 10 | 7.8 | E2 | | EMFD (nT) | |
|---|---|---|---|---|---|---|---|---|---|
| | | VRR | 17.4 | 13.4 | 10.7 | | Fluxgate | 19.6 | 19.5 |
| | Line mode | EMFD (nT) | 25 | 19 | 15 | | Active mode ME sensor | 26 | N/A |
| | | VRR | 10.9 | 12.3 | 9.3 | | Passive mode ME sensor | N/A | 78 |

## 3.5. New ME structure for vibration rejection.

As confirmed by the measurements listed above, when vibrations were transmitted the gradiometer could only reject the common mode part. Due to the asymmetric structure of the system, the vibration of non-common-mode part would impact the measurement of gradiometer curves. In order to obtain gradiometer curve measurements under vibrational conditions, I designed a new ME structure (Fig. 3.9) for achieving self-vibration cancellation. Specifically, for the PZT layer, the structure will only detect vibrational noise, while the ME sensor can detect both vibrational and magnetic signals. By incorporating an adaptive filter, which can automatically match the amplitude and phase of two outputs at a specific frequency, the vibrational noise can be subtracted. For this experiment, the magnetic source was 5Hz, and the vibration source was 12Hz. Figure 3.10 provides voltage output results, where the black curve is the voltage output from the ME sensor, the red curve is the voltage output from the PZT layer, and the blue curve is the subtracted result between them using the digital circuit of the adaptive filter. As evidenced by the blue curve at 12Hz, the voltage output caused by the vibration was rejected to 10 times lower than the original value (black curve at 12Hz).

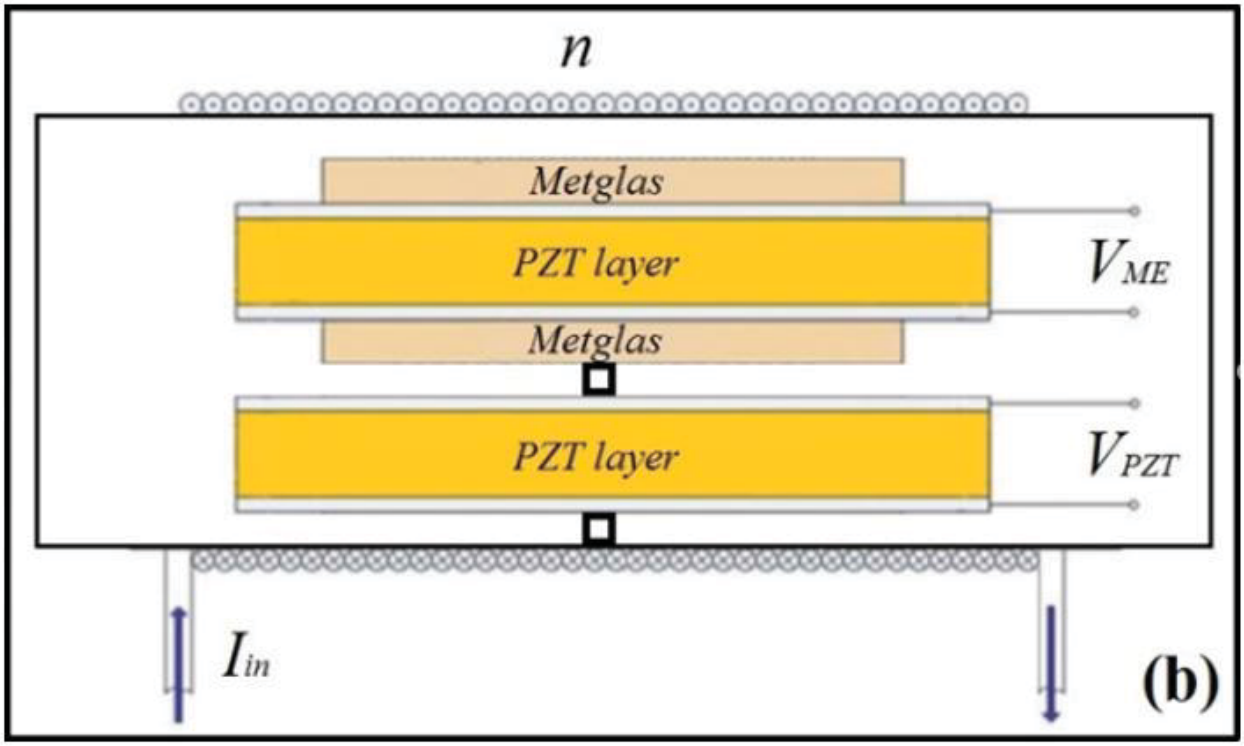


*Figure 3.9. Cross-section sketch of the new ME structure for self-vibration cancellation.*

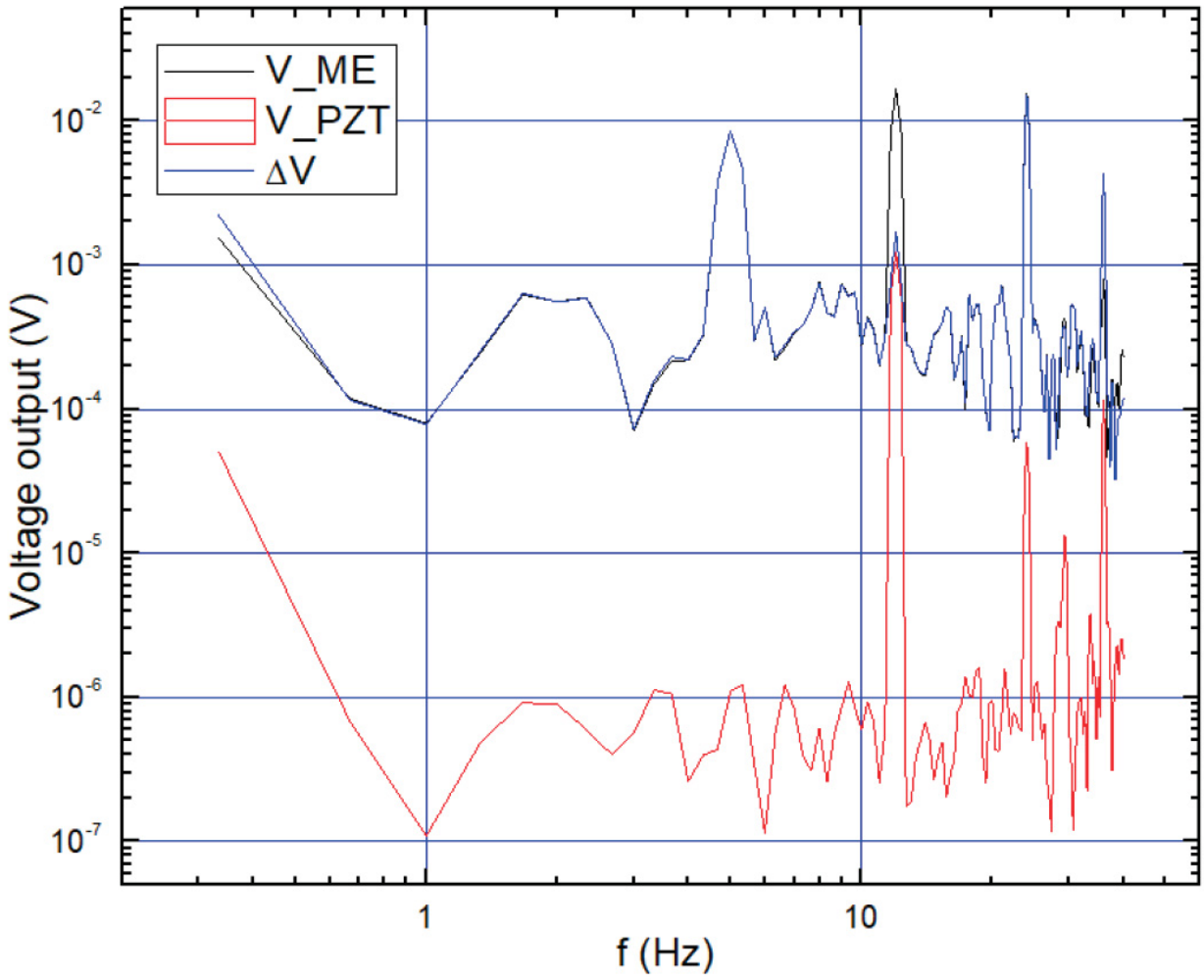


*Figure 3.10. Voltage outputs from an ME sensor (black curve) and PZT layer (red curve), and the subtracted results (blue curve) by using an adaptive filter.*

Subsequently, I constructed a gradiometer with the new ME structure. As shown in Fig. 3.11, the new ME gradiometer is located on the vibration system in two different configurations. In Configuration 1, the longitudinal direction of the ME gradiometer is perpendicular to the rigid metal bar, while in Configuration 2, the longitudinal direction of the ME gradiometer is along the rigid metal bar. In both cases, I used same magnetic sources and vibrations.

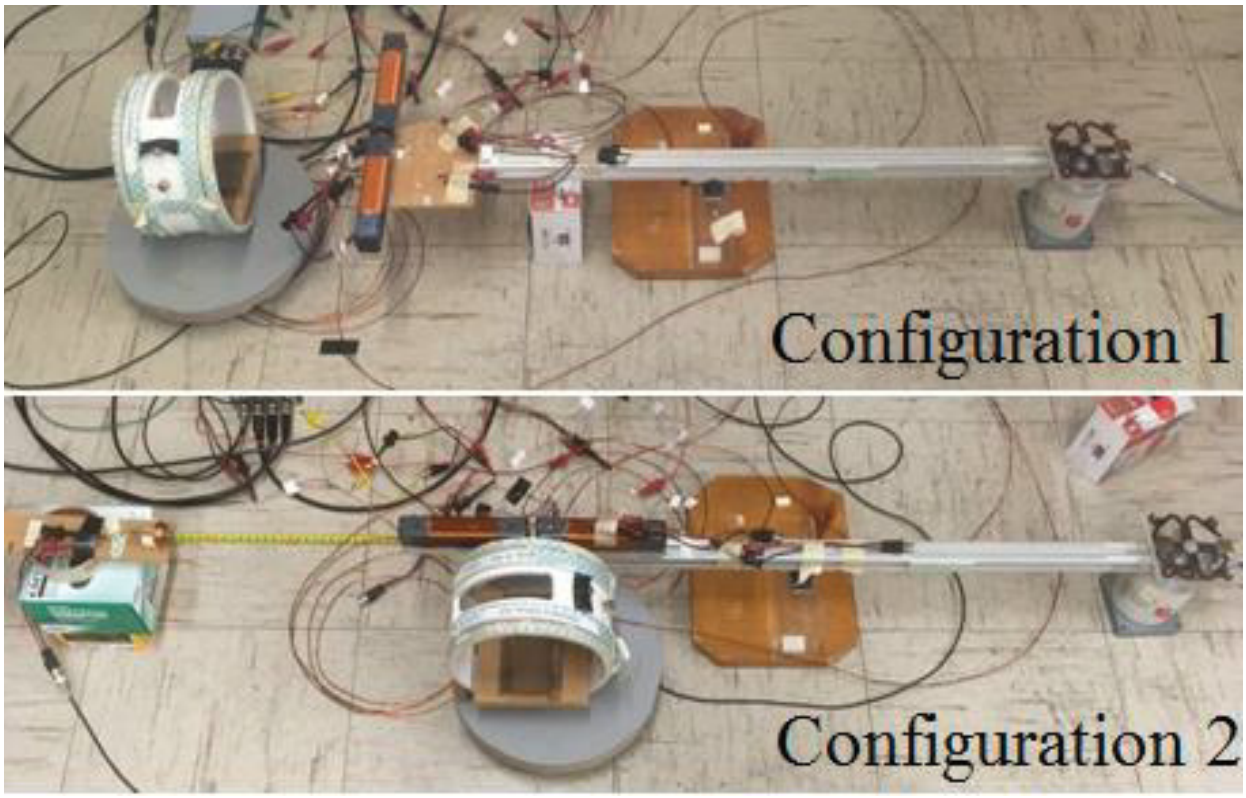


*Figure 3.11. Experimental setup for ME gradiometer with new ME structure operating in two different configurations.*

Figure 3.12 illustrates the results for the two configurations. Note that in both figures, the black curves were measured using a digital subtractor under a magnetic source, the red curves were measured using a digital subtractor under both a magnetic and vibrational source, and the blue curves were measured using an adaptive filter under both a magnetic and vibrational source. Although an adaptive filter is able to reject a significant proportion of vibrational noise, it cannot not reject it completely due to residual effects. Therefore, the most precise curves would be measured under non-vibrational conditions. Referring to Fig. 3.12, the blue curves were measured using an adaptive filter, which was able to reject most of the vibrational noise; accordingly, the blue curves can be seen to be quite close to the black ones. In contrast, the red curves were

measured under vibrational conditions without the use of an adaptive filter, which accounts for the fact that the red curves were less accurate compared to the other two.

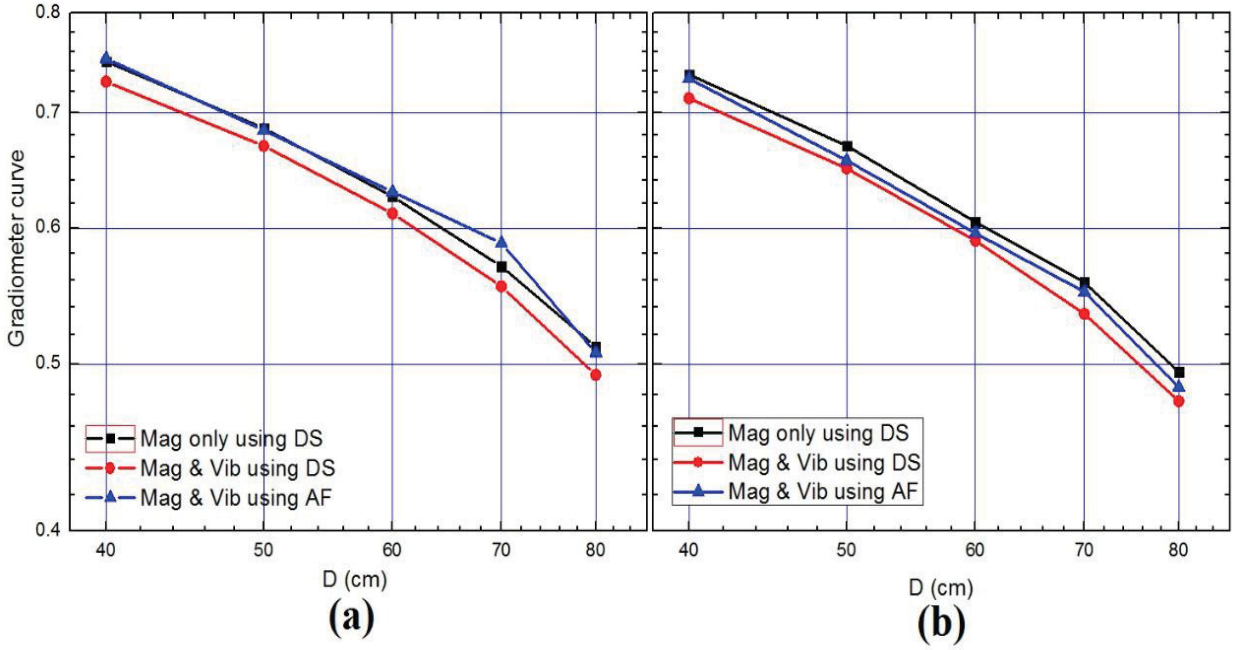


*Figure 3.12. Gradiometer curve measured under vibrations with the new ME structure.*

## 3.6. Spatial magnetic source detection with 2D and 3D configurations.

Prior work in our research group has shown that an ME gradiometer working under H-field modulation is capable of measuring the distance between the magnetic source and an ME sensor.[69] For this phase of the investigation, we focused on two-dimensional (2D) measurements of the detected magnetic field as a function of varying angles, in order to confirm whether the orientation of the magnetic source could be determined based on the position of the ME gradiometer. The detected magnetic source has also been characterized using a vector matrix, both mathematically and graphically.

**Experimental Procedure and Analysis**

**i. ME sensor structure and operational principles**

We developed an ME gradiometer consisting of several ME sensors with asymmetric and symmetric configurations. Each ME sensor consisted of five PZT fibers (40 mm × 2 mm × 0.2 mm), two symmetric Kapton patterns with interdigitated (ID) electrodes, and six Metglas foils (80 mm × 10 mm × 0.022 mm). As shown Figure 3.13, the five PZT fibers were fixed between the ID electrodes by an epoxy resin (Stycast 1264, USA), achieving a longitudinal-longitudinal (LL) polarization with a multi-push-pull configuration. Then, three Metglas foils were stacked and bonded together, and subsequently bonded on the top and bottom of the ID electrodes/PZT laminate, yielding ME sensors (Metglas/PZT/Metglas trilayer). The bonding agent used was an epoxy resin (West System 206, USA). An applied magnetic field induced a magnetization change in the Metglas layers, resulting a shape change via magnetostriction. This shape change was then transmitted to the PZT fibers due to mechanical coupling between the PZT fibers and Metglas layers, resulting in a voltage/charge output from the PZT fibers. The equivalent magnetic noise of the ME sensors was recorded to be approximately 60 pT/√Hz at 5Hz under H-field modulation.

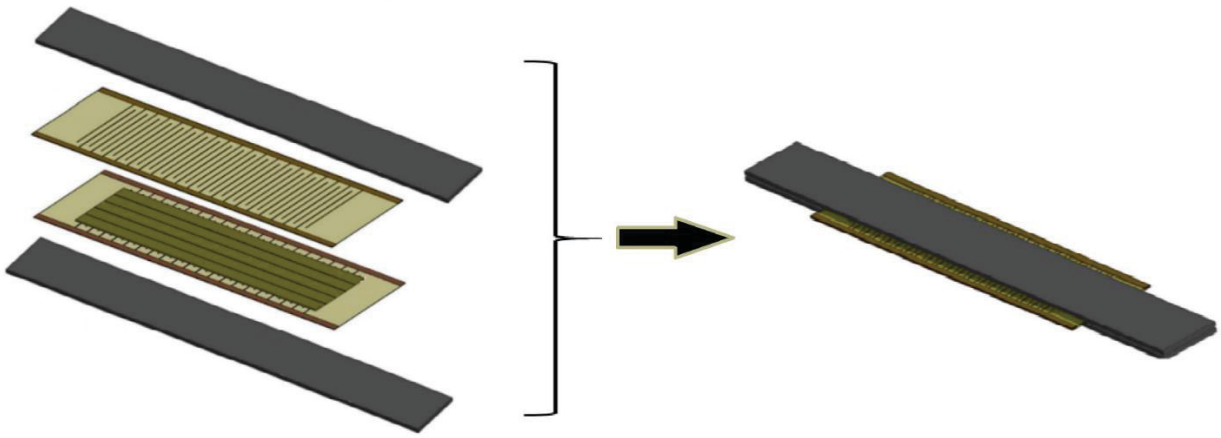

*Figure 3.13. Schematic of the ME sensor. Xu, Junran, et al. "Spatial magnetic source detection based on active mode magnetoelectric gradiometer with 2D and 3D configurations." Journal of Physics D: Applied Physics (2020), with fair use.*

**ii. Angular measurement for magnetic source detection in 2D**

First, we conducted angular measurements to determine the angle between the ME gradiometer and magnetic source. As documented in prior investigations, it is possible to determine the distance between the magnetic source and an ME gradiometer consisting only of two ME sensors in a 2D plane.[59,69] In contrast, it is not possible to use this pair of ME sensors to determine the angle between the magnetic source and the gradiometer. For example, if one uses ME sensors #1 and #2 (see Fig. 3.14(a)) to measure the magnetic sources at 90° and 270°, the outputs from the two sensors will be the same at these settings. Thus, at a minimum, an additional third ME sensor is needed in this measurement approach.

Accordingly, the proposed ME gradiometer consisted of three ME sensors with three different configurations, as shown in Figs. 3.14(a), 2(c), 2(e). All three ME sensors were in the same 2D plane. The ME gradiometer was positioned in the center of a circle working under H-field modulation, and the circle center overlapped in the middle point of the baselines between ME

sensors #1 and #2, between ME sensors #1 and #3, and between ME sensors #2 and #3. Note that the baseline is the center-to-center distance between two ME sensors. The baselines between ME sensors #1 and #2 and between sensors #2 and #3 were set at 15 cm. For the magnetic source, we utilized a ~1000 turns small search coil with a length of 9.5 mm and a diameter of 25.5 mm. We then measured the voltage outputs from the three ME sensors by orienting the axis of the search coil towards the center of a sweeping circle. The ME gradiometer and the search coil were placed in the same 2D plane. The radius of the circle was 0.5 m, and the search coil was supplied by a power amplifier (LDS PA25E Power Amplifier, Brüel & Kjær, Denmark) with a magnetic flux density of 210 nT. The ME gradiometer was operated under H-field modulation in all cases. Furthermore, all the voltage outputs from the ME sensors were calibrated using LabView to ensure that each ME sensor had the same voltage output under the same applied magnetic field. The data were captured using a spectrum analyzer (SRS SR785, Stanford Research Systems, Sunnyvale, CA, USA).

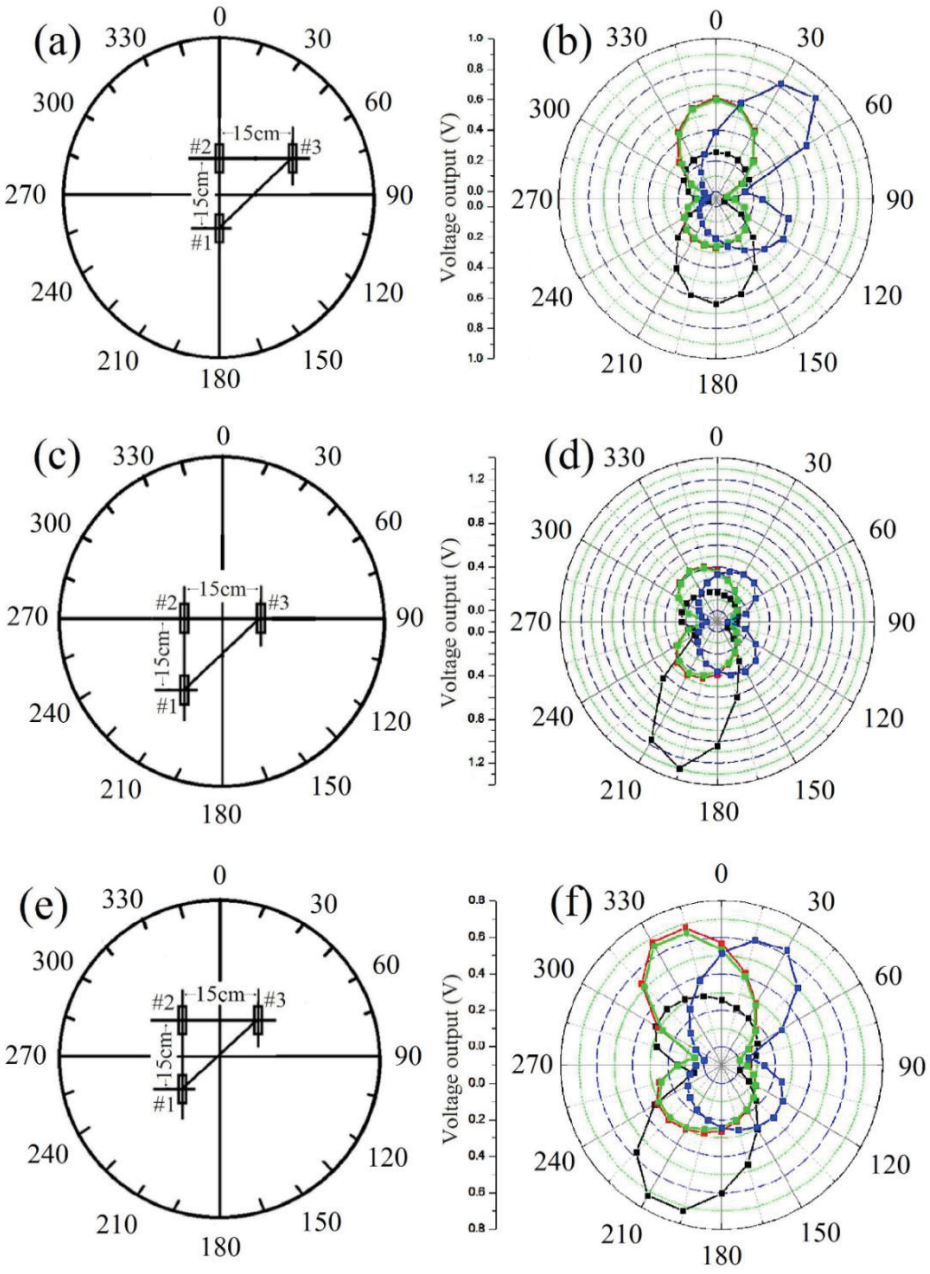


*Figure 3.14. Experimental setup and voltage output patterns from our ME gradiometer with different sensor configurations. (a), (c), and (e) show different configurations where the circle center is on the middle point of the different baselines. (b), (d) and (f) show the voltage output patterns from the ME gradiometer using the different sensor configurations. Xu, Junran, et al. "Spatial magnetic source detection based on active mode magnetoelectric gradiometer with 2D and 3D configurations." Journal of Physics D: Applied Physics (2020), with fair use.*

In order to verify that the magnetic field generated by the search coil was constant, each measurement was divided into two parts. In the first part, only sensors #1 and #2 were operated, while sensor #3 was not powered. In the second part, only sensors #2 and #3 were operated. Thus, the voltage output from sensor #2 was measured twice, which should have produced the same value each time. The voltage outputs from the ME gradiometer with different configurations (see Figs. 3.14(a), (c), and (e)) are shown in Figures 3.14(b), (d), and (f), respectively. In these plots, the black and blue patterns represent the voltage outputs from sensors #1 and #3, respectively, and the red and green patterns are the voltage outputs from sensor #2 (measured twice). Note that the red and green patterns overlap in each individual figure, verifying that the magnetic source was constant during measurement. The two pairs of ME sensors had a center circular distribution: #1 and #2 in Fig. 3.14 (a), and #2 and #3 in Fig. 3.14 (c). Accordingly, their corresponding patterns displayed circular center symmetry. For example, in Fig 3.14 (a), if the black pattern was rotated 180°, it overlapped with the green one. This result verifies the geometric relation between sensors #1 and #2. Under this condition, we could not determine when the search coil was located at either 90° or 270° on the circle; however, the blue pattern measurement using sensor #3 resolved this dilemma. In this case, the voltage outputs in the blue pattern at 90° or 270° were different. In the last configuration shown in Fig. 3.14 (e), sensors #1 and #2 had a line symmetry based on the horizontal line that crossed the 90° and 270° spots, and sensors #2 and #3 had a line symmetry based on the vertical line crossing the 0° and 180° spots. Therefore, their corresponding patterns should be symmetrically equal, as shown in in Fig. 3.14 (f). In other words, if the black pattern is turned over on the horizontal line that crosses the 90° and 270° spots, and the blue pattern is turned over the vertical line crossing the 0° and 180° spots, then all the patterns should overlap due to geometric symmetry. And indeed, as indicated in Fig. 3.15, all the different patterns can be seen

to nearly overlap after these operations were performed. Thus, these voltage output results confirmed that the magnetic source and sensitivity of our ME sensors were constant and stable. However, as shown in Figure 3.14 (f), the voltage outputs from the three ME sensors were not the same at all measured angles, which could then assist in determining the position of the magnetic source within the 2D plane.

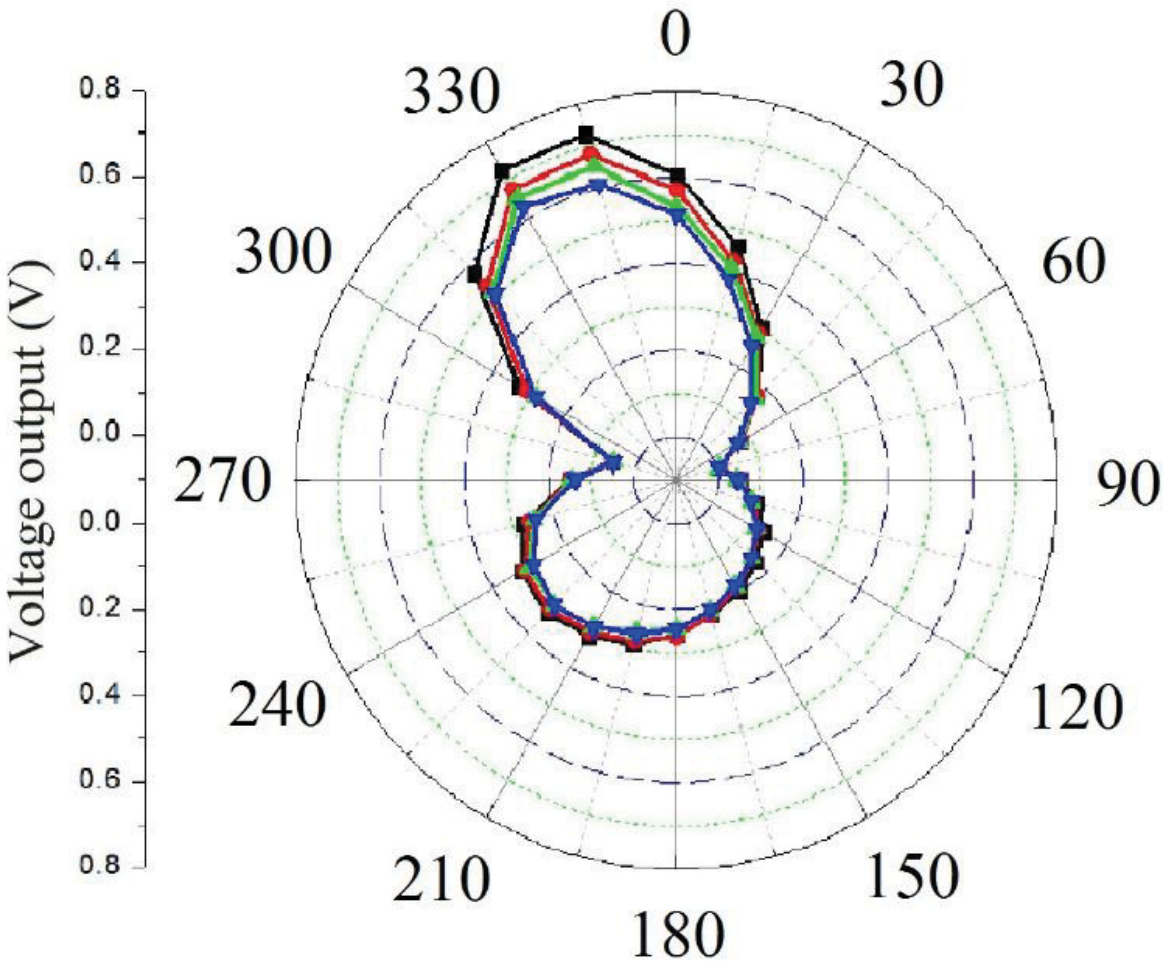


*Figure 3.15. Pattern comparison after operation based on the symmetry. Xu, Junran, et al. "Spatial magnetic source detection based on active mode magnetoelectric gradiometer with 2D and 3D configurations." Journal of Physics D: Applied Physics (2020), with fair use.*

**iii. Gradient measurement of magnetic source in 3D**

To detect the location of an unknown magnetic source in 3D, it is necessary to measure its gradient distribution. The gradient of a magnetic source has previously been measured by an ME gradiometer consisting of two ME sensors,[69] defined as:

$$\vec{G} = \frac{\overrightarrow{B_1} - \overrightarrow{B_2}}{\overrightarrow{B_1}} ; \tag{3.14}$$

where $\overrightarrow{B_1}$ and $\overrightarrow{B_2}$ are the magnetic flux densities measured by the two ME sensors. The sensitivities of the ME sensors were calibrated in order to ensure their similarity. Equation (3.14) can then be rewritten as:

$$\vec{G} = \frac{\overrightarrow{V_1} - \overrightarrow{V_2}}{\overrightarrow{V_1}} , \tag{3.15}$$

where $\overrightarrow{V_1}$ and $\overrightarrow{V_2}$ are the voltage outputs of the two ME sensors. If one uses a 3D Cartesian coordinate system to measure the magnetic gradient along x axis, y axis, and z axis, then the gradient of magnetic source can be expressed by the matrix

$$\overrightarrow{G_{XYZ}} = \begin{bmatrix} \overrightarrow{G_X} \\ \overrightarrow{G_Y} \\ \overrightarrow{G_Z} \end{bmatrix} = \begin{bmatrix} \overrightarrow{G_{xx}} & \overrightarrow{G_{xy}} & \overrightarrow{G_{xz}} \\ \overrightarrow{G_{yx}} & \overrightarrow{G_{yy}} & \overrightarrow{G_{yz}} \\ \overrightarrow{G_{zx}} & \overrightarrow{G_{zy}} & \overrightarrow{G_{zz}} \end{bmatrix} ; \tag{3.16}$$

where $\overrightarrow{G_X}$, $\overrightarrow{G_Y}$, and $\overrightarrow{G_Z}$ are the magnetic gradients measured along the x, y, and z axes, respectively. The matrix on the right gives the magnetic gradient components along these three axes, where the first subscript is the orientation of the ME gradiometer and the second is the direction of the magnetic gradient component measured.

The 3D magnetic gradient measurement is illustrated in Fig. 3.16. The magnetic source was positioned in the center of a cubic-shaped space, which was also the zero point of the 3D coordinate. This magnetic source served as the search coil that was used to obtain angular measurements. The longitudinal direction of this search coil was along the x axis. The eight corners of the cubic space

were selected as the measuring points, where the various ME sensors of the gradiometer were then placed. The mid-point of the baseline of the ME gradiometer overlapped with the measurement points. The baseline was fixed at 15 cm in all cases. The shortest distance between the cube's center to the six cubic surfaces was 30 cm.

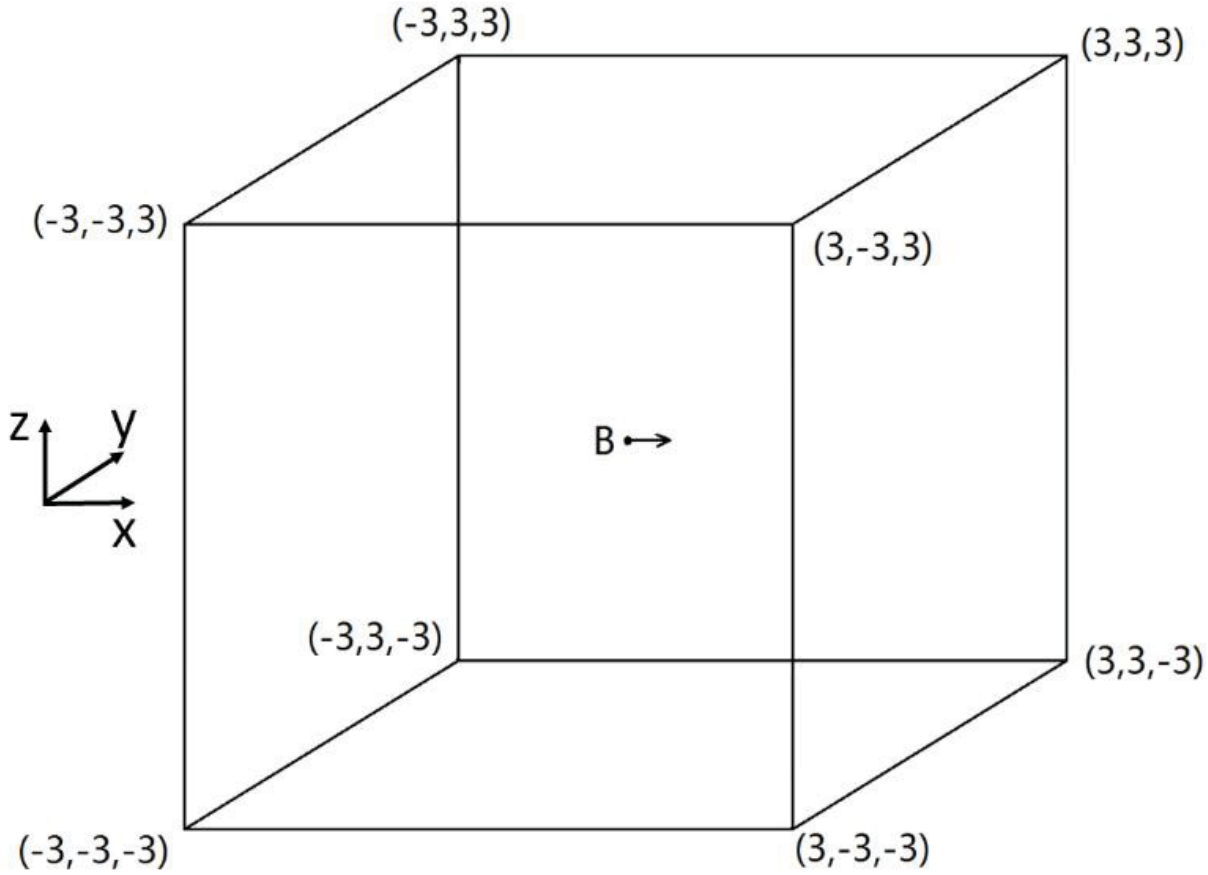


*Figure 3.16. Experimental outlay for the 3D magnetic gradient measurement. Xu, Junran, et al. "Spatial magnetic source detection based on active mode magnetoelectric gradiometer with 2D and 3D configurations." Journal of Physics D: Applied Physics (2020), with fair use.*

Figure 3.17 illustrates the 3D magnetic gradient measurement setup at the measuring point of (3,3,3). It also shows all nine different magnetic gradient components given in the matrix

equation (3.16). In all nine cases, the distance between the search coil and the mid-point of the ME gradiometer baseline was equal to the distance between the magnetic source and the eight corners of the cube in Fig. 3.13. The baseline was fixed at 15 cm in each case. The search coil was powered by an amplifier (LDS PA25E Power Amplifier, Brüel & Kjær, Denmark). The voltage outputs from the ME gradiometer were calibrated by LabView programs, using data obtained by a spectrum analyzer (SRS SR785, Stanford Research Systems, Sunnyvale, CA, USA).

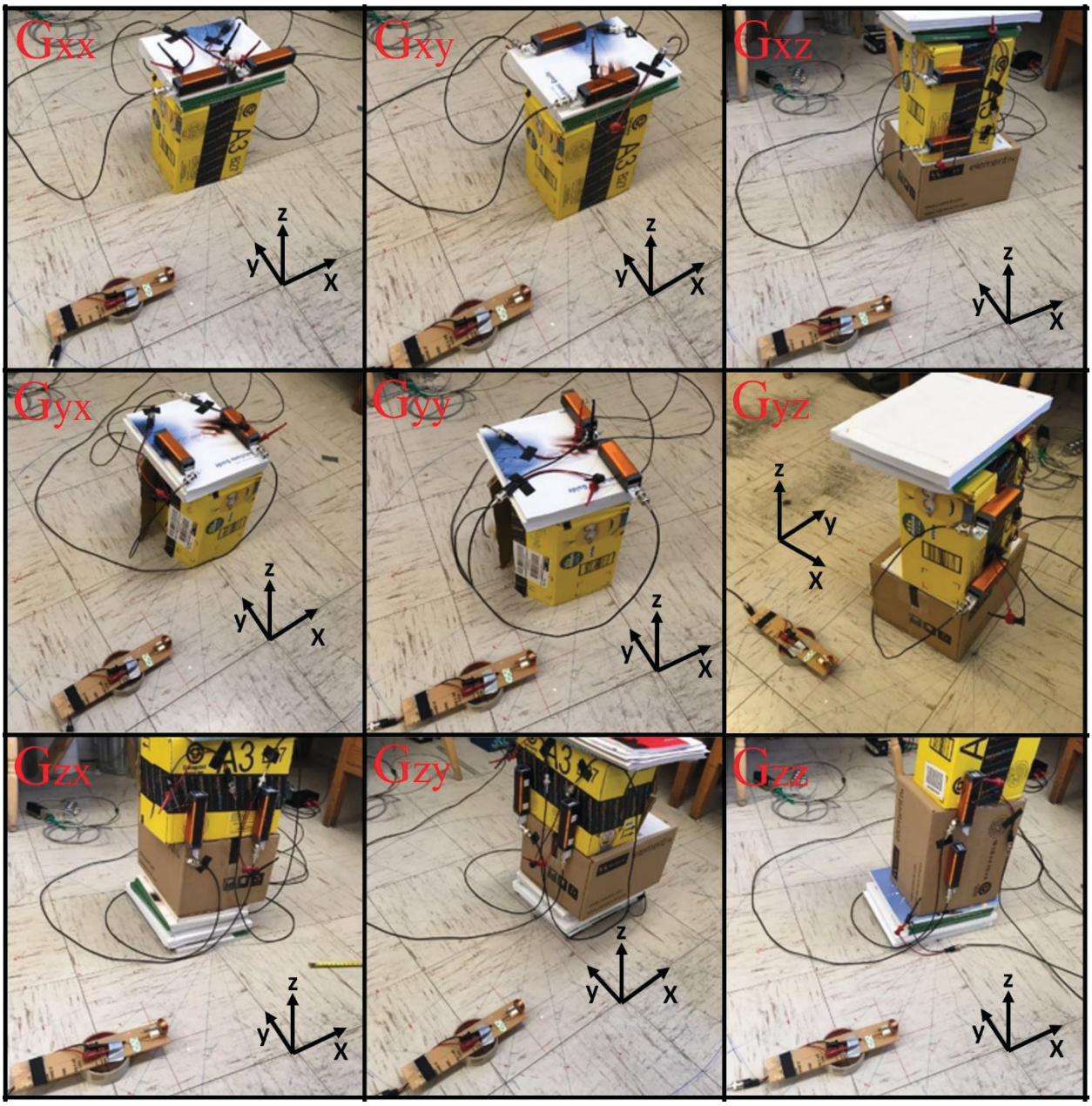


*Figure 3.17. Experimental setup for the 3D magnetic gradient measurement at the measurement point of (3,3,3). Xu, Junran, et al. "Spatial magnetic source detection based on active mode magnetoelectric gradiometer with 2D and 3D configurations." Journal of Physics D: Applied Physics (2020), with fair use.*

By implementing Equations (3.15) and (3.16), we were able to obtain the components of the magnetic gradient matrix at the point (3,3,3). The absolute value of the magnetic gradient components can be determined as:

$$\left|\overrightarrow{G_{(3,3,3)}}\right| = \begin{bmatrix} 0.1085 & 0.7299 & 0.7975 \\ 0.6468 & 0.3180 & 0.5980 \\ 0.3370 & 0.5901 & -0.4156 \end{bmatrix}. \tag{3.17}$$

Following the vector rule, we can obtain:

$$\begin{cases} \left|\overrightarrow{G_X}\right| = \sqrt{\left|\overrightarrow{G_{xx}}\right|^2 + \left|\overrightarrow{G_{xy}}\right|^2 + \left|\overrightarrow{G_{xz}}\right|^2} \\ \left|\overrightarrow{G_Y}\right| = \sqrt{\left|\overrightarrow{G_{yx}}\right|^2 + \left|\overrightarrow{G_{yy}}\right|^2 + \left|\overrightarrow{G_{yz}}\right|^2} \\ \left|\overrightarrow{G_Z}\right| = \sqrt{\left|\overrightarrow{G_{zx}}\right|^2 + \left|\overrightarrow{G_{zy}}\right|^2 + \left|\overrightarrow{G_{zz}}\right|^2} \end{cases}. \tag{3.18}$$

Equation (3.17) can also be expressed as:

$$\left|\overrightarrow{G_{(3,3,3)}}\right| = \begin{bmatrix} 1.0865 \\ 0.9365 \\ 0.7966 \end{bmatrix}. \tag{3.19}$$

Equations (3.17) and (3.19) are the expressions of $\left|\overrightarrow{G_{(3,3,3)}}\right|$ in terms of the magnetic gradient components and the total magnetic gradient. Repeating the measurement eight times, we were able to identify the magnetic gradients at the eight measurement points. Figure 3.18 shows the magnetic gradient components and the total magnetic gradients measured using the 3D ME gradiometer. For example, at measuring point (3,3,3), the red, blue, and green arrows represent the nine gradient components in Equation (3.17). The projected distance of the red arrow was 0.1085, 0.7299, and 0.7975 were along the x, y, and z axes, respectively. Similarly, the projected distances of the blue arrow were 0.6468, 0.3180, and 0.5980 along the x, y, and z axes, respectively. The black arrow represents the total magnetic gradient at measurement point (3,3,3), which was obtained via Equation (3.18). The projected distances of the black arrow were 1.0865, 0.9365, and 0.7966 along the x, y, and z axes, respectively. These values indicate the total gradient changes at (3,3,3) using

a baseline of 15 cm. Theoretically, the results for the black arrows in Fig. 3.18 should all be symmetrically equal. Experimentally, we observed that the direction of each black arrow should be orientated outward, and essentially symmetrical to each other. The average error for the black arrow lengths between the adjacent measuring points was 9.86%, which is probably due to the geometric asymmetry in the locations of the ME gradiometer (see Fig. 3.17); in addition, the search coil we utilized cannot be considered as a perfect magnetic point source. The black arrows represent the flux directions of the magnetic source, which were precisely the direction along which magnetic gradient changes were observed in our experiments. These results verify the magnetic field distribution in 3D space of the source, and demonstrate the feasibility of the magnetic source detection using ME gradiometers.

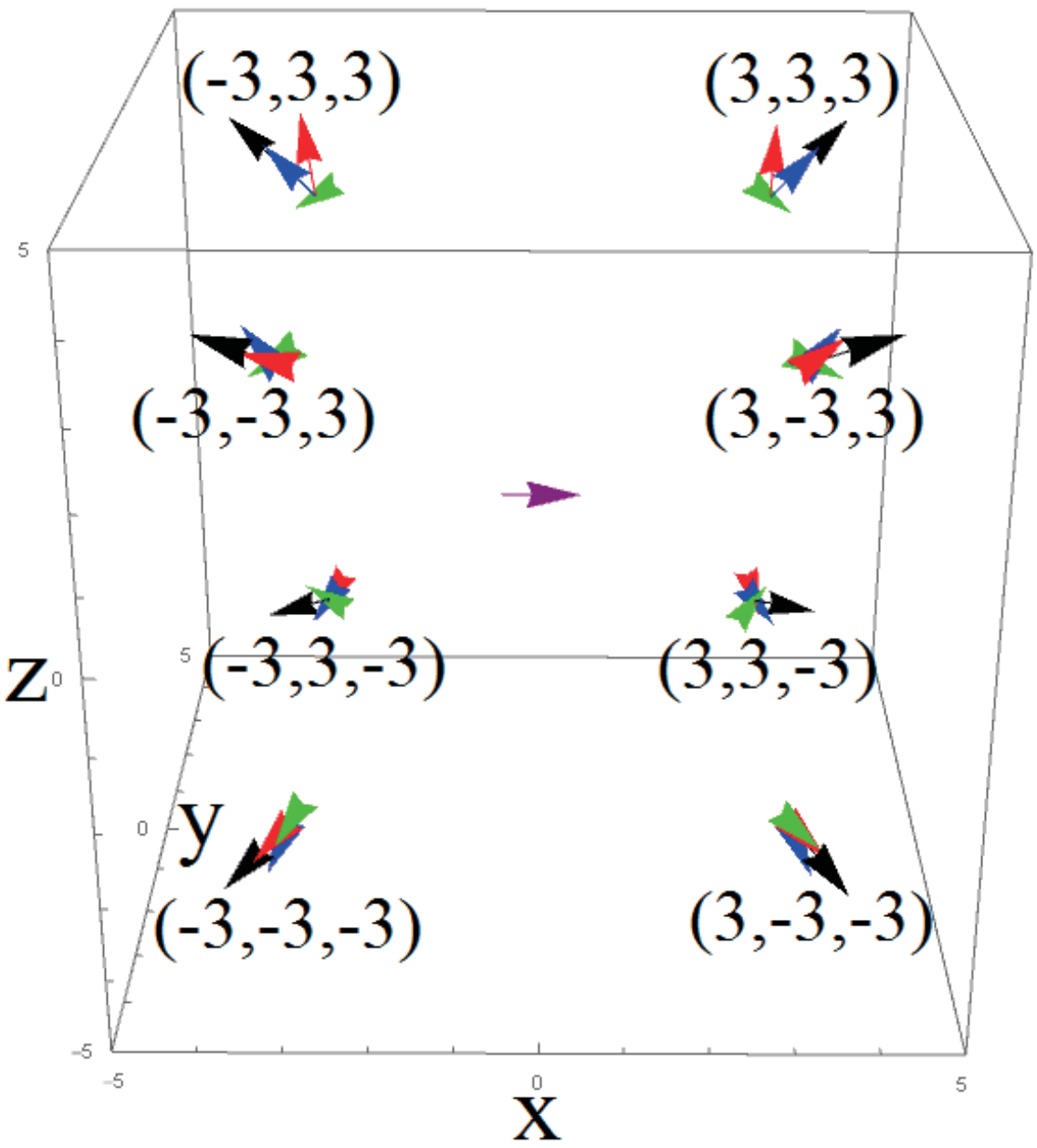


*Figure 3.18. Magnetic gradient components and total magnetic gradients measured using our ME gradiometer in 3D space, using the experimental setup shown above in Figure 3.16. Xu, Junran, et al. "Spatial magnetic source detection based on active mode magnetoelectric gradiometer with 2D and 3D configurations." Journal of Physics D: Applied Physics (2020), with fair use.*

## 3.7. Summary of this section

In this paper, ME gradiometers whose individual sensors operated under H-field modulation were constructed for the first time and subsequently characterized. The ME gradiometer response curve was measured for this ME active gradiometer, and shown to be capable of detecting a source out to a distance normalized to the baseline of D/d = 13. We also determined the vibration rejection ratio; specifically, we found that the vibration rejection of an ME gradiometer working in the H-field modulation was at least 3x larger than that of a passive mode ME gradiometer, but yet only 30% smaller than a fluxgate gradiometer. Additionally, we confirmed that the our H-field modulation ME sensors demonstrated a significantly lower noise floor than a corresponding passive sensor.

As detailed in this section, we also showed that an ME gradiometer consisting of three ME sensors (Metglas/PZT/Metglas heterostructures) is able to determine the angle between the magnetic source and the ME gradiometer. Using three baselines, the unique pattern groups of the magnetic field distributions were identified, which could distinguish the location of an unknown magnetic source. Furthermore, an ME gradiometer consisting of two ME sensors was capable of detecting changes in the magnetic gradient of the source, where the eight measurement points are symmetric to each other. As a consequence, this development facilitated the determination of both the signal and distance, demonstrating its potential for localization of an unknown magnetic source in 3D space.

# CHAPTER 4: LOW-FREQUENCY ME LAMINATE TRANSMITTER

## 4.1. Introduction.

A VLF transmitter is located in Cutler, ME (USA) that is capable of transmitting 2 MW of power.[70] It operates near 25 kHz and can transmit a signal around the world using a very small bandwidth at low data rates. This transmitter facility utilizes large towers spread across 2000 acres and has a radiation efficiency of 75%.[70] Portable receivers for this VLF system are magnetic sensors that are widely available. Increasingly, however, more compact transmitters that are still capable of sending VLF electromagnetic waves are needed. Therefore, the reduction of the transmitter size needs to be investigated. The requirements of the VLF transmitter as identified by as: 1) transmission of dynamic time harmonic magnetic field in the fT range at km distance ranges, 2) packaged in a portable self-contained system that includes the emitting material, power, electronics and packaging materials, 3) consumes no more than 20W of power. Such a new transmitter would enable forward and backward communication of very low frequency signals in a portable and robust manner.

Our research team has previously developed ME heterostructures for passive (battery operated) magnetic sensors/receivers,[10,35,71-73] which utilized external magnetic fields to excite magnetostrictive layers into mechanical vibration. In turn, this mechanical vibration was transferred to the bonded piezoelectric layer, resulting in voltage output. Wang et al.[18] fabricated a longitudinal-longitudinal (LL) multi-push-pull structure using a piezoelectric layer bonded between two interdigitated electrodes (ID), and subsequently bonded to magnetostrictive layers forming a sandwich-like structure. A schematic of this ME sensor and its operating principle is depicted in Figure 4.1. Magnetic sensors based on these laminates and a charge-amplifier detection method have been shown to display an extremely low equivalent magnetic noise floor of 5.1

pT/√Hz at 1 Hz. A large ME voltage coefficient of 52 $Vcm^{-1}Oe^{-1}$ has been obtained under optimized direct current DC magnetic bias for Metglas/ PMN-PT trilayer laminates.[18,47]

Furthermore, large gains in the ME properties of ME laminates have been reported near the electromechanical resonance (EMR) frequency. The highest resonance ME voltage coefficient reported is 1100 $Vcm^{-1}Oe^{-1}$, based on the structure shown in Figure 4.1.[18,74,75] Later, even higher ME voltage coefficients have been achieved by optimizing their geometric configuration and improving the interfacial bonding between the piezoelectric and magnetostrictive phases. For example, Li et al. reported a spin-coat/vacuum-bag method that could improve interfacial bonding and increase ME coupling.[76] Furthermore, theoretical analysis has revealed that the resonance ME coupling coefficient in ME laminates can be significantly increased as a result of improvements in the mechanical quality factor $Q_m$.[37] Based on the discussions above, Chu et al. proposed a composite with (1-1) connectivity, which exhibited an enhanced resonance ME coupling coefficient of 7000 $Vcm^{-1}Oe^{-1}$.[77] Their study confirms that ME sensors can be designed to be highly effective at receiving low-frequency (~30 kHz) and low-power-propagating signals by utilizing this large ME gain effect at the EMR.

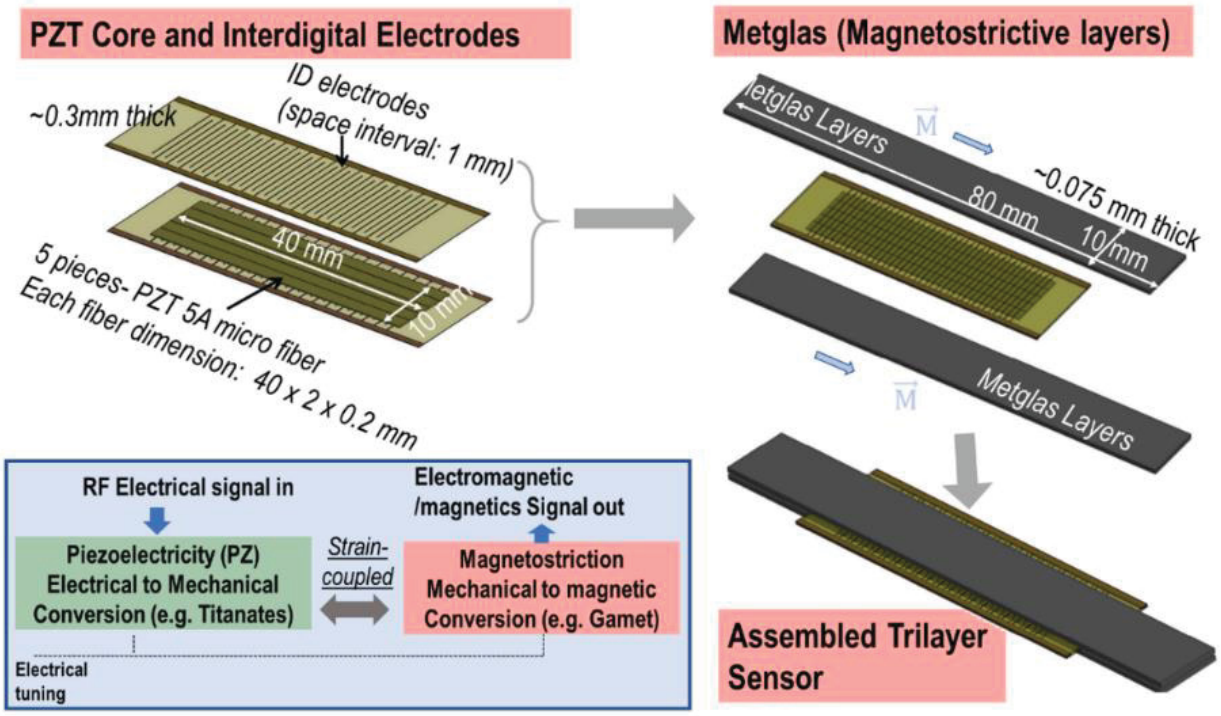


*Figure 4.1. Schematic of the proposed ME laminate transmitter, its construction and operation principal using piezo and magneto layers. Xu, Junran, et al. "A low frequency mechanical transmitter based on magnetoelectric heterostructures operated at their resonance frequency." Sensors 19.4 (2019): 853, with fair use.*

More recently, we examined the transduction capabilities of ME heterostructures for power conversion devices and motors.[78,79] A highly efficient, solid-state gyrator based on tri-layer composites, which consisted of two magnetostrictive ferrite layers epoxied to a PZT piezoelectric core placed between the ferrite layers, was developed.[80] This electrical element used an input electric field to generate an output magnetic flux.[79,81] In turn, this flux then induced current that flowed into an N-turns coil. Near the EMR, this ME gyrator exhibited both power conversion and transfer efficiency to a coil in the near field at about 90% under low power density (0.61 mW/cm$^3$), and 75% under a higher one of 1.83 W/cm$^3$.[81] These results signify that ME laminates do not have

significant radio frequency (RF) losses at very low frequencies (VLFs), and thus show potential for higher induction transmission efficiency in the near field. Accordingly, ME laminates represent promising candidates for incorporation in an ME based transmitter–receiver system when operating near the EMR. Such a resonance-based transmitter–receiver would also have a DC bias tunable frequency.

This section describes the magnetic flux transmitting capabilities of ME resonance laminates. The measurements of magnetic flux density detection are presented, and we compared the proposed ME laminate transmitter with a same-sized small current loop. Finally, the ME laminate structure was optimized to enhance its transmission potential.

## 4.2. Laminate construction and operating principle.

### (a) Design and operation

A multiferroic antenna structure consisting of piezoelectric and magnetostrictive materials has been proposed, which was used to create electromagnetic waves.[82] Based on this previous work, we investigated ME laminates functioning at their electromechanical resonance frequency. The composite laminates consisted of a piezoelectric (PZT-5A) core and magnetostrictive layers on both the top and bottom, as shown in Figure 4.2(a). The PZT core consisting of five PZT fibers was attached with interdigitated (ID) electrodes to provide electrical actuation. According to the piezo properties, the longitudinal vibrations in the piezoelectric layers are transferred to the magnetostrictive layers due to mechanical (or strain)-coupling between PZT core and the Metglas layers at EMR. The magnetostrictive layers (e.g., Metglas) have the inherent ability to convert mechanical vibrations to magnetic fluxes. Notably, these fluxes could be steady (static) magnetic fluxes, but upon radio frequency actuation, these fluxes are time-varying in nature and thus will

exhibit induction transmission in the near field. This described operating principle is also referred to as the electro-mechanical-magnetic effect.

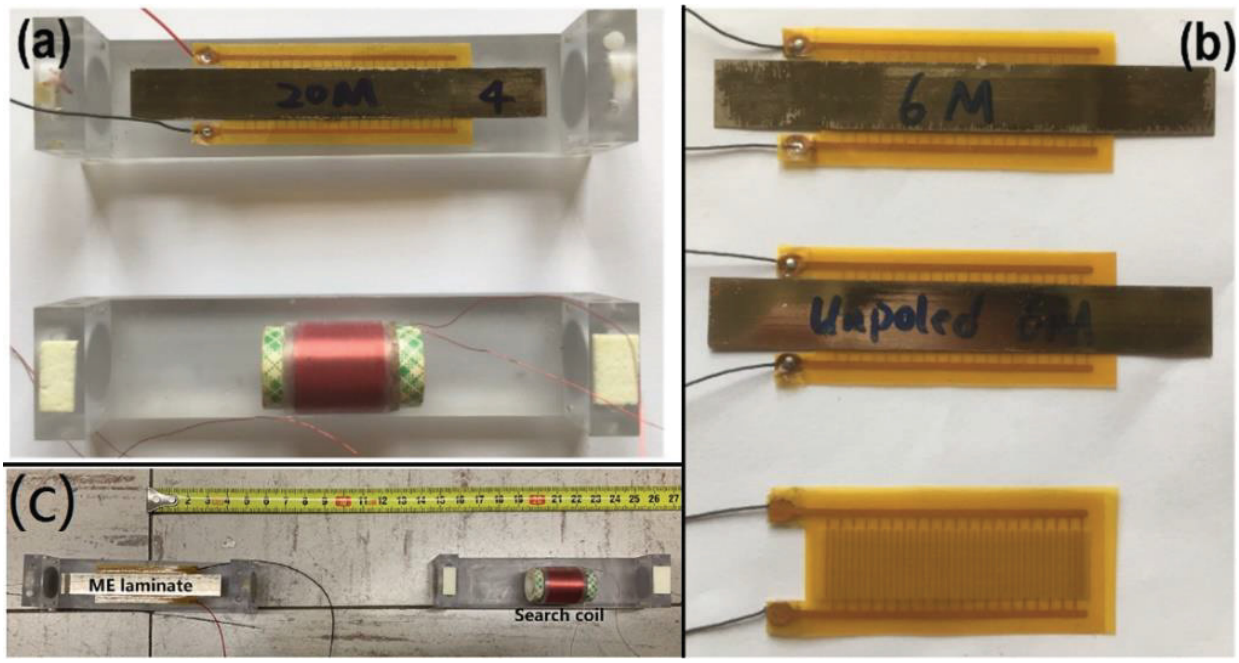


*Figure 4.2. (a) fabricated ME laminate and search coil used for test and measurements, (b) three samples- 6 Metglas layers (6M) based ME laminate, unpoled 6M ME laminate and poled Piezo layers used in characterization, and (c) experimental set-up for flux measurements. Xu, Junran, et al. "A low frequency mechanical transmitter based on magnetoelectric heterostructures operated at their resonance frequency." Sensors 19.4 (2019): 853, with fair use.*

**(b) Fabrication**

To demonstrate the basic operation of the ME laminates transmitter, three samples of varying construction elements were prototyped. The samples of the constructed laminates and PZT layer are shown in Figure 4.2(b). The first sample (of dimension 80 mm × 20 mm × 0.4 mm) was a Metglas/PZT/Metglas trilayer with six Metglas layers (three on either side). The PZT layer was

poled in this sample. To reiterate, poling refers to the process of orienting all material dipoles in one direction via the application of a strong electric field. Upon switching off the field, these dipoles do not return to their original position. Poling is essential for inducing the required piezoelectric effect in the PZT layer. The second sample (dimension: 80 mm × 20 mm × 0.4 mm) was also a geometrically similar trilayer with a total of six Metglas layers; in this case, however, the PZT layer was not poled. If the ME laminate with the unpoled PZT layers was driven under a set input power, then the electro-mechanical effect should be negligibly low. The third sample (dimension: 53 mm × 20 mm × 0.3 mm) was a poled PZT layer without any attached Metglas layers. If this sample was driven under a set input power, then there should only be electrical (non-magnetic) interference generated. Figure 4.2a (bottom) shows the copper coil with a diameter of 16 mm and length of 15.4 mm used as the receiver. There are approximately 200 turns of the coil.

## 4.3. Experimental setup, basic tests and optimization.

### (a) Verification of the electro-mechanical-magnetic effect.

First, we needed to confirm that the magnetic flux around the EMR detected by a receiver was, indeed, emitted by the ME laminate transmitter through the electro-mechanical-magnetic effect in the laminate. Specifically, since an unpoled PZT-based, ME-laminated layer—as well as an poled PZT layer lacking any Metglas layers—would be unable to generate magnetic flux, these were used as control samples. Therefore, an experiment was designed using the three different samples, as depicted in Figure 4.2c. To verify the electro-mechanical-magnetic effect, magnetic flux densities were measured by exciting the three samples with input signals at their resonance frequencies. A receiver search coil was placed at 40 cm along the longitudinal direction of the laminate transmitter (Figure 4.2c).

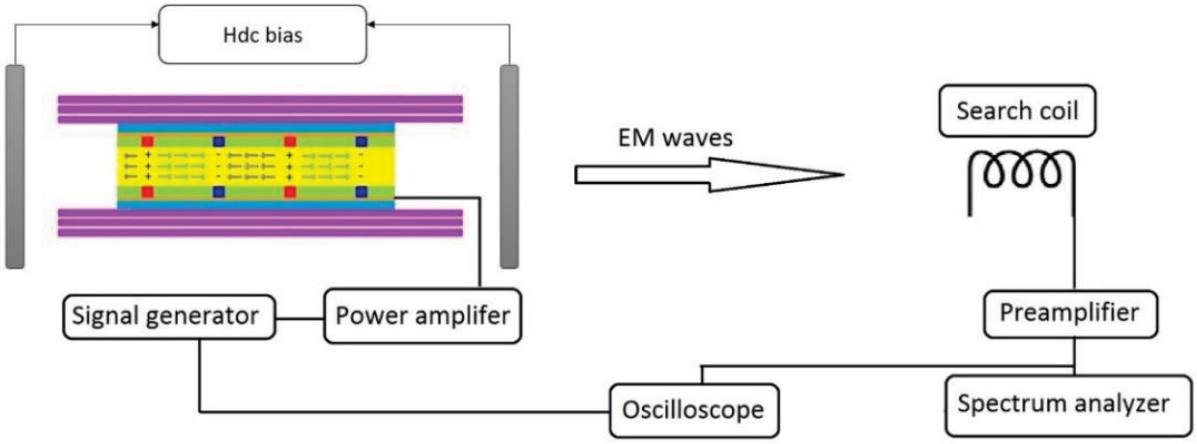


*Figure 4.3. Measurement set-up and excitation method used for the characterization of the ME laminate transmitter. Xu, Junran, et al. "A low frequency mechanical transmitter based on magnetoelectric heterostructures operated at their resonance frequency." Sensors 19.4 (2019): 853, with fair use.*

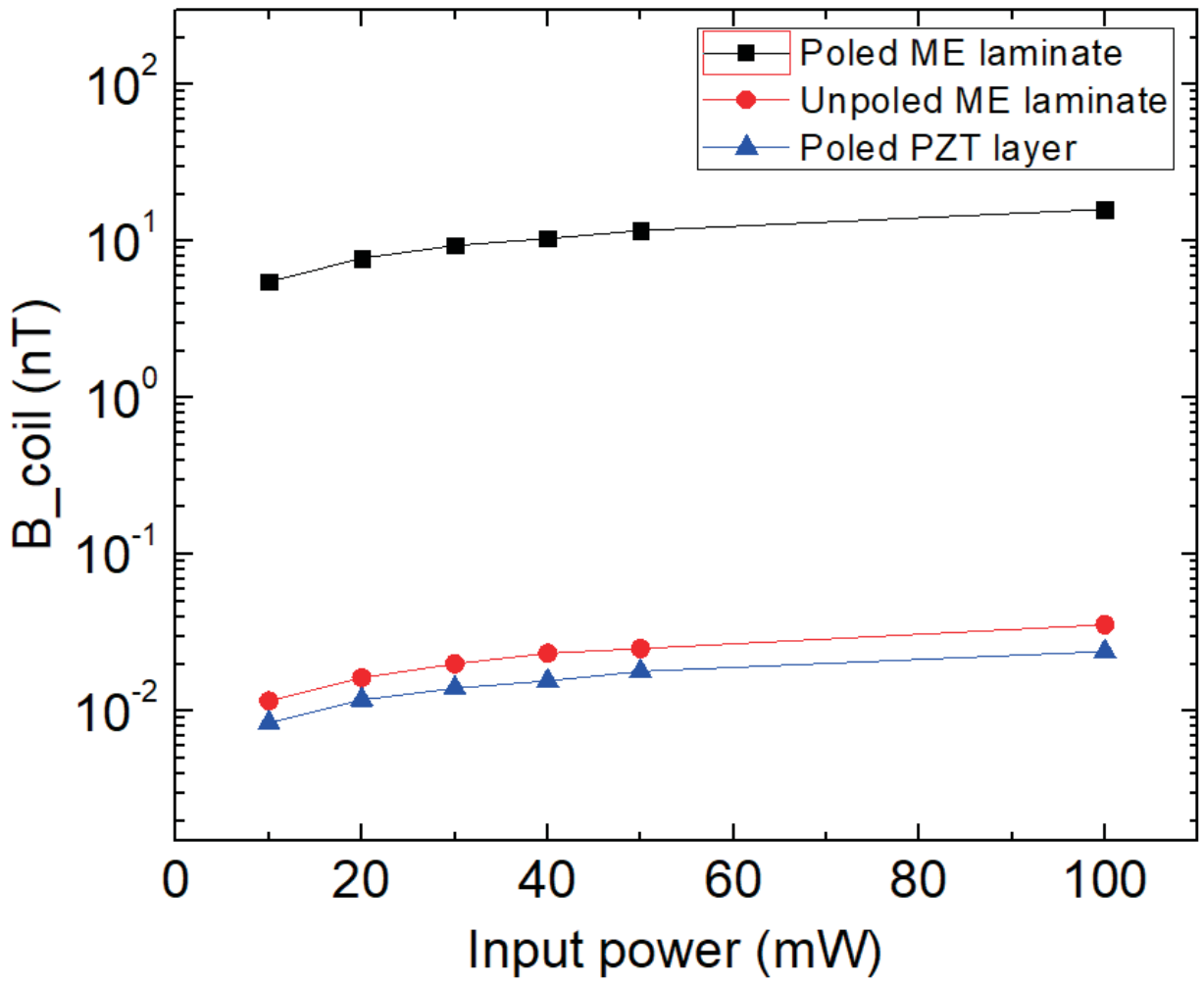


*Figure 4.4. The magnetic flux densities detected by the receiver as a function of the increasing input power to three different samples. Xu, Junran, et al. "A low frequency mechanical transmitter based on magnetoelectric heterostructures operated at their resonance frequency." Sensors 19.4 (2019): 853, with fair use.*

The three fabricated samples were replaced at the transmitter side one-by-one and the magnetic flux density was measured. The measurement and excitation of the samples were conducted using the set-up shown in Figure 4.3. The voltage output received from the search coil was divided by the transfer function of the coil to obtain the detected magnetic flux density. The voltage output of the search coil was obtained using a preamplifier (SRS SR560, Stanford Research Systems, Sunnyvale, CA, USA) and a spectrum analyzer (SRS SR785, Stanford Research Systems, Sunnyvale, CA, USA), which was also observed on an oscilloscope (MSOX3014T, KEYSIGHT, Santa Rosa, CA, USA). In each case, the applied input power was gradually varied from 10 mW to 100 mW, while a resonance frequency, (i.e., 28 kHz) was used for excitation. The input power was generated from a signal generator (AFG320, Tektronix, Inc., Beaverton, OR, USA), and amplified by an amplifier set at 100 amplification. Only Sample 1 (the poled PZT layer with Metglas layers) displayed an "electromagnetic" resonant frequency (around 28 kHz). Since Sample 2 (the unpoled PZT layer with Metglas layers) was unpoled, it did not display "electromagnetic" resonant frequency in the low-frequency regime. Although Sample 3 (the poled PZT layer without Metglas layers) did evidence an "electroelastic" resonant frequency (around 35 kHz), it did not result from the electromagnetic effect. Figure 4.4 shows the magnetic flux density detected by the receiver coil as a function of the input power for the three samples. The values measured using the trilayer with poled PZT were about three orders of magnitude higher than the ones from the poled PZT layer only. This finding confirmed our assumption that the receiver measured the signal from Sample 1 and not the electromagnetic interference (EMI) in the room. Furthermore, Sample 2 (with unpoled PZT layer) was not polarized—yet still exhibited very weak electro-mechanical coupling capable of generating a tiny magnetic flux by the magnetostrictive layers (Metglas). However, Sample 3 (poled PZT layer without Metglas layers) failed to generate

any magnetic flux in the absence of magnetostrictive layers, which accounts for why there was still a small difference between the red curve and blue curve in Figure 4.4. Thus, in this instance, the detected magnetic flux density from Sample 3 was simply the background EMI in the room. Clearly, the magnetic flux densities detected by the receiver were generated by the ME laminate transmitter with poled PZT layers.

This experimental measurement was then repeated at the EMR using the trilayer structure with a poled PZT core and rotating it to 45° and 90°. The distance between the ME laminate transmitter and the receiver was maintained at 40 cm. As opposed to a 16 nT flux observed with a 0° case, 9.6 nT and 0.82 nT flux values were observed for 45° and 90°, respectively. The almost two orders of magnitude decrease in the magnetic flux along the transverse direction (90° case) compares with the longitudinal direction (0° case). Thus, results from these experiments served to verify the ME laminate operation.

(b) Effect of Number of Metglas Layers.

Next, we determined that the magnetic flux density generated by the ME laminate transmitter could be enhanced by increasing the number of Metglas layers. Specifically, we constructed ME laminate transmitters with a varying number of bonded Metglas layers and then measured their ME coupling efficiency. The receiver was implemented using a standard Helmholtz coil with 50 turns on each side (radius: 45 mm). In this set-up, the ME laminate acted as a transmitter and the Helmholtz coil as the receiver. The input power at the EMR applied to the ME laminate transmitter and the voltage outputs from the receiver were measured by an oscilloscope (KEYSIGHT MSOX3014T). The power efficiency (PE), defined as:

$$\mathrm{PE} = \frac{\text{Ouput power from the receiver}}{\text{Input power to the laminate}}, \tag{4.1}$$

was plotted for varying numbers of Metglas layers, which is illustrated in Figure 4.5.

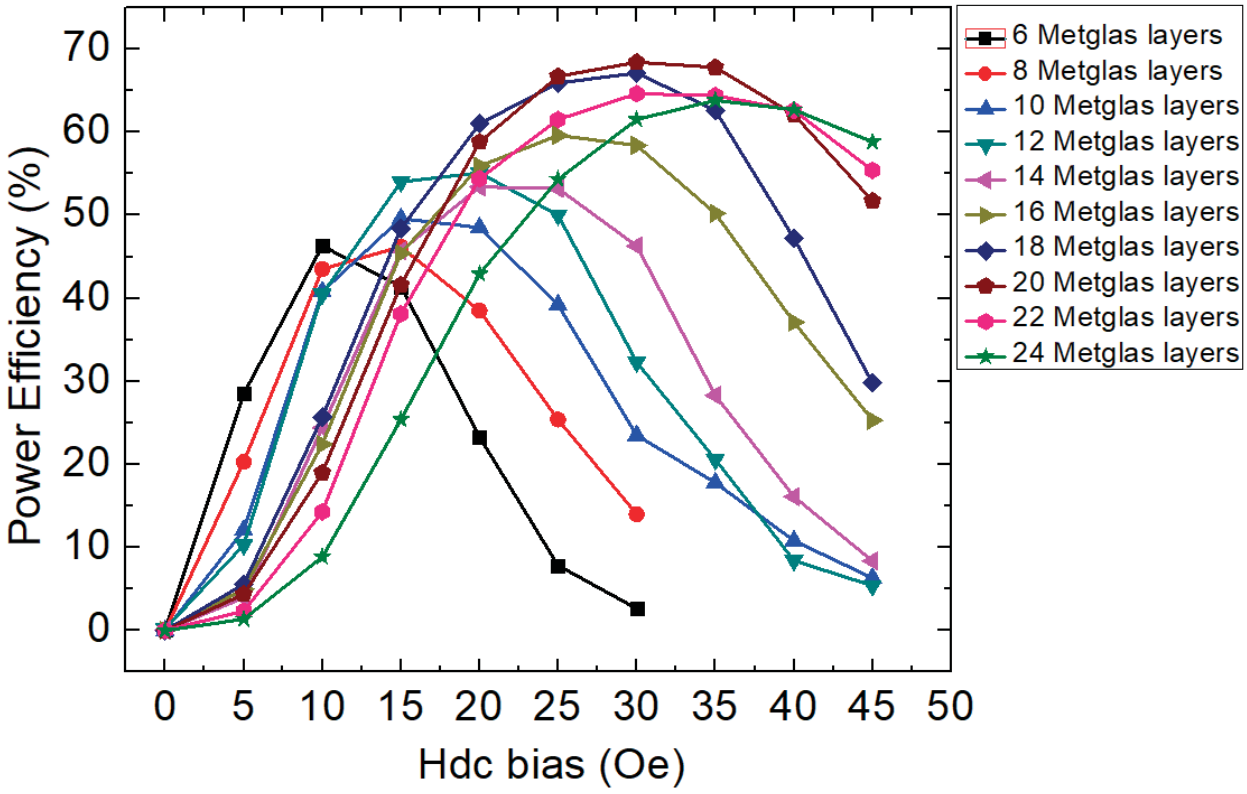


*Figure 4.5. Power efficiency of the laminate transmitter–receiver system as a function of the increasing magnetic DC bias using the ME laminates with the different numbers of Metglas layers. Xu, Junran, et al. "A low frequency mechanical transmitter based on magnetoelectric heterostructures operated at their resonance frequency." Sensors 19.4 (2019): 853, with fair use.*

The input power of the ME laminate transmitter was calculated by the voltage, the current, and the phase between the voltage and the current. For the output power of the receiver, we used an optimized resistor connected to the receiver. Therefore, the output power was calculated by the voltage, the current, and the phase difference on the optimized resistance.[64] The output power was measured from the receiver (i.e., a Helmholtz coil). Low power (4 mW–18 mW) measurements were conducted by fixing the input voltage to 10 $V_{rms}$. The power efficiency shown on the oscilloscope was then adjusted to its maximum value by varying the frequency.

Furthermore, the applied DC-magnetic field bias (Hdc) was varied from 0 Oe to 45 Oe in each case (Figure 4.5). Thus, the figure shows the results of the maximum PE at the EMR for ME laminates with different numbers of Metglas layers as a function of $H_{dc}$. The highest value of PE = 68.4% was found at Hdc = 30 Oe° for an ME laminate with 20 Metglas layers. The dimension of this laminate was 80 mm × 20 mm × 1 mm. Given its high PE value, we utilized this ME laminate with 20 Metglas layers (20M-trilayer) for subsequent investigations.

## 4.4. Transmitted magnetic flux, efficiency and pattern measurements.

Next, we investigated the induction transmission and efficiency capabilities of an ME laminate (a 20M-trilayer) at the EMR. These measurements served to increase our understanding of the potential communication properties of the ME laminate transmitter; additionally, however, by comparing a known small-loop antenna, we were also able to estimate induction transmission efficiency in the near field. Thus, we incorporated this approach in our investigation. Finally, the magnetic flux patterns of the proposed ME laminate transmitter are also presented.

We used the set-up described in Section 3.1 for characterizing the ME laminate transmitter (20M trilayer structure). We applied an input power 100 mW to the ME laminate at resonance frequency $f_r$ = 28.17 kHz. The distance between the ME laminate transmitter and the receiver, r, was then sequentially increased from 0.4 m to 1.35 m. Figure 6 shows the flux density detected by the receiver as a function of r. We measured the flux, which varied with distance, in two directions, i.e., $\theta = 0°$ and 90°. We measured the dominant flux components along each direction. Specifically, $B_r$ (along $\theta = 0°$) and $B_\theta$ (along $\theta = 90°$) were measured. As shown, the magnetic-flux levels varied between 30 nT to 1 nT in the provided distance range. As described in the following subsection,

we were able to understand more about these values by comparing our results with a small current-loop antenna.

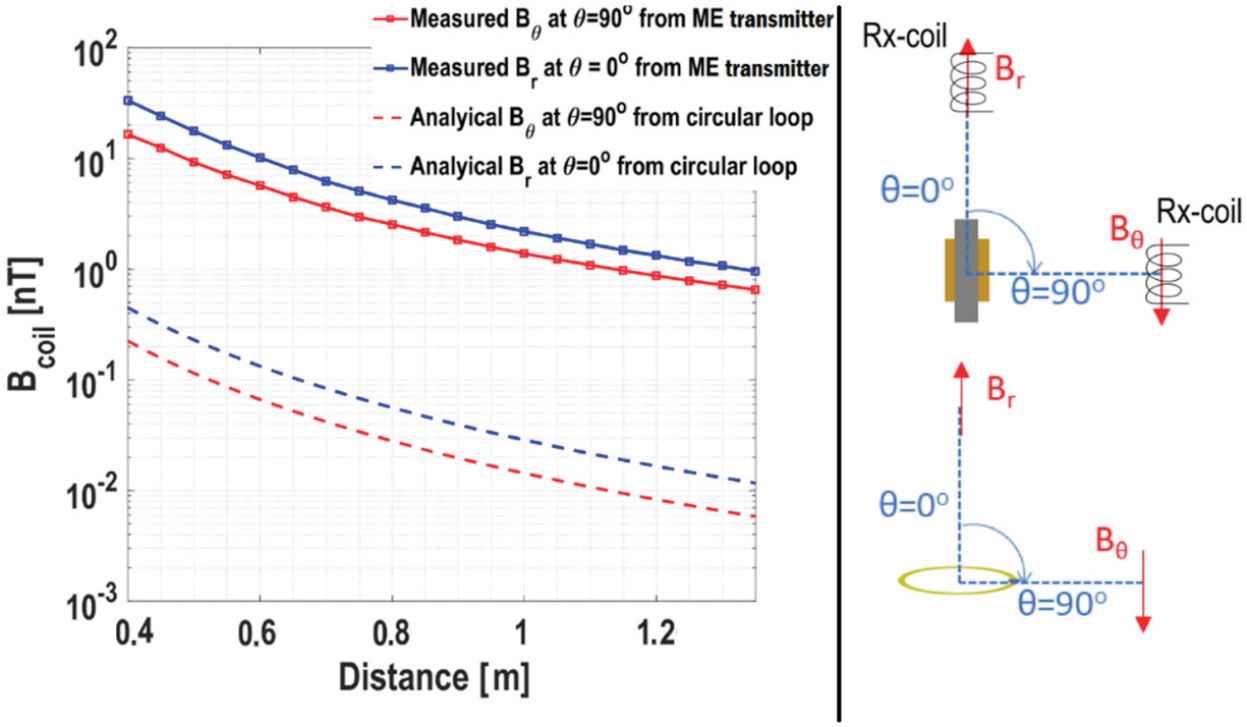


*Figure 4.6. Left figure: the magnetic flux density detected by the receiver (Rx-coil) as a function of the distance along longitudinal (θ = 0°) and transverse (θ = 90°). Right figure: the configurations of the ME laminate transmitter and the current loop. The results are compared with analytical results for a small current loop. Xu, Junran, et al. "A low frequency mechanical transmitter based on magnetoelectric heterostructures operated at their resonance frequency." Sensors 19.4 (2019): 853, with fair use.*

**(a) Comparison with a Small Current-Loop Antenna**

To understand the induction transmission capabilities of the presented ME laminate, it must be compared with analogous results from a canonical antenna structure. The size of the proposed

current loop was as same as the ME laminate, which was 16 $cm^2$. As is well known, a horizontal small circular loop is equivalent to a vertical magnetic small-dipole erected through the loop's center. Given that information, coupled with the fact that the ME laminate transmitter has a magnetic-dipole like resonance along the longitudinal direction, this comparison is appropriate (Figure 4.6, right).

First, using derivations provided in Appendix A, the near field of the small loop of radius a can be derived as:

$$|B_r| \approx \frac{\mu_o}{\sqrt{2}} \sqrt{\frac{3}{\pi \eta k^4} \frac{Z_o R_r P_{in}}{(R_r+Z_o)^2}} \left(\frac{2\cos\theta}{r^3}\right) \tag{4.2}$$

and:

$$|B_\theta| \approx \frac{\mu_o}{\sqrt{2}} \sqrt{\frac{3}{\pi \eta k^4} \frac{Z_o R_r P_{in}}{(R_r+Z_o)^2}} \left(\frac{\sin\theta}{r^3}\right). \tag{4.3}$$

Here, $P_{in}$ is the input power applied at the port of the loop antenna; $Z_o$ (= 50 Ω) is the impedance of the input transmission line; $R_r \approx 31{,}171\frac{S^2}{\lambda^4}$, with $S = \pi a^2$ is the radiation resistance of the antenna; $\eta$ = 377 Ω is the free-space radiation impedance; and the permeability of the free-space is given by $\mu_o = 4\pi \times 10{-}7$ H/m. Finally, $k = 2\pi/\lambda$ is the propagation constant for a wavelength λ. To match the measurement conditions, $P_{in}$ = 100 mW was chosen for the loop antenna, r is distance of the observation point from the center of the antenna, and θ is the angle as shown in the right-hand portion of Figure 4.6. For a reasonable comparison, we chose the loop area to be S = 16 $cm^2$ (the same as the area of ME laminate 8 × 2 $cm^2$). Note that a factor of $1/\sqrt{2}$ was added in $B_r$ and $B_\theta$ to obtain the root mean square (RMS) fluxes for the loop antenna for a viable comparison with obtained measurements. Measured $B_{coil}$ represents RMS flux density as obtained from the oscilloscope voltage (refer to Figure 4.3).

Figure 4.6 reveals a close match between the flux-distance profiles from the loop antenna and the measured ME laminate transmitter. Notably, according to Labels (4.2) and (4.3), ratio $|B_r|/|B_\theta| = 2$ would be expected. On average, this ratio was found to be $\approx 1.84$ for our experiments. This finding is in reasonable agreement since we expect diffractions, reflections, and refractions within the room, including those from the ground. Note that, because of low frequency and near-static fields ($\lambda = 10$ km), these interferences manifest themselves as constant additions of field, instead of inducing oscillations as generally expected in such distance profiles in the microwave regime. Furthermore, the empirical curve fitting suggests that the measured magnetic flux density decayed as $1/r^{2.6}$, which is comparable with theoretical values of $1/r^3$ given the various possible sources of measurement error. Finally, we also observed a difference in the flux levels from the loop antenna and the ME laminate transmitter. This discrepancy is further discussed in the efficiency subsection that follows.

We also measured the magnetic flux density generated by the ME laminate transmitter as a function of the distance with the highest power (500 mW) that we could apply. In Figure 4.7, the black curve was measured with 100 mW, and the red one was measured with 500 mW. Extrapolating the 500 mW fitting curve, it can be estimated that a 1 fT flux could be detected around 200 meters. The background magnetic noise floor in an open environment at EMR (~30 kHz) was about a few hundred fT/√Hz. Therefore, a higher input power level or a greater number of ME laminate transmitter could be added to increase transmitted magnetic fluxes.

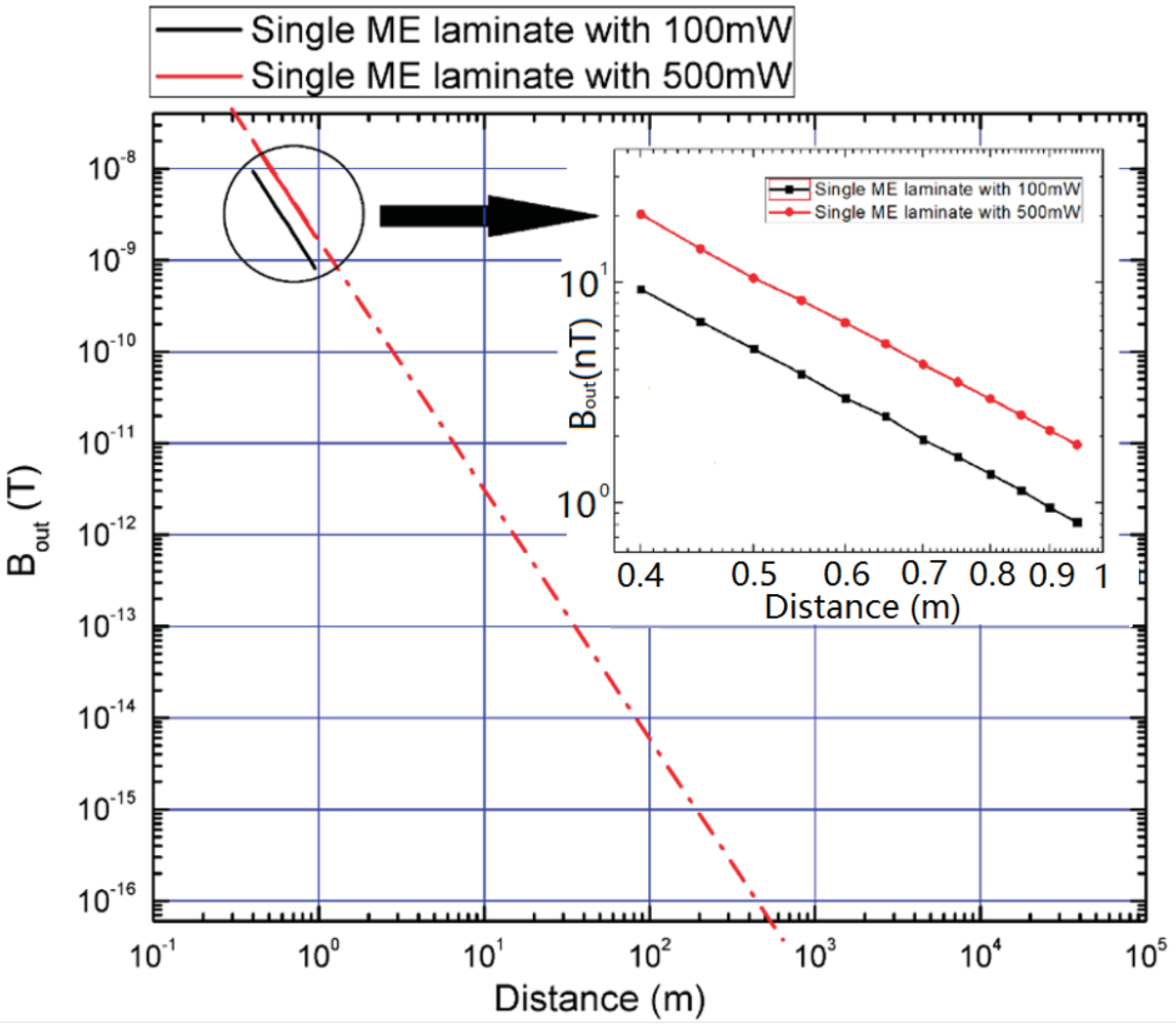


*Figure 4.7. The magnetic flux density (near-field) generated from the ME laminate transmitter as a function of the distance between the ME laminate transmitter and the receiver. The dash-dot line represents the extended line on the curve measured using a single ME laminate with 500 mW. Xu, Junran, et al. "A low frequency mechanical transmitter based on magnetoelectric heterostructures operated at their resonance frequency." Sensors 19.4 (2019): 853, with fair use.*

**(b) Induction Transmission Efficiency of the Magnetic Flux.**

Efficiency calculations generally require knowledge of total transmitted inductive power, which requires knowledge of 3D far-fields. However, such information could be difficult to capture for a kHz-range antenna due to large wavelengths. Most modern antenna chambers support measurements only above a few tens of MHz. Under these restrictions, we were able to infer the induction transmission efficiency of the proposed ME laminate transmitter by comparing its performance with the theoretical current-loop discussed above. Note that a flux ratio $|B_r|/|B_\theta| = 1.84$ confirms a similarity of ME laminate with the current loop. Furthermore, we know that the ME laminate at the EMR functions like a magnetic dipole along the longitudinal direction due to the magnetic moment's direction in the magnetostrictive layer. It is a reasonable assumption, therefore, that the flux-profile from the ME laminate and current-loop should match (as further confirmed in the pattern measurements in the next section) across a 3D space.

We also observed that the magnetic flux produced by the loop was two orders smaller than the ME laminate transmitter. For example, $B_r$ at 90 cm from the ME laminate transmitter was 2.9 nT and from the loop was 0.039 nT. This information, coupled with the known induction transmission efficiency of the current loop, can be used to calculate the induction transmission efficiency of the proposed ME laminate transmitter. We know that induction transmission efficiency is proportional to magnetic flux squared. Thus, the efficiency ratio of an ME antenna ($\eta_{ME}$) and current loop ($\eta_{loop}$) will follow as:

$$\frac{\eta_{ME}}{\eta_{loop}} = \left(\frac{|B_{r_{ME}}|}{|B_{r_{loop}}|}\right)^2 \approx 5.5 \times 10^3. \tag{4.4}$$

Accordingly, the induction transmission efficiency in the near field of the proposed ME laminate transmitter would be expected to be three to four orders higher than a current loop of the same area. This finding confirms the superior operation of the proposed ME laminate transmitter under both

near-field and far-field conditions. The proposed ME laminate transmitter would be particularly efficient in instances when the packing area is small, since it can provide higher efficiency within the same size.

We also point out that the efficiency of the current loop was extremely low ($\eta_{loop} = 1.2 \times 10^{-19}$) due to a $\ll \lambda$ restriction at kHz range.[83] That is, since the current loop is non-resonant, its radiation resistance was negligible as compared to the impedance parameters of a typical transmission line, indicating that most power will simply reflect back from the antenna port. In other words, the factor $1-|S_{11}|^2$ is negligible. This finding represents a typical challenge for antennas that are operating at much longer wavelengths than their size. Even with such severe impedance-matching challenges, the proposed ME laminate provides substantial improvements for low frequency (~30 kHz) induction transmissions, causing the induction transmission efficiency to be estimated in the order of $10^{-16}$, which is three orders larger than for the current loop of the same size.

**(c) Pattern Measurements**

In terms of the orientation of the ME laminate transmitter, we assumed the ME laminate transmitter's longitudinal direction to be along the Z-axis, the width along the X-axis, and the thickness along the Y-axis. Magnetic flux pattern measurements were obtained by sweeping the elevation angle $\theta$ in the XZ (or 001)-plane, YZ (or 010)-plane and XY (or 100)-plane. We chose to measure the Br component for these measurements by orienting the axis of the search coil towards the center of the sweeping circle. The radius of the circle was 0.5 m. The input power applied was 100 mW. The ME laminate transmitter was working at its EMR in all cases, and the measurement set-up was similar to Figure 4.3, but applied for varying $\theta$.

The resulting normalized magnetic-flux-pattern profiles are shown in Figure 4.8a, b and c. The maximum value of the magnetic flux density was 4.75 nT, which is depicted in the red curve of Figure 4.8d. The fluxes in the XZ- and YZ-planes were normalized to their maximum value, as both fluxes were found to be in the tens on nT range. For the XY-plane, the fluxes were found to be one order smaller than the XZ, YZ-planes. The normalization was conducted with a maximum of the XZ-plane to show the NULL along the XY-plane (Figure 4.8c).

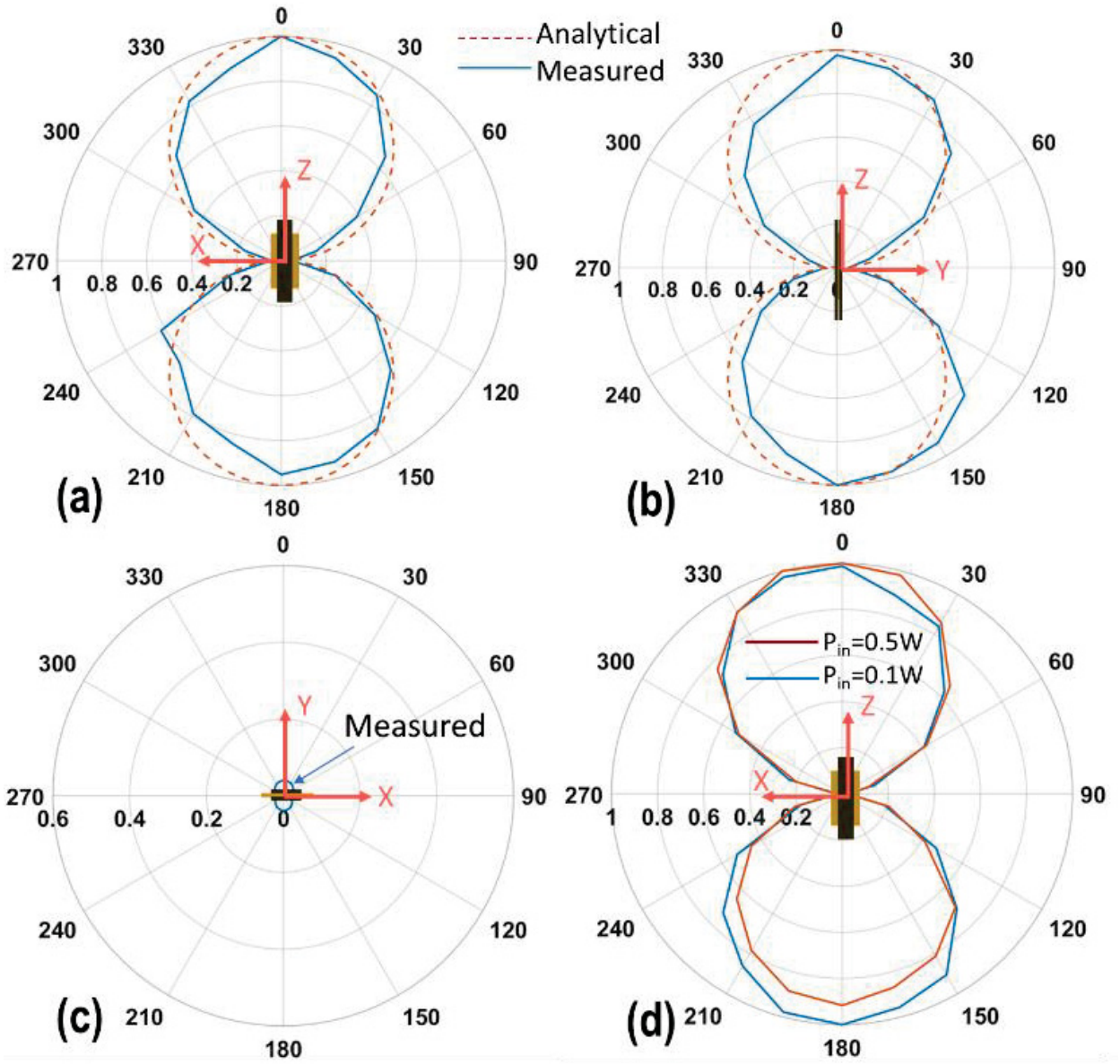


*Figure 4.8. The measured normalized radial magnetic flux (Br (θ)) of the ME laminate transmitter as a function of elevation angle θ in (a) XZ (or 001)-plane, (b) YZ (or 010)-plane, (c) XY (or 100)-plane, and (d) linearity performance of the ME laminate transmitter as shown with two different power levels. Xu, Junran, et al. "A low frequency mechanical transmitter based on magnetoelectric heterostructures operated at their resonance frequency." Sensors 19.4 (2019): 853, with fair use.*

The $B_r$ flux component followed the cosine flux profile for XZ-(001) and YZ-(010) planes, confirming a magnetic-dipole-like (or horizontal small-loop) operation predicted by Label (4.2). Note that the detected flux in the XY (100)-plane in Figure 4.8c was one order smaller than Figures 4.8a and b, which effectively represents a NULL at $\theta = 90°$ based on Label (4.2). However, the power in the (100) plane was still measurable, which is likely attributable to the slight asymmetry of the ME laminate transmitter and receiver.

Additionally, we compared the obtained normalized magnetic flux patterns using a single ME laminate under input powers of 100 mW and 500 mW along the XZ-(001) plane. Both patterns are shown in Figure 4.8d. Their overlap confirms the linear operation of the ME laminate transmitter, i.e., the transmitted fluxes linearly increase with applied input power. This is an important observation, given the nonlinear physics of the ME laminates under consideration.

**Appendix A**

For a circular loop of radius a, and constant current $I_o$, the near field under the approximation $k_r \ll 1$ is given by:[84,85]

$$H_r \approx \frac{a^2 I_o e^{-jkr} \cos\theta}{2r^3}, \tag{A1}$$

$$H_\theta = \frac{a^2 I_o e^{-jkr} \sin\theta}{4r^3}, \tag{A2}$$

$$H_\phi = E_r = E_\theta = 0, \tag{A3}$$

$$E_\phi \approx -\frac{ja^2 k I_o e^{-jkr}}{4r^2} \sin\theta. \tag{A4}$$

Here, $k = 2\pi/\lambda$ is the propagation constant and r is the distance of the radiator from the measurement point. Thus, the maximum of the H-fields along the longitudinal and transverse directions are provided by $H_r$ at $\theta = 0°$ and $H_\theta$ at $\theta = 90°$, respectively. Furthermore, geometrical and current related parameters can be replaced by total radiated power using the relation:

$$P_{rad}=\eta\left(\frac{\pi}{12}\right)k^4\left(a^2|I_o|\right)^2, \tag{A5}$$

which provides $a^2|I_o| = \sqrt{\frac{12P_{rad}}{\pi\eta k^4}}$, and thus equations for $H_r$ and $H_\theta$ can be written as:

$$|H_r|\approx\sqrt{\frac{12\,P_{rad}}{\pi\eta k^4}}\left(\frac{\cos\theta}{2r^3}\right) \tag{A6}$$

and

$$|H_\theta|\approx\sqrt{\frac{12\,P_{rad}}{\pi\eta k^4}}\left(\frac{\sin\theta}{4r^3}\right)\ . \tag{A7}$$

We further note that $P_{rad} = (1-|S_{11}|^2)$ Pin, where Pin is the applied power to the antenna and $S_{11}$ is the reflection coefficient due to antenna and transmission line-impedance mismatch. Given the radiation resistance of the loop antenna to be $Rr \approx 31{,}171\frac{S^4}{\lambda^2}$, where $S = \pi a^2$ is the area of the loop and characteristic impedance of the coaxial cable as Zo = 50 Ω, we write $|S_{11}|=|(\frac{Z_o-R_r}{Z_o+R_r})|$ and $P_{rad} = P_{in}\,(1-|S_{11}|^2) = P_{in}\frac{4Z_oR_r}{(R_r+Z_o)^2}$. Thus, the magnetic field can be calculated in terms of input power as:

$$|H_r|\approx\sqrt{\frac{3}{\pi\eta k^4}\frac{Z_oR_rP_{in}}{(R_r+Z_o)^2}}\left(\frac{2\cos\theta}{r^3}\right) \tag{A8}$$

and:

$$|H_\theta|\approx\sqrt{\frac{3}{\pi\eta k^4}\frac{Z_oR_rP_{in}}{(R_r+Z_o)^2}}\left(\frac{\sin\theta}{r^3}\right). \tag{A9}$$

Furthermore, magnetic-field flux components $B_\theta$ and $B_r$ can be evaluated by using $B_\theta = \mu_o H_\theta$ and $B_r = \mu_o H_r$.

## 4.5. Summary of this section

In this work, we investigated the optimization of an ME laminate transmitter and measured its magnetic fluxes at EMR (~30 kHz). As opposed to large current radiation antennas for kHz, the

proposed approach used mechanical vibrations to excite induction transmission using piezo and magneto laminates. Furthermore, the induction transmission efficiency in the near field was optimized by increasing the number of Metglas layers. The enhanced magnetic flux density provides proof-of-concept for miniaturization of low-frequency laminate transmitter based on mechanical-magnetic effects.

Our results clearly demonstrate the potential for developing small portable devices with significantly enhanced magnetic flux density in the 30 kHz frequency range. Even with the observed small induction transmission efficiency in the near field, the presented values are several orders higher than a current loop of the same size. Furthermore, the background magnetic noise floor in an open environment at EMR (~30 kHz) is about a few hundred fT/√Hz. While a higher input power level or a larger number of ME laminate transmitters could be added to increase magnetic flux through induction transmission, these modifications would invariably compromise size parameters. These effects, along with impedance matching concerns, represent worthy areas for future work.

# CHAPTER 5: ME GYRATOR APPLICATION

## 5.1. Introduction.

In 1948, Tellegen proposed a passive linear electronic device with both an inductive port and a capacitive port. With its two-port configuration, this device was defined as the fifth basic electric element. In 2006, Zhai et al. was the first to demonstrate gyrator features in ME laminates. Due to the giant ME effect, the incorporation of an ME laminate represents an ideal strategy for achieving a gyrator structure, which can then convert magnetic energy forms to electric forms, or vice-versa. The giant ME effect can be further enhanced when ME laminates are driven under mechanical resonance frequency. The magnetic and electric energy forms can be converted through magnetostrictive and piezoelectric phases via mechanical coupling between the two phases. Accordingly, a gyrator can be realized by using an ME laminate with a search coil, where both the former and latter can either be an electric output and a magnetic input, or an electric input and a magnetic output.

The energy conversion of an ME gyrator can be broken down into three steps. The first step is the energy conversion from electric form to magnetic form using the search coil as an input. Second, the conversion occurs from the magnetic form to the elastic form on the magnetostrictive phase of the ME laminate. Third, the conversion will conclude from the elastic form to the electric form on the piezoelectric phase, which also represents the output of the ME gyrator. The power efficiency of an ME gyrator strongly depends on the power conversion and power loss. The power conversion can be separated into (a) electro-magnetic coupling in the search coil, and (b) ME coupling between the magnetostrictive and piezoelectric phases of the ME laminate. In order to achieve the highest power efficiency, we need to increase the electro-magnetic coupling of the

search coil and the ME coupling of the ME laminate, while at the same time decreasing power loss. The power loss is designated as wasted power, which is caused by the dissipation of the ME gyrator.

Prior studies show that the power efficiency of an ME gyrator is related to the dissipation and the power loss in that gyrator.[86] First, the current flow in a coil creates a loss of power due to the resistance of the coil. Second, the power loss that occurs in an ME laminate consists of three elements: 1) Eddy current generated in the magnetostrictive phases, which is caused by the induced current due to a magnetic field; 2) Internal friction and compliance loss between the magnetostrictive and piezoelectric materials result in mechanical loss due to the laminated structure; and 3) In piezoelectric phases, the dielectric loss and the resistive loss represent the principal drivers of electrical loss in an ME laminate. However, the two dominant sources of power loss in an ME gyrator were finally determined as the resistance loss in the coil and the mechanical dissipation in the ME laminates working at their resonance frequency. Accordingly, the power efficiency of an ME gyrator (PE) can be expressed as[86]

$$\text{PE} \approx 1 - \frac{1}{k_{eff,m}^2 Q_{mech}} , \tag{5.1}$$

where $k_{eff,m}$ is the effective magneto-mechanical coupling factor, and $Q_{mech}$ is the mechanical quality factor of the ME laminate.

The power loss of ME gyrators also has been investigated, which showed that high-power conversion efficiency can be realized by increasing the mechanical coupling and mechanical quality factor of the ME gyrators. Recently, the power efficiency of ME gyrators has been improved to 90% through the incorporation of Metglas.

There are two basic methods for characterizing an ME gyrator, which are shown in Fig 5.1. The first approach is through IV or VI measurements. In order to obtain IV measurements, the output voltage is measured by a pre-amplifier with a 10MΩ in open-circuit conditions. In the case

of VI measurements, a current amplifier with a 1Ω impedance is used to measure the output current in closed-circuit conditions. The second approach for characterizing an ME gyrator is by assessing its power efficiency. For this measurement approach, we used a variable resistor $R_L$, which was connected to the output port so that the output power could be calculated by $V_R^2/R_L$, while the input power was calculated by a real part of $V_{in}$ and $I_{in}$.

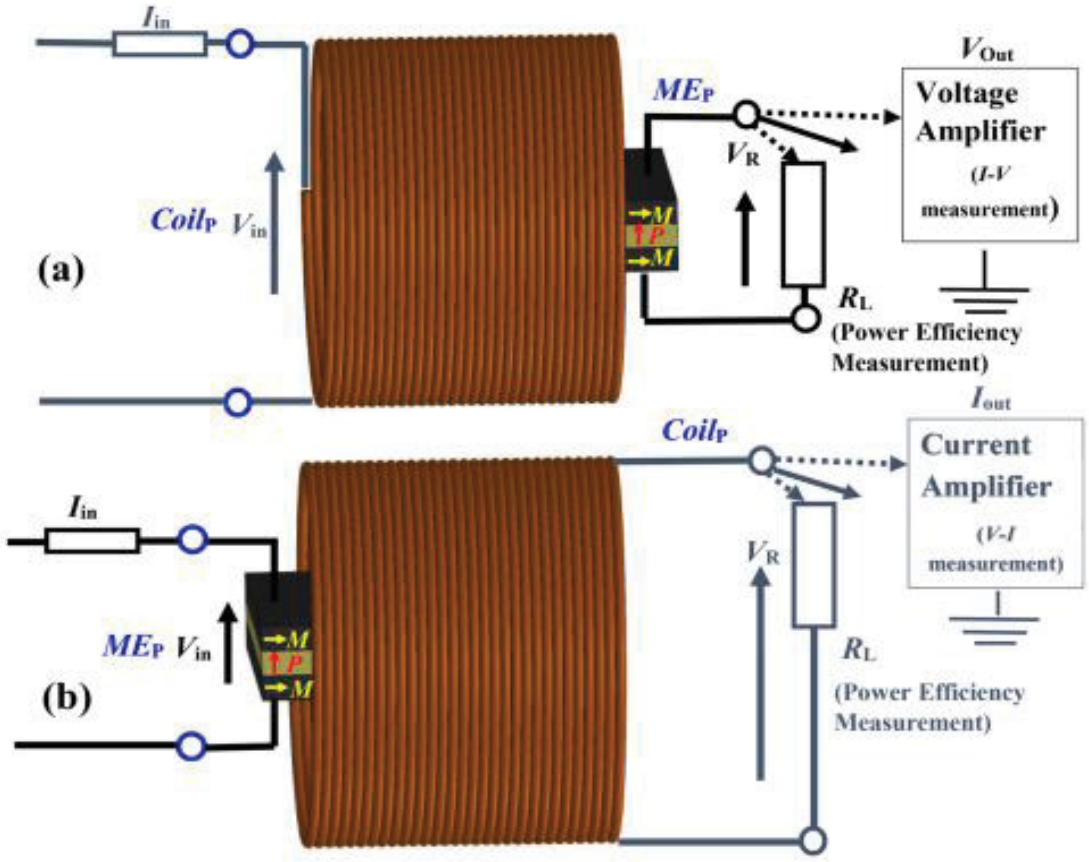


*Figure 5.1. (a) I-V and V-I measurement. (b) Power efficiency measurement. Leung, Chung Ming, et al. "Power conversion efficiency and resistance tunability in coil-magnetoelectric gyrators." Applied Physics Letters 109.20 (2016): 202907, with fair use.*

## 5.2. Impedance mismatch and resonance frequency mismatch.

Under actual application conditions, acoustic transducers are driven by power amplifiers. Accordingly, power amplifiers are required to have good linearity and a wide bandwidth for optimal transducer performance. Designing linear power amplifiers that operate reliably at high frequency is quite challenging, which is mainly due to the fact that the parasitic impedances of their electronic components tend to dominate at higher frequencies, thereby leading to significant power-efficiency loss. At the same time, the electro-acoustic coupling factor of acoustic transducers is also limited by the bandwidth, over which the transducer can be impedance-matched to a power amplifier. Acoustic transducers fabricated with piezoelectric materials feature a large capacitance. When exhibiting optimal performance they are usually operating under their electromechanical resonance (EMR) frequency. Note that a standard power amplifier only has a fixed impedance of 50Ω. In contrast, the input electric impedance of transducers features a huge capacitance, which can lead to a significant impedance mismatch between power amplifiers and acoustic transducers. Based on previous research, ME gyrators displaying high power-conversion efficiency have also been fabricated with piezoelectric materials, which have similar impedance properties as acoustic transducers. Therefore, it is possible to configure an ME gyrator between a power amplifier and an acoustic transducer to resolve the impedance-mismatch problem, and this phase of the investigation focused on this problem.

Based on this assumption, there will be an EMR-frequency mismatch between an acoustic transducer and an ME gyrator due the different structures and dimensions. This EMR-frequency mismatch will also result in a significant degradation of power efficiency, especially when the frequency difference is substantial.

## 5.3. Equivalent circuit development.

In order to resolve the EMR-frequency mismatch between an ME gyrator and an acoustic transducer, an equivalent circuit of an ME gyrator connected to an acoustic transducer needs to be developed. Fig. 5.2(a) shows the schematic of the proposed ME gyrator and the acoustic transducer. As detailed in this chapter, the acoustic transducers we used are PZT layers. The structure of the ME gyrator is composed of a longitudinal-transverse (L-T) mode ME laminate, which is located in the center of a copper coil. The ME laminate is connected to one end of a PZT layer, and the other end of the PZT layer is connected to a resistance load, which is used for the optimized output power.

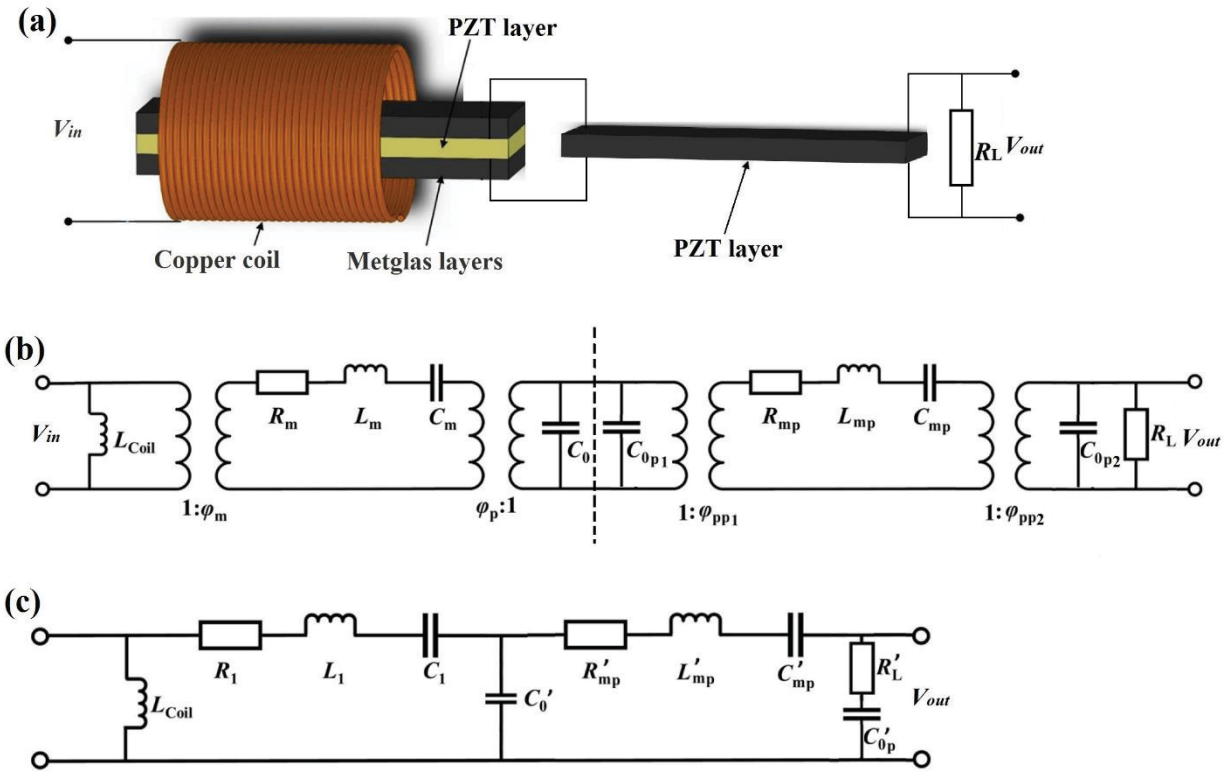


*Figure 5.2. (a) Schematic of the proposed ME gyrator and the acoustic transducer, (b) equivalent circuit working at resonance frequency, (c) simplified circuit working at resonance frequency.*

Both the ME gyrator and the PZT layer are working under free vibration conditions. The equivalent circuit of the ME gyrator connected to the PZT layer working at resonance frequency is shown in Fig. 5.2(b). The left side of the dashed line represents the equivalent circuit of the ME gyrator, while the PZT layer is on the right. With the constitutive equations (1.7), the impedance of the ME laminate can be divided into mechanical resistance $R_m$, mechanical inductance $L_m$, and mechanical capacitance $C_m$. $C_0$ is the electric capacitance of the ME laminate. $\varphi_m$ and $\varphi_p$ are the magneto-elastic and the electro-elastic coupling factors of the ME laminate, respectively. The impedance of the PZT layer also can be divided into mechanical resistance $R_{mp}$, mechanical inductance $L_{mp}$, and mechanical capacitance $C_{mp}$. $C_{0p1}$ and $C_{0p2}$ are the electric capacitance of the PZT layer on two sides. $\varphi_{pp1}$ and $\varphi_{pp2}$ are the electro-elastic coupling factors of the PZT layer on two sides. All the parameters are expressed below.[78]

$$\begin{cases} R_m = \frac{\pi Z_0}{8Q_m} \\ L_m = \frac{\pi Z_0}{8\omega_s} \\ C_m = \frac{1}{\omega_s L_m} \\ C_0 = \frac{wl}{t_p}\varepsilon_{33}^S \\ \varphi_m = 2A_m \frac{d_{33,m}}{s_{33}^H} \\ \varphi_p = \frac{wd_{31,p}}{s_{11}^E} \\ Z_0 = \overline{\rho v} A_{lam} \end{cases} \qquad \begin{cases} R_{mp} = \frac{\pi Z_{0p}}{8Q_{mp}} \\ L_{mp} = \frac{\pi Z_{0p}}{8\omega_{sp}} \\ C_{mp} = \frac{1}{\omega_{sp} L_{mp}} \\ C_{0p} = \frac{w_p l_p}{t_{pp}}\varepsilon_{33}^S \\ \varphi_{pp1} = \frac{w_1 d_{31,p}}{s_{11}^E} \\ \varphi_{pp2} = \frac{w_2 d_{31,p}}{s_{11}^E} \\ Z_{0p} = \overline{\rho_p v_p} A_{lamp} \end{cases} \tag{5.2}$$

where $Z_0$ and $Z_{0p}$ are the impedance of the ME gyrator and the PZT layer, respectively. $Q_m$ is the mechanical quality factor of the ME gyrator. $\rho$ is the density of the laminate, v is the sound velocity, ω and $\omega_s$ are the angular frequency and the angular frequency at resonance.

In order to simplify the equivalent circuit of the ME gyrator connected to the PZT layer, Fig 5(c) was developed for the circuit analysis. On the left side, the ME gyrator circuit contains the equivalent resistance $R_1 = \frac{R_m}{\varphi_m^2}$, the equivalent inductance $L_1 = \frac{L_m}{\varphi_m^2}$, the equivalent capacitance $C_1 = C_m\varphi_m^2$. Similarly, the PZT circuit on the right side contains the equivalent resistance $R'_{mp} = \frac{R_{mp}}{\varphi_{pp1}^2}$, the equivalent inductance $L'_{mp} = \frac{L_{mp}}{\varphi_{pp1}^2}$, the equivalent capacitance $C'_{mp} = C_{mp}\varphi_{pp1}^2$. The expressions for the electric capacitance at end of the PZT layer and the load resistance of the whole system are shown below,

$$\begin{cases} C'_{0p} = \dfrac{1+\omega^2\left(\frac{R_L}{1+\omega^2R_L^2C_{0p2}^2}\frac{\varphi_{p2}^2}{\varphi_{p1}^2}+\frac{1+\omega^2R_L^2C_{0p2}^2}{\omega^2R_L^2C_{0p2}}\frac{\varphi_{p1}^2}{\varphi_{p2}^2}\right)^2(C_0+C_{0p1})^2}{\omega^2\left(\frac{R_L}{1+\omega^2R_L^2C_{0p2}^2}\frac{\varphi_{p2}^2}{\varphi_{p1}^2}+\frac{1+\omega^2R_L^2C_{0p2}^2}{\omega^2R_L^2C_{0p2}}\frac{\varphi_{p1}^2}{\varphi_{p2}^2}\right)C_{0p2}^2}\dfrac{\varphi_p^2}{\varphi_m^2} \\ R'_L = \dfrac{\frac{R_L}{1+\omega^2R_L^2C_{0p2}^2}\frac{\varphi_{p2}^2}{\varphi_{p1}^2}+\frac{1+\omega^2R_L^2C_{0p2}^2}{\omega^2R_L^2C_{0p2}}\frac{\varphi_{p1}^2}{\varphi_{p2}^2}}{1+\omega^2\left(\frac{R_L}{1+\omega^2R_L^2C_{0p2}^2}\frac{\varphi_{p2}^2}{\varphi_{p1}^2}+\frac{1+\omega^2R_L^2C_{0p2}^2}{\omega^2R_L^2C_{0p2}}\frac{\varphi_{p1}^2}{\varphi_{p2}^2}\right)^2(C_0+C_{0p1})^2}\dfrac{\varphi_p^2}{\varphi_m^2} \end{cases} . \quad (5.3)$$

## 5.4. Impedance match of whole system.

Since the ME gyrator developed during this study displayed over 90% power conversion efficiency, we can use it as a platform between a power amplifier and a PZT transducer to address the problem of impedance mismatch. One problem associated with the impedance mismatch between the ME gyrator and the PZT layer is the resistance load we used at the output end. Therefore, the optimized resistance load needs to be determined in order to achieve the highest power efficiency possible.

This study was also designed to test a tri-layer L-T mode ME gyrator with a magnetostrictive-piezoelectric-magnetostrictive structure. The magnetostrictive and piezoelectric phases are Metglas layers and a PZT layer, respectively. The ME gyrator featured the following dimensions:

50 mm length, 6mm width, and 2.2 mm thickness. The PZT layer was 8.5 mm in width and 2 mm in thickness; its length was initially 42 mm but was decreased to 28 mm due to the size reduction. Figure 5.3 shows the power efficiency of the single PZT layer as a function of the increasing resistance load at the output end of the circuit (see Fig. 5.2). The best results we obtained were around 91.2% - 98.9% under the optimized resistance load of 3 kOhm, regardless of how many times size reduction. The power efficiency of the ME gyrator connected to the PZT layer with the optimized resistance load was also checked. The results showed that both the highest efficiency of PZT layer and the highest efficiency of ME gyrator connected to PZT layer (Fig 5.3) occurred with the same optimized resistance load, which was 3 kOhm.

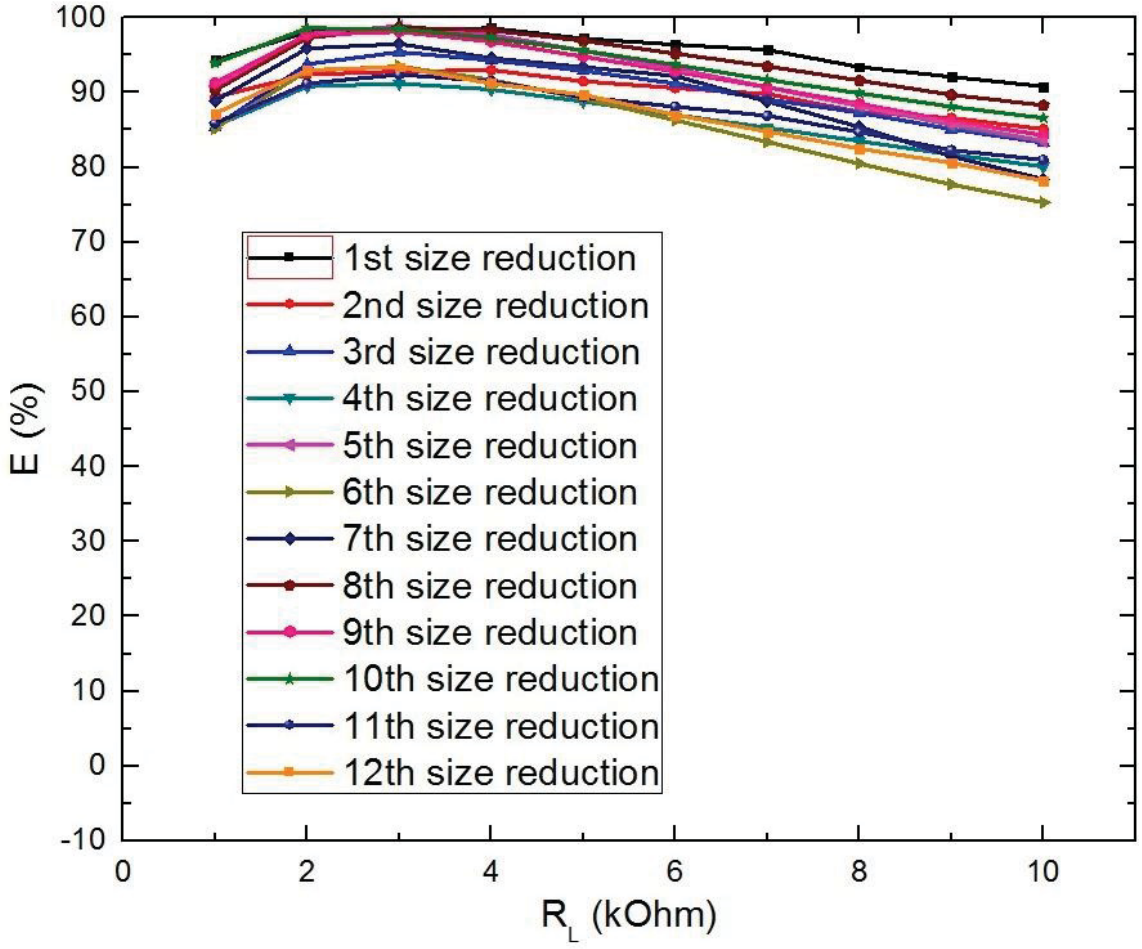


*Figure 5.3. Power efficiency of ME gyrator as a function of resistance loads.*

## 5.5. Resonance frequency tuning.

5.5.1. Size reduction.

For use in actual applications, the total power-conversion efficiency of the ME gyrator connected to the PZT layer needs to be improved by adjusting the EMR frequency of the PZT layer. There are two approaches for adjusting the EMR frequency. First, because the EMR frequency of the PZT layer is lower than that of the ME gyrator, we can shorten the length of the PZT layer to make the EMR of the PZT layer move from left to right on the frequency spectrum. Figure 5.4 shows the power efficiency of the ME gyrator connected to the PZT layer as a function of frequency based on a range of length reductions. Specifically, the length of the PZT layer was decreased from 42 mm to 28 mm over a total of 12 size reductions. From the 1st size reduction to 9th size reduction, the EMR frequency of the PZT layer was initially quite distant from the EMR frequency of the ME gyrator; however, the two peaks became closer with each subsequent length reduction of the PZT layer. Furthermore, both the efficiency of the PZT layer and the ME gyrator increased rapidly. However, for each size reduction, the efficiency of PZT layer was higher than that of the ME gyrator. This trend can be attributed to the fact that the power efficiency strongly depends on the mechanical quality factor ($Q_{mech}$) and the effective magneto-mechanical coupling factor ($k_{eff,m}$) of the material, which is based on equation 5.1. Compared with the mechanical quality factor of the PZT layer and the ME laminate, the $Q_{mech}$ of PZT is much higher than the corresponding data for Metglas: therefore, the $Q_{mech}$ of PZT is higher than that of the ME gyrator. Meanwhile, the efficiency of the ME gyrator is also influenced by $k_{eff,m}$, which is a number less than 1. In contrast, the PZT layer will not affected by this parameter due to the absence of the magnetostrictive phase. After the 10th size reduction (green curve), the peaks of PZT layer and the ME gyrator were basically overlapped at the same EMR frequency, which also represents the

optimized case in terms of impedance match; the efficiency of the entire system achieved its highest value under said condition, which was 82.2%. At this point, the power efficiency of the whole system can be theoretically calculated as:

$$E_{\_total}\,(\%) = E_{\_ME\ gyrator}\,(\%) \cdot E_{\_PZT}\,(\%)\ . \tag{5.4}$$

As calculated from this equation, the power efficiency of the ME gyrator and the PZT layer were 90.3% and 98.5%, respectively. Therefore, the calculated efficiency will be 88.9%, which is reasonably close to the measured value of 82.2% at EMR. During the 11$^{th}$ and 12$^{th}$ size reductions, the EMR frequency of the PZT moved to the right of the EMR frequency of the ME gyrator, and the efficiency decreased rapidly due to the impedance mismatch of the PZT layer and the ME gyrator.

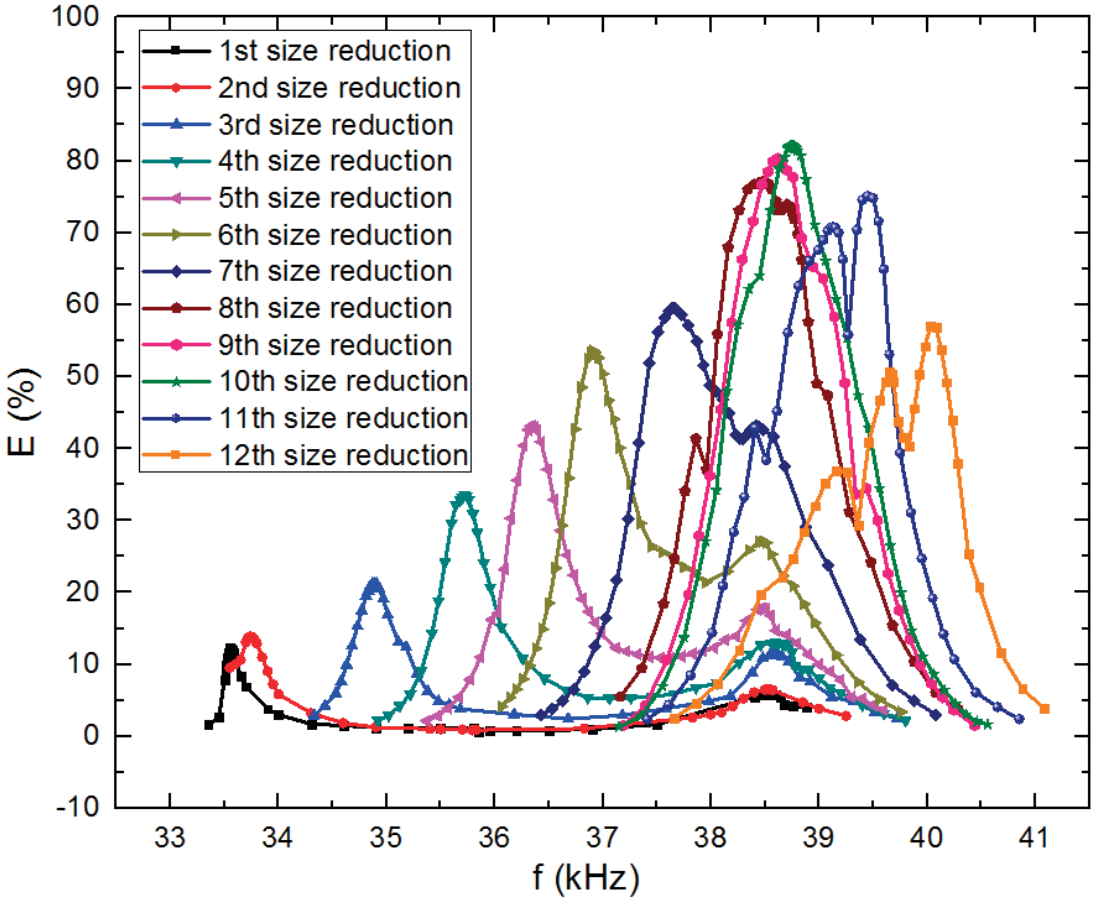


*Figure 5.4. Power efficiency of ME gyrator connected with PZT layer as a function of frequency.*

5.5.2. Capacitor and inductor tuning.

As described in the prior paragraph, the EMR of the PZT layer can be increased from left to right to match the EMR of the MR gyrator. However, if the EMR of the PZT layer is already higher than that of the ME gyrator, we cannot change the size of the PZT layer to achieve an EMR frequency match. Therefore, it is so important to focus on whether the EMR of the PZT layer can be moved from right to left, or from left to right by using other methods. The capacitor and inductor can play important roles in further investigating the above-mentioned issue. The tuning capacitor or the tuning inductor is parallel to the resistance load at the output end of the circuit (in the red dash line block of Fig 5.5(a)). In other words, only the capacitor or the inductor will be parallel to the resistance load. Therefore, the expression of the tuning capacitor $C_L'$ or the tuning inductor $L_L'$ in Fig. 5.5(b) and (c) can be determined as,

$$\begin{cases} C_L' = \frac{1+\omega^2(C_{op}'+R_L')^2C_L^2}{\omega^2(C_{op}'+R_L')^2C_L^2}\frac{\varphi_{pp1}^2}{\varphi_{pp2}^2} \\ L_L' = \frac{L_L}{1+\omega^2(C_{op}'+R_L')^2L_L^2}\frac{\varphi_{pp1}^2}{\varphi_{pp2}^2} \end{cases}. \tag{5.3}$$

As indicated in Figure 5.5(b) and (c), $C_L'$ or $L_L'$ are connected to $R_{mp}'$, $L_{mp}'$, and $C_{mp}'$ in series. The angular frequency at EMR $\omega_s = \frac{1}{L_m C_m}$. Therefore, the shifted frequency of the EMR caused by the tuning capacitor ($\Delta\omega_C$) and the tuning inductor ($\Delta\omega_L$) can be determined as,

$$\begin{cases} \Delta\omega_C = \frac{1}{L_{mp}'C_{mp}'} - \frac{1}{(\frac{C_{mp}'C_L'}{C_{mp}'+C_L'})L_{mp}'} \\ \Delta\omega_L = \frac{1}{L_{mp}'C_{mp}'} - \frac{1}{(L_{mp}'+L_L')C_{mp}'} \end{cases}. \tag{5.4}$$

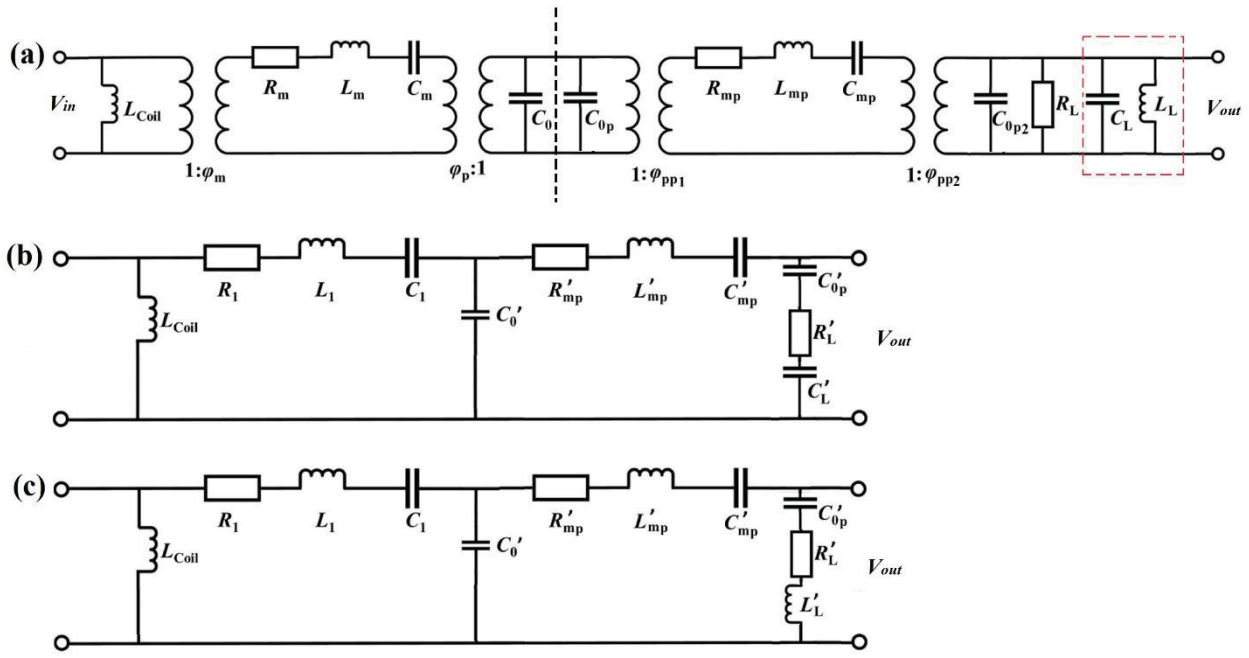


*Figure 5.5. (a) Equivalent circuit of the proposed ME gyrator and the acoustic transducer with tuning capacitor or tuning inductor, (b) simplified circuit working at resonance frequency with tuning capacitor, (c) simplified circuit working at resonance frequency with tuning inductor.*

Figure 5.6 shows the power efficiency of an ME gyrator connected to a PZT layer as a function of the shifted EMR frequency of the PZT layer with the increasing electric capacitors. Initially, when the tuning capacitor had not yet been applied to the circuit, we noted the highest efficiency value of 76.4%. As the capacitor was increased from 0 pF to 1000 pF, that efficiency level decayed from 76.4% to 63.7%. In terms of shifting the EMR frequency of the PZT layer, it could only be moved from right to left, which resolved the issue of whether the EMR frequency of the PZT layer is on the right of the ME gyrator. Using this method, therefore, the EMR frequency can be moved to match the EMR frequency of the ME gyrator. The furthest shift in frequency we were able to achieve was 240 Hz, with a corresponding power loss of approximately 12.7%.

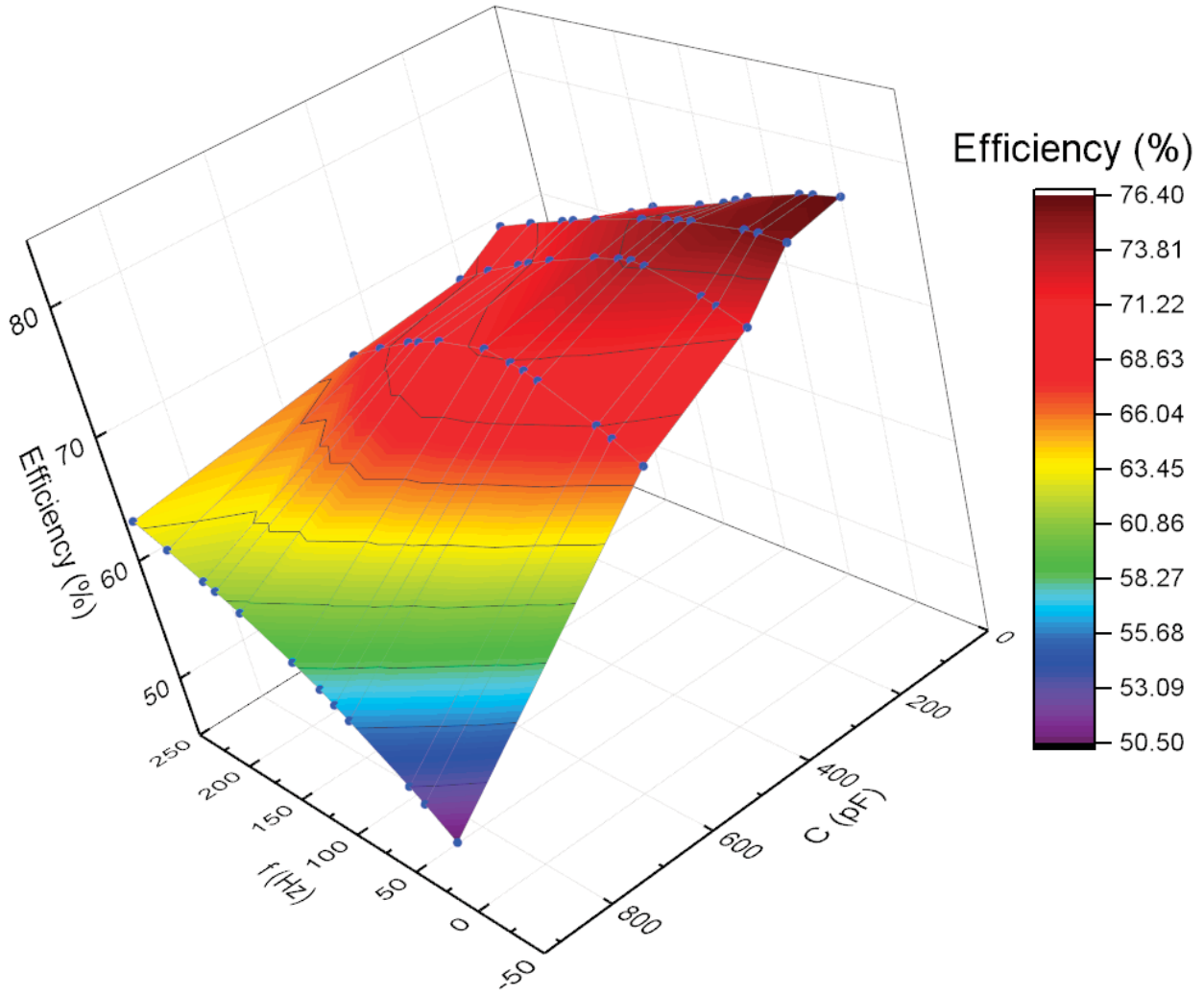


*Figure 5.6. 3D Power efficiency of the ME gyrator connected to the PZT layer as a function of the shifted EMR frequency of the PZT layer with the increasing electric capacitors.*

Correspondingly, Figure 5.7 shows the power efficiency of an ME gyrator connected to a PZT layer as a function of the shifted EMR frequency of the PZT layer with the increasing electric inductors. Similarly, the efficiency achieved its highest value of 81% when the tuning inductor had not yet been applied to the circuit. As the inductor was increased from 0 mH to 300 mH, the efficiency initially decayed from 76.4% to 70.5%, then increased to 83.3%; by the end of the assay it had further decreased slightly to 81.2%. We attribute this trend to the fact that for a system

featuring an ME gyrator and a PZT layer working at their EMR, the internal electric capacitor dominates the impedance of the system. Under this condition, the efficiency will be decreased when an external electric capacitor is introduced into the circuit. On the plus side, the addition of an external inductor, which results in decreasing the influence of the internal electric capacitor to the circuit, may ultimately afford the opportunity to increase the efficiency of the entire system. This flexibility represents a significant advantage in comparison to using a tuning capacitor: efficiency can be maintained through the incorporation of an inductor to tune the EMR frequency. In terms of the shifted EMR frequency of the PZT layer, our findings confirmed that it could be moved from both right to left, as well as from left to right, which serves to enable the EMR frequency shift of the PZT layer close to the EMR of the ME gyrator. The furthest shifted frequency from right to left was also 240 Hz without any loss of power. In contrast, the furthest shifted frequency from left to right was 20 Hz without any loss of loss. This finding represents the second advantage compared to use a tuning capacitor.

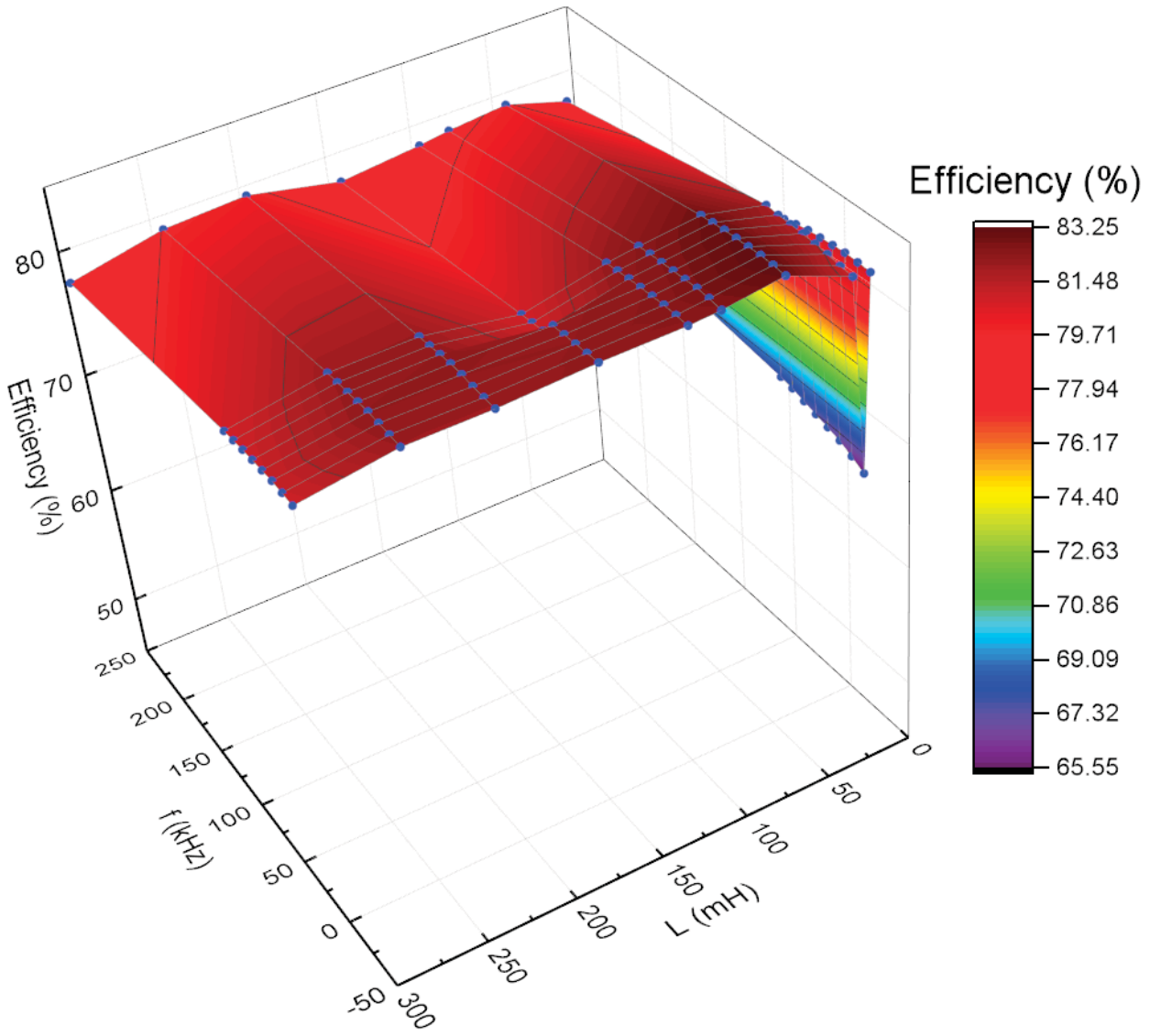


*Figure 5.7. 3D Power efficiency of the ME gyrator connected to the PZT layer as a function of the shifted EMR frequency of the PZT layer with the increasing electric inductors.*

5.5.3. New structure ME gyrator.

For a traditional ME gyrator, the piezoelectric phase is basically a whole piece. When an external capacitor is added in order to tune EMR frequency, the result is a loss of power. Therefore, we designed an ME gyrator with new structures, as shown in Fig 5.8. The Metglas layers were bonded on the top and bottom of the piezoelectric phase using epoxy. The piezoelectric layer

consisted of three thin PZT layers, with the middle one connected to an external capacitor $C_o$ in order to change the total internal capacitance of the ME gyrator. The advantage of this new structure is that it serve to maintain the amplitude of the impedance despite any changes in EMR frequency; moreover, the power conversion can also be maintained with any changes in EMR frequency.

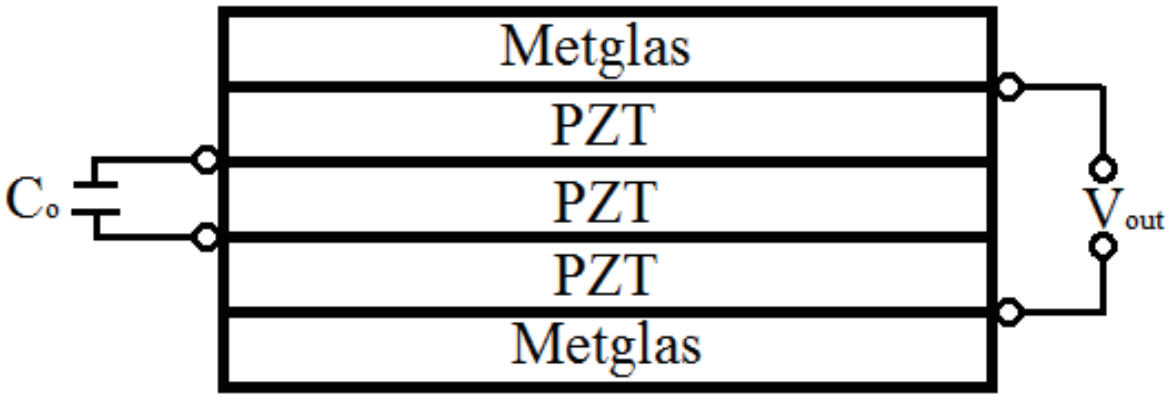


*Figure 5.8. Sketch of proposed new structure ME gyrator.*

Figure 5.9 illustrates the power efficiency of the new structure ME gyrator as a function of frequency with increasing electric capacitor. As the capacitor was increased from 0 pF to 135 pF, the efficiency was basically maintained at 64%. We attribute this outcome to the fact that the three PZT layers are separated by an epoxy layer. If the capacitance of the middle PZT layer is altered via an external capacitor, and this PZT layer is not connected to the electrical equipment, one can avoid any power loss in the circuit. Therefore, the EMR of the ME gyrator can be tuned while maintaining power efficiency.

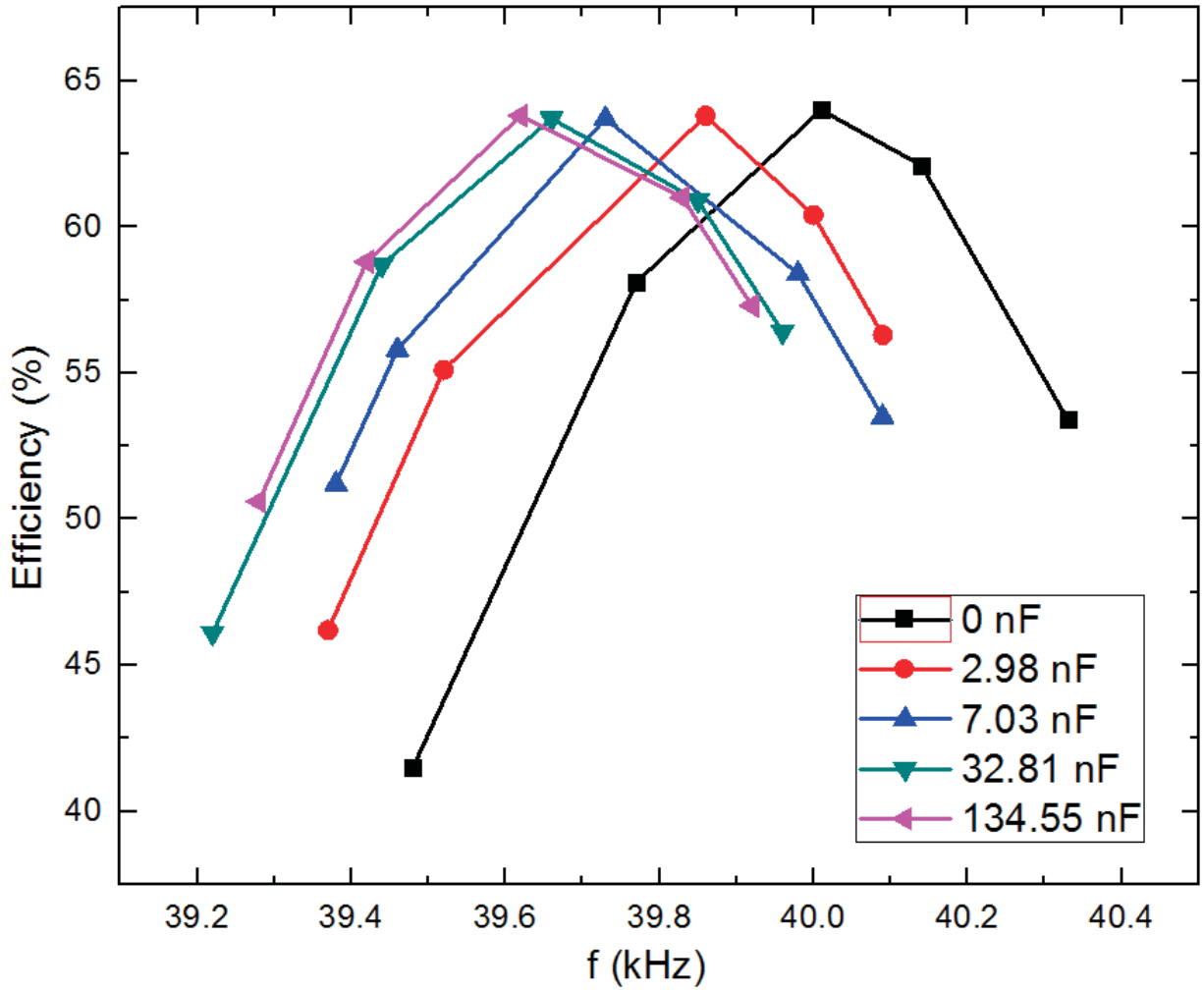


*Figure 5.9. Power efficiency of the new structure ME gyrator as a function of frequency with increasing electric capacitors.*

## 5.6. Summary of this section and future work.

As detailed in this section, an ME gyrator with magneto-piezoelectro-magneto structure was connected between a power amplifier and an acoustic transducer to significantly increase the power efficiency of the whole system. First, the circuit of the whole system was modified. Second, the impedance mismatch between the ME gyrator and the PZT transducer was solved with the optimized resistance load. Third, the EMR frequency tuning was realized using three methods: 1) size reduction, 2) capacitor and inductor tuning, and 3) new structure for ME gyrator.

# CHAPTER 6: CONCLUSION AND FUTURE WORK

## 6.1. Conclusion

As reported in this dissertation, I investigated how to enhance ME properties through an enhanced understanding of theoretical knowledge in terms of piezoelectric constant, piezomagnetic constant, elastic compliance, mechanical quality factor, and electromechanical coupling factor. Building on that knowledge, this dissertation also focus on how to use these theories in actual applications.

Previous research had shown that an ME sensor working in the active mode is less sensitive to mechanical stimuli compared with passive mode ME sensors. Therefore, ME sensors operating in H-field modulation were thoroughly investigated using Metglas/PMN-PT/Metglas features. Based on the expression of noise floor (1.20), this investigation was designed with the goal of increasing two parameters—namely the magnetomechanical coupling coefficient and mechanical capacitance—while at the same time decreasing mechanical resistance. The noise floor of the ME sensors working under H-field modulation was reduced to only 30 pT/√Hz, which is the lowest value currently known.

In order to enhance the vibration rejection of ME sensors working in an open environment, an active mode ME gradiometer consisting of one pair of ME sensors was developed. Under actual application conditions, the higher CMRR facilitates further distance detection. Therefore, an ME sensor with higher transfer function was needed, which was achieved by increasing both the magnetomechanical coupling factor and the eletromechanical coupling factor. The CMRR of the ME gradiometer working in H-field modulation was confirmed to be 74. The ME gradiometer response curve was firstly measured, which showed it was capable of detecting a magnetic source out to a distance normalized to the baseline of D/d = 13. Furthermore, the vibration rejection ratio

of this active ME gradiometer was also determined. Results showed that the VRR of an ME gradiometer working in the H-field modulation was 3 times higher than that of a passive mode ME gradiometer, and only 30% smaller than a fluxgate gradiometer. These findings clearly confirm the applications potential for an active mode ME gradiometer in actual operating conditions. Based on the features of a gradiometer, it not only can measure the distance between a magnetic source and the gradiometer, but also can determine the angle between a magnetic source and the gradiometer. Using two ME gradiometers consisting of three ME sensors, we were able to determine the unique pattern groups of the magnetic field distributions, which showed the location of an unknown magnetic source. Additionally, the magnetic gradient of the source was also detected using an active mode ME gradiometer. The eight measurement points were symmetrically located on the eight corners of a cubic with a dimension of 60 cm × 60 cm × 60 cm. The results clearly showed the change of the magnetic gradient of a source, which demonstrates its potential for localization of an unknown magnetic source in 3D space.

Due to the extremely high power conversion efficiency of an ME gyrator, we focused on how much energy could be transmitted using an ME laminate as a transmitter. In so doing we were able to study the optimization and efficiency of an ME laminate transmitter. Compared with the traditional radiation antenna for kHz, the proposed ME laminate transmitter used mechanical vibrations to excite induction transmission in the near field using ME laminates. Although the proposed ME laminate transmitter can only operate with localized security induction transmission, the size is much smaller than traditional antenna in the 30 kHz range. The results also revealed that its efficiency could be optimized by increasing the number of Metglas layers. It must be noted that although efficiency values were modest, they were nonetheless approximately three or four orders higher than that of a current-loop of the same size. In order to generate more power at the output

port during the inductive power transmission process, the transfer function of the ME laminate transmitter was increased. The underlying theory behind increasing the transfer function of the ME laminate transmitter is that it facilitates the induction transmission of more energy from the electric form to the magnetic form in the near field. While efficiency levels could be improved with even higher input power and a large number of ME laminate transmitter groups, there will be a trade-off between efficiency and size.

In order to address the limitation problem when a power amplifier needs to drive an acoustic transducer at high frequency, an ME gyrator can be set between the power amplifier and the transducer. However, the efficiency of the whole system will be extremely low due to the impedance mismatch and the EMR frequency mismatch between the ME gyrator and the transducer. Therefore, three essential steps were implemented to solve the two mismatch problems. First, the equivalent circuit of the whole system was modified, which clearly showed the internal electric capacitance of the system and the optimized resistance load. Secondly, the resistance load was optimized to increase the overall efficiency of the system. Thirdly, the EMR frequency tuning of the PZT transducer was achieved using size reduction, capacitor and inductor tuning, and developing a new structure ME gyrator.

## 6.2. Future work

As we discovered in developing this ME gyrator application, certain problems must be addressed in future investigations. The first issue pertains to the equivalent circuit modification. The circuit only describes conditions under EMR, which represents the ideal case as noted in Chapter 5. However, cases under non-resonance frequency must also be considered. Secondly, based on prior research in our lab, the power efficiency of an ME gyrator strongly depends on the

magneto-mechanical coupling factor and the mechanical quality factor. Therefore, new materials with optimized parameters for both factors need to be developed, which can then enhance power efficiency in order to reduce any power loss through the magnetomechanical and electromechanical power conversion process. Third, the power efficiency of our ME gyrator was maintained based on the new structure of piezoelectric phase using capacitor tuning. However, the power efficiency of the ME gyrator featuring this new structure was only ~60% , which is much lower than an ME gyrator based on the traditional configuration (over 90%). Therefore, next-generation ME gyrators based on this new structure with enhanced power efficiency need to be studied and characterized.

# REFERENCES


1 Fiebig, M. Revival of the magnetoelectric effect. *J Phys D Appl Phys* **38**, R123-R152, doi:10.1088/0022-3727/38/8/R01 (2005).

2 Eerenstein, W., Mathur, N. D. & Scott, J. F. Multiferroic and magnetoelectric materials. *Nature* **442**, 759-765, doi:10.1038/nature05023 (2006).

3 Nan, C.-W. New materials from non-intuitive composite effects. *Z Metallkd* **94**, 1148-1152 (2003).

4 Bichurin, M. I., Petrov, V. M. & Srinivasan, G. Theory of low-frequency magnetoelectric coupling in magnetostrictive-piezoelectric bilayers. *Physical Review B* **68**, 054402, doi:10.1103/PhysRevB.68.054402 (2003).

5 Astrov, D. N. The magnetoelectric effect in antiferromagnetics. *Sov. Phys. JETP* **11**, 708-709 (1960).

6 Astrov, D. N. Magnetoelectric effect in chromium oxide. *Sov. Phys. JETP* **13**, 729-733 (1961).

7 Gehring, G. A. On the microscopic theory of the magnetoelectric effect. *Ferroelectrics* **161**, 275-285 (1994).

8 Van Suchtelen, J. Product properties: a new application of composite materials. *Philips Res. Rep* **27**, 28-37 (1972).

9 Curie, P. Sur la symétrie dans les phénomènes physiques, symétrie d'un champ électrique et d'un champ magnétique. *Journal de physique théorique et appliquée* **3**, 393-415 (1894).

10 Das, J., Gao, J., Xing, Z., Li, J. F. & Viehland, D. Enhancement in the field sensitivity of magnetoelectric laminate heterostructures. *Applied Physics Letters* **95**, 092501 (2009).

11 Nan, C.-W., Bichurin, M. I., Dong, S., Viehland, D. & Srinivasan, G. Multiferroic magnetoelectric composites: Historical perspective, status, and future directions. *Journal of applied physics* **103**, 1 (2008).

12 Van den Boomgaard, J., Terrell, D. R., Born, R. A. J. & Giller, H. An in situ grown eutectic magnetoelectric composite material. *Journal of Materials Science* **9**, 1705-1709 (1974).

13 Nan, C. W., Li, M. & Huang, J. H. Calculations of giant magnetoelectric effects in ferroic composites of rare-earth–iron alloys and ferroelectric polymers. *Physical Review B* **63**, 144415 (2001).

14 Ryu, J., Priya, S., Carazo, A. V., Uchino, K. & Kim, H. E. Effect of the Magnetostrictive Layer on Magnetoelectric Properties in Lead Zirconate Titanate/Terfenol-D Laminate Composites. *Journal of the American Ceramic Society* **84**, 2905-2908 (2001).

15 Dong, S., Cheng, J., Li, J. F. & Viehland, D. Enhanced magnetoelectric effects in laminate composites of Terfenol-D/Pb (Zr, Ti) O 3 under resonant drive. *Applied Physics Letters* **83**, 4812-4814 (2003).

16 Dong, S., Li, J.-F. & Viehland, D. Longitudinal and transverse magnetoelectric voltage coefficients of magnetostrictive/piezoelectric laminate composite: Experiments. *IEEE transactions on ultrasonics, ferroelectrics, and frequency control* **51**, 794-799 (2004).

17 Zhai, J., Dong, S., Xing, Z., Li, J. & Viehland, D. Giant magnetoelectric effect in Metglas/polyvinylidene-fluoride laminates. *Applied Physics Letters* **89**, 083507 (2006).

18 Wang, Y. *et al.* An extremely low equivalent magnetic noise magnetoelectric sensor. *Advanced Materials* **23**, 4111-4114 (2011).

19 Sandlund, L. *et al.* Magnetostriction, elastic moduli, and coupling factors of composite Terfenol-D. *Journal of Applied Physics* **75**, 5656-5658 (1994).
20 Guruswamy, S., Srisukhumbowornchai, N., Clark, A. E., Restorff, J. B. & Wun-Fogle, M. Strong, ductile, and low-field-magnetostrictive alloys based on Fe-Ga. *Scripta Materialia* **3**, 239-244 (2000).
21 Malmhäll, R. *et al.* Metglas 2826B—Transport, magnetic and thermal properties. *Journal of Applied Physics* **49**, 1727-1729 (1978).
22 Yang, J. *An introduction to the theory of piezoelectricity*. Vol. 9 (Springer, 2005).
23 Srinivas, K., Prasad, G., Bhimasankaram, T. & Suryanarayana, S. V. Electromechanical coefficients of magnetoelectric PZT–CoFe2O4 composite. *Modern Physics Letters B* **14**, 663-674 (2000).
24 Fu, H. & Cohen, R. E. Polarization rotation mechanism for ultrahigh electromechanical response in single-crystal piezoelectrics. *Nature* **403**, 281 (2000).
25 Shirane, G. & Suzuki, K. Crystal structure of Pb (Zr-Ti) O3. *Journal of the Physical Society of Japan* **7**, 333-333 (1952).
26 Leontsev, S. O. & Eitel, R. E. Progress in engineering high strain lead-free piezoelectric ceramics. *Science and Technology of Advanced Materials* **11**, 044302 (2010).
27 Dong, S., Li, J.-F. & Viehland, D. Ultrahigh magnetic field sensitivity in laminates of TERFENOL-D and Pb (Mg 1/3 Nb 2/3) O 3–PbTiO 3 crystals. *Applied Physics Letters* **83**, 2265-2267 (2003).
28 Laletsin, U., Padubnaya, N., Srinivasan, G. & Devreugd, C. P. Frequency dependence of magnetoelectric interactions in layered structures of ferromagnetic alloys and piezoelectric oxides. *Applied Physics A* **78**, 33-36 (2004).
29 Harshe, G., Dougherty, J. P. & Newnham, R. E. 224-235 (International Society for Optics and Photonics).
30 Srinivasan, G. *et al.* Erratum: Magnetoelectric bilayer and multilayer structures of magnetostrictive and piezoelectric oxides [Phys. Rev. B 64, 214408 (2001)]. *Physical Review B* **66**, 029902 (2002).
31 Dong, S. *et al.* Fe–Ga⁄Pb (Mg 1⁄3 Nb 2⁄3) O 3–Pb Ti O 3 magnetoelectric laminate composites. *Applied Physics Letters* **87**, 222504 (2005).
32 Dong, S. *et al.* Magnetostrictive and magnetoelectric behavior of Fe–20 at.% Ga⁄Pb (Zr, Ti) O 3 laminates. *Journal of applied physics* **97**, 103902 (2005).
33 Zhai, J., Xing, Z., Dong, S., Li, J. & Viehland, D. Magnetoelectric laminate composites: an overview. *Journal of the American Ceramic Society* **91**, 351-358 (2008).
34 Dong, S., Li, J.-F. & Viehland, D. Longitudinal and transverse magnetoelectric voltage coefficients of magnetostrictive/piezoelectric laminate composite: theory. *IEEE Transactions on Ultrasonics, Ferroelectrics, and frequency control* **50**, 1253-1261 (2003).
35 Dong, S., Zhai, J., Li, J. & Viehland, D. Near-ideal magnetoelectricity in high-permeability magnetostrictive/piezofiber laminates with a (2-1) connectivity. *Applied Physics Letters* **89**, 252904 (2006).
36 Srinivasan, G., Rasmussen, E. T., Levin, B. J. & Hayes, R. Magnetoelectric effects in bilayers and multilayers of magnetostrictive and piezoelectric perovskite oxides. *Physical Review B* **65**, 134402 (2002).
37 Dong, S. & Zhai, J. Equivalent circuit method for static and dynamic analysis of magnetoelectric laminated composites. *Chinese Science Bulletin* **53**, 2113-2123 (2008).

38 Lin, Y., Cai, N., Zhai, J., Liu, G. & Nan, C.-W. Giant magnetoelectric effect in multiferroic laminated composites. *Physical Review B* **72**, 012405 (2005).
39 Sim, C. H., Pan, A. Z. Z. & Wang, J. Thickness and coupling effects in bilayered multiferroic CoFe 2 O 4/Pb (Zr 0.52 Ti 0.48) O 3 thin films. *Journal of Applied Physics* **103**, 124109 (2008).
40 Fang, F., Zhao, C. & Yang, W. Thickness effects on magnetoelectric coupling for Metglas/PZT/Metglas laminates. *Science China Physics, Mechanics and Astronomy* **54**, 581-585 (2011).
41 Srinivasan, G. *et al.* Resonant magnetoelectric coupling in trilayers of ferromagnetic alloys and piezoelectric lead zirconate titanate: The influence of bias magnetic field. *Physical Review B* **71**, 184423 (2005).
42 Zhuang, X. *et al.* Theoretical intrinsic equivalent magnetic noise evaluation for magneto (elasto) electric sensors using modulation techniques. *IEEE Sensors Journal* **14**, 150-158 (2013).
43 Ma, J., Hu, J., Li, Z. & Nan, C. W. Recent progress in multiferroic magnetoelectric composites: from bulk to thin films. *Advanced Materials* **23**, 1062-1087 (2011).
44 Jia, Y., Luo, H., Zhao, X. & Wang, F. Giant magnetoelectric response from a piezoelectric/magnetostrictive laminated composite combined with a piezoelectric transformer. *Advanced materials* **20**, 4776-4779 (2008).
45 Gao, J., Das, J., Xing, Z., Li, J. & Viehland, D. Comparison of noise floor and sensitivity for different magnetoelectric laminates. *Journal of Applied Physics* **108**, 084509 (2010).
46 Dong, S., Zhai, J., Bai, F., Li, J.-F. & Viehland, D. Push-pull mode magnetostrictive/piezoelectric laminate composite with an enhanced magnetoelectric voltage coefficient. *Applied Physics Letters* **87**, 062502 (2005).
47 Zhuang, X. *et al.* Theoretical analysis of the intrinsic magnetic noise spectral density of magnetostrictive-piezoelectric laminated composites. *Journal of Applied physics* **109**, 124512 (2011).
48 Xing, Z., Li, J. & Viehland, D. Modeling and the signal-to-noise ratio research of magnetoelectric sensors at low frequency. *Applied Physics Letters* **91**, 142905 (2007).
49 Wang, Z., Zhang, R., Sun, E. & Cao, W. Contributions of domain wall motion to complex electromechanical coefficients of 0.62 Pb (Mg 1/3 Nb 2/3) O 3–0.38 PbTiO 3 crystals. *Journal of applied physics* **107**, 014110 (2010).
50 Chen, L., Xiong, X. M., Meng, H., Lv, P. & Zhang, J. X. Migration and redistribution of oxygen vacancy in barium titanate ceramics. *Applied physics letters* **89**, 071916 (2006).
51 Petrie, J. *et al.* Enhancing the sensitivity of magnetoelectric sensors by increasing the operating frequency. *Journal of Applied Physics* **110**, 124506 (2011).
52 Zhuang, X. *et al.* Evaluation of applied axial field modulation technique on ME sensor input equivalent magnetic noise rejection. *IEEE Sensors Journal* **11**, 2266-2272 (2011).
53 Gillette, S. M. *et al.* Improved sensitivity and noise in magneto-electric magnetic field sensors by use of modulated AC magnetostriction. *IEEE Magnetics Letters* **2**, 2500104-2500104 (2011).
54 Petrie, J. R. *et al.* Enhanced sensitivity of magnetoelectric sensors by tuning the resonant frequency. *Applied Physics Letters* **99**, 043504 (2011).
55 Jahns, R., Greve, H., Woltermann, E., Quandt, E. & Knöchel, R. Sensitivity enhancement of magnetoelectric sensors through frequency-conversion. *Sensors and Actuators A: Physical* **183**, 16-21 (2012).

56 Shen, L. *et al.* Magnetoelectric nonlinearity in magnetoelectric laminate sensors. *Journal of Applied Physics* **110**, 114510 (2011).
57 Malatek, M., Dufay, B., Saez, S. & Dolabdjian, C. Improvement of the off-diagonal magnetoimpedance sensor white noise. *Sensors and Actuators A: Physical* **204**, 20-24 (2013).
58 Salem, A., Hamada, T., Asahina, J. K. & Ushijima, K. Detection of unexploded ordnance (UXO) using marine magnetic gradiometer data. *Exploration Geophysics* **36**, 97-103 (2005).
59 Shen, Y. *et al.* Metglas/Pb (Mg 1/3 Nb 2/3) O 3-PbTiO 3 magnetoelectric gradiometric sensor with high detection sensitivity. *IEEE transactions on ultrasonics, ferroelectrics, and frequency control* **59**, 2111-2115 (2012).
60 Xi, H. *et al.* A room temperature ultrasensitive magnetoelectric susceptometer for quantitative tissue iron detection. *Scientific reports* **6**, 29740 (2016).
61 Xi, H. *et al.* 1-3 (IEEE).
62 Xing, Z., Zhai, J., Li, J. & Viehland, D. Investigation of external noise and its rejection in magnetoelectric sensor design. *Journal of Applied Physics* **106**, 024512 (2009).
63 Ripka, P. Review of fluxgate sensors. *Sensors and Actuators A: Physical* **33**, 129-141 (1992).
64 Dong, S., Li, J.-F. & Viehland, D. in *Frontiers of Ferroelectricity* 97-106 (Springer, 2006).
65 Callen, H. B. & Welton, T. A. Irreversibility and generalized noise. *Physical Review* **83**, 34 (1951).
66 Zhuang, X. *et al.* Mechanical noise limit of a strain-coupled magneto (elasto) electric sensor operating under a magnetic or an electric field modulation. *IEEE Sensors Journal* **15**, 1575-1587 (2014).
67 Mei, L., Rupprecht, S., Yang, Q. & Zhang, Q. M. 85-86 (IEEE).
68 *Billingsley Aerospace & Defense*, <https://magnetometer.com/> (2014).
69 Xu, J. *et al.* Magnetoelectric gradiometer with enhanced vibration rejection efficiency under H-field modulation. *Journal of Applied Physics* **123**, 104501 (2018).
70 Newman, E. M. *THE BIGGEST LITTLE ANTENNA IN THE WORLD*, <http://arlassociates.net/Newman%20AP%20Presentation.pdf> (2012).
71 Li, M. *et al.* Ultra-sensitive NEMS magnetoelectric sensor for picotesla DC magnetic field detection. *Applied Physics Letters* **110**, 143510 (2017).
72 Wang, Y. J. *et al.* A review on equivalent magnetic noise of magnetoelectric laminate sensors. *Philosophical Transactions of the Royal Society A: Mathematical, Physical and Engineering Sciences* **372**, 20120455 (2014).
73 Xing, Z. P. *et al.* Modeling and detection of quasi-static nanotesla magnetic field variations using magnetoelectric laminate sensors. *Measurement Science and Technology* **19**, 015206 (2007).
74 Gao, J. *et al.* Enhanced sensitivity to direct current magnetic field changes in Metglas/Pb (Mg1/3Nb2/3) O3–PbTiO3 laminates. *Journal of Applied Physics* **109**, 074507 (2011).
75 Wang, Y. *et al.* Influence of interfacial bonding condition on magnetoelectric properties in piezofiber/Metglas heterostructures. *Journal of Alloys and Compounds* **513**, 242-244 (2012).

76 Li, M. *et al.* Enhanced sensitivity and reduced noise floor in magnetoelectric laminate sensors by an improved lamination process. *Journal of the American Ceramic Society* **94**, 3738-3741 (2011).
77 Chu, Z. *et al.* Enhanced resonance magnetoelectric coupling in (1-1) connectivity composites. *Advanced Materials* **29**, 1606022 (2017).
78 Leung, C. M. *et al.* Importance of composite parameters in enhanced power conversion efficiency of Terfenol-D/PZT magnetoelectric gyrators. *Applied Physics Letters* **110**, 112904 (2017).
79 Leung, C. M. *et al.* Power conversion efficiency and resistance tunability in coil-magnetoelectric gyrators. *Applied Physics Letters* **109**, 202907 (2016).
80 Leung, C. M. *et al.* Highly efficient solid state magnetoelectric gyrators. *Applied Physics Letters* **111**, 122904 (2017).
81 Leung, C. M. *et al.* Enhanced stability of magnetoelectric gyrators under high power conditions. *Applied Physics Letters* **111**, 182901 (2017).
82 Yao, Z., Wang, Y. E., Keller, S. & Carman, G. P. Bulk acoustic wave-mediated multiferroic antennas: Architecture and performance bound. *IEEE Transactions on Antennas and Propagation* **63**, 3335-3344 (2015).
83 Chu, L. J. Physical limitations of omni-directional antennas. *Journal of applied physics* **19**, 1163-1175 (1948).
84 Stutzman, W. L. & Thiele, G. A. *Antenna theory and design*. (John Wiley & Sons, 2012).
85 Balanis, C. A. *Antenna theory: analysis and design*. (John wiley & sons, 2016).
86 Zhuang, X., Leung, C. M., Li, J., Srinivasan, G. & Viehland, D. Power conversion efficiency and equivalent input loss factor in magnetoelectric gyrators. *IEEE Transactions on Industrial Electronics* **66**, 2499-2505 (2018).